JETP Letters, Vol. 74, No. 2, 2001, pp. 100–102. Translated from Pis'ma v Zhurnal Éksperimental'noĭ i Teoreticheskoĭ Fiziki, Vol. 74, No. 2, 2001, pp. 105–107.

Terahertz Injection Electroluminescence in Multiperiod Quantum-Cascade AlGaAs/GaAs Structures

N. N. Zinov'ev[1, 3], A. V. Andrianov[1]*, V. Yu. Nekrasov[1], V. A. Petrovskiĭ[1], L. V. Belyakov[1], O. M. Sreseli[1], G. Hill[2], and J. M. Chamberlain[3]

[1] *Ioffe Physicotechnical Institute, Russian Academy of Sciences, Politekhnicheskaya ul. 26, St. Petersburg, 194021 Russia*
** e-mail: Alex.Andrianov@pop.ioffe.tssi.ru*

[2] *Department of Electronic and Electrical Engineering, University of Sheffield, Sheffield, S10 2TN, United Kingdom*

[3] *IMP, School of Electronic and Electrical Engineering, University of Leeds, Leeds LS2 9JT, United Kingdom*

Received June 14, 2001

Terahertz electroluminescence in the range ≈1.5 THz was observed in a quantum-cascade GaAs/AlGaAs structure containing 40 periods of tunnel-coupled wells. The luminescence is caused by the spatially indirect optical electron transitions between the ground states of neighboring quantum wells. © *2001 MAIK "Nauka/Interperiodica".*

PACS numbers: 78.67.De; 78.60.Fi; 07.57.Hm

The terahertz (or far-IR) band is among the most difficult to access and, as a result, is the least studied frequency range of the electromagnetic spectrum. In recent years, progress in band-gap engineering has provided techniques for designing terahertz sources based on semiconducting multiperiod size-quantized systems with carrier injection and intersubband radiative transitions [1]. The ideas pioneered in [1] were implemented in practice in the mid-IR range [2, 3]. It is expected that the approach developed in designing mid-IR quantum-cascade lasers and quantum-cascade structures (QCSs) will be helpful in the development of devices for the far-IR range, where compact light sources are presently lacking. The generation of far-IR emission through the radiative relaxation of size-quantized electrons in quantum wells (QWs) is hampered by the competing phonon emission and electron–electron scattering processes [4]. Far-IR electroluminescence was recently observed in parabolic QWs [5] and in QCSs [6, 7]. Nevertheless, the achieved radiative recombination efficiency reported to date is still low. Further use of band engineering techniques such as the design of QCSs with optimal tunneling conditions, as well as the use of asymmetric QWs [8, 9] and QCSs constructed on the basis of type II heterostructures, will permit the enhancement of the efficiency of far-IR electroluminescence and, ultimately, produce stimulated radiation.

The structures studied in this work were grown by molecular beam epitaxy at the MBE EPSRC centre, University of Sheffield (Great Britain). The structure was grown on a semi-isolating (100) GaAs substrate and contained 40 periods, each composed of four GaAs QWs separated by tunneling $Al_{0.15}Ga_{0.85}As$ barriers. The widths of wells and barriers, and their sequence, were as follows: 280-Å QW, 25-Å barrier, 180-Å QW, 40-Å barrier, 160-Å QW, 25-Å barrier, 150-Å QW, and 40-Å barrier. Then, the periods were repeated. The quantum-cascade structure was constructed so as to produce, as in [6], terahertz radiation as a result of the intraband optical electron transitions between the lowest dimensionally quantized subbands. The 280-Å and 180-Å quantum wells separated by a 25-Å-thick tunneling barrier formed the active region of the structure. The next two 160-Å and 150-Å wells separated by the same barrier served as an injector delivering electrons to the QW in the next period. Unlike the QCSs studied in [6], where the tunneling barriers between the neighboring periods of the structure were 60 Å wide, the width of tunneling barriers between the periods of our structures was brought down to 40 Å with the aim of enhancing the efficiency of injection and the depletion of the ground state. A decrease in the width of the injection barrier also allowed the observation of the indirect optical transitions between the lower states in the active region. To depress the influence of an injection-induced volume charge, the 160-Å and 150-Å QWs were doped with silicon to a level of $\approx 10^{16}$ cm^{-3}. A 2-μm n^+-GaAs layer ($n \approx 2 \times 10^{18}$ cm^{-3}) with a 100-nm GaAs (undoped) spacer on the substrate side formed a two-dimensional 2D injecting junction. Similar layers of n^+GaAs and undoped GaAs functioned as the upper 2D contact.

For measurements, mesa structures ≈400 μm in diameter were formed on the samples. To extract radiation along the normal to the structure surface (perpendicular to the QW plane), a metallic (Cr/Au) grating with a period of 20 μm was put on the upper contact layer to convert the QCS radiation mode into a mode

with the wave vector normal to the structure plane. The samples were mounted on the copper cold finger of a helium optical cryostat, using a "warm" window made from polyethylene. A bias in the form of rectangular pulses with a frequency of 500 kHz (period-to-pulse duration ratio 2) modulated by low-frequency rectangular pulses (80 Hz; period-to-pulse duration ratio 2; modulation factor 1) was applied to the samples. This bias was used to minimize sample heating during the course of measurements.

Electroluminescence (EL) was recorded with the use of a Fourier transform spectrometer constructed on the basis of a Grubbs–Parsons instrument. The inner volume of the spectrometer was evacuated to avoid the influence of water vapor absorption. A liquid-helium-cooled silicon bolometer (QMW Instruments) with a bandpass optical filter placed at its input to provide operation in the spectral range 2–400 cm^{-1} served as a detector of far-IR radiation. The detector signal was measured at the current modulation frequency (80 Hz) using an SR-530 lock-in amplifier. The moving mirror of the FT spectrometer was translated by a high-precision reciprocating feedback Newport system that provided positioning accuracy no worse than 0.25 μm. The mirror translation control, the measurement of the amplifier output, the bias pulse amplitude control, and the fast Fourier transform of the interferograms were performed using a computer.

After application of bias to the structure, a terahertz radiation was detected. The signal increased with increasing bias on the structure (Fig. 1). At small voltages, the signal was lost in noise. As the voltage increased to 4–9 V, the signal-to-noise ratio increased appreciably and reached a value of ten or more (Fig. 1). A typical signal interferogram is shown in the inset in Fig. 1. A pronounced maximum is clearly seen in the interferogram when the moving mirror passes through the position corresponding to zero path difference between the interferometer arms.

The spectrum of terahertz radiation at a voltage of 5.5 V on the quantum-cascade structure is shown in Fig. 2. The spectra were measured with a resolution of ≈10 cm^{-1}. This resolution was chosen to minimize the spectrum recording time. It is seen that the band with a maximum at 48.8 cm^{-1} (605 meV or 1.46 THz) and a halfwidth of about 30 cm^{-1} makes the main contribution to the EL spectrum. This spectrum differs noticably from the data obtained in [6], where a narrow emission line with a maximum at 113.6 cm^{-1} due to the transitions between the second and first size-quantization subbands in a quantum well of thickness 280 Å (QCS active region) was observed.

The frequency corresponding to the emission maximum in our spectrum increases with increasing bias voltage. This dependence can be approximated by a linear function (Fig. 3) with a slope of approximately 8.9 cm^{-1}/V. The fact that the maximum position depends linearly on the applied bias suggests that the

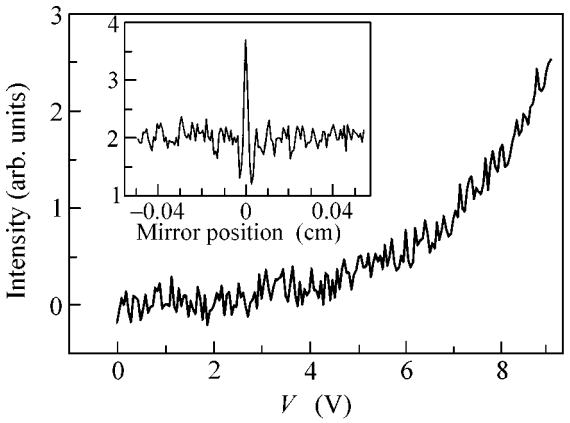

Fig. 1. Terahertz radiation intensity as a function of bias V on the structure. Inset: signal intensity vs. the position of interferometer mirror. The pass band of the input filter is 2–400 cm^{-1} and T = 7–13 K.

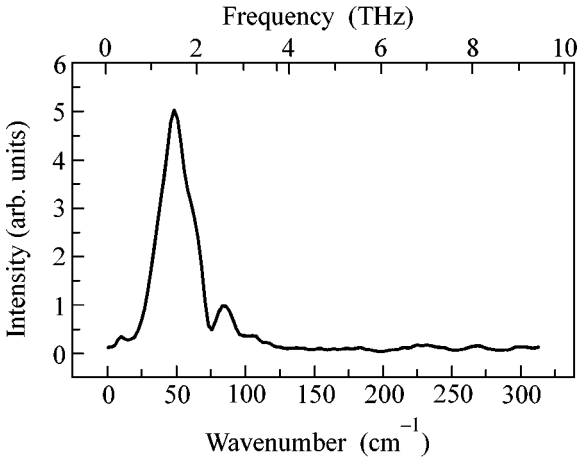

Fig. 2. Terahertz emission spectrum; T = 7 K and V = 5.5 V.

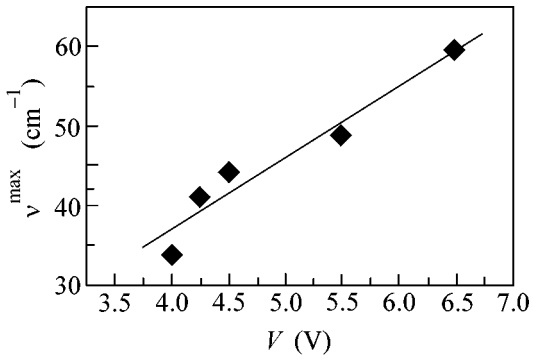

Fig. 3. Position of terahertz emission maximum ν^{max} vs. applied bias V.

observed band is caused by the emission accompanying the indirect (in real space) electron transitions in the QCS. Electron transitions between the ground state of the 280-Å well and the ground state of the neighboring well could be responsible. Our estimates showed that, considering the voltage drop on the contacts, a bias of approximately 1.5–2 V should be applied to the structure to equalize the lowest levels in the neighboring QWs of the active region of QCS. Note that the EL is excited starting at biases close to this value (Fig. 1).

The estimates of the integrated intensity of terahertz radiation with correction for the efficiency of radiation collection provide a value of about 2 nW at a bias of 5.5 V and an input electric power of 700 mW for the structures prepared and studied in this work. This gives a value on the order of 3×10^{-9} for the emitter quantum efficiency.

In summary, a new terahertz electroluminescence band has been observed in this work. For the quantum-cascade structures containing tunnel-coupled GaAs/AlGaAs quantum wells, the emission maximum in the EL spectrum occurs near 48.8 cm^{-1} (1.46 THz) with a bias of 5.5 V and shifts linearly to higher frequencies with increasing bias. The observed behavior of the terahertz electroluminescence suggests that it is caused by the spatially indirect electron transitions between the ground state of the wide well and the ground state of the neighboring "ejecting" well.

This work was supported in part by the INTAS (grant no. 97-0856), the Russian Foundation for Basic Research "Scientific School" (project no. 00-15-96750), and the program "Size-Quantized Nanostructures." N.N.Z. is grateful to the EPSRC for the support of his visit to the UK.

REFERENCES

1. R. F. Kazarinov and R. A. Suris, Fiz. Tekh. Poluprovodn. (Leningrad) **5**, 797 (1971) [Sov. Phys. Semicond. **5**, 707 (1971)]; Fiz. Tekh. Poluprovodn. (Leningrad) **6**, 148 (1972) [Sov. Phys. Semicond. **6**, 120 (1972)].
2. J. Faist, F. Capasso, D. L. Sivco, *et al.*, **264**, 553 (1994).
3. F. Capasso, J. Faist, S. Sitori, and A. Y. Cho, Solid State Commun. **102**, 231 (1997).
4. P. Hyldgaard and J. W. Wilkins, Phys. Rev. B **53**, 6889 (1996).
5. K. D. Maranovski, A. C. Cossard, K. Unterrainer, and E. Gornik, Appl. Phys. Lett. **69**, 3522 (1996).
6. M. Rochat, J. Faist, M. Beck, *et al.*, Appl. Phys. Lett. **73**, 3724 (1998).
7. J. Ulrich, R. Zobl, V. Schrenk, *et al.*, Appl. Phys. Lett. **77**, 1928 (2000).
8. P. Harrison, R. W. Kelsall, K. Donovan, and P. Kinsler, IEEE Trans. Microwave Theory Technol. **48**, 645 (2000).
9. P. Kinsler, P. Harrison, and R. W. Kelsall, Phys. Rev. B **58**, 4771 (1998).

Translated by V. Sakun

JETP Letters, Vol. 74, No. 2, 2001, pp. 103–106. Translated from Pis'ma v Zhurnal Éksperimental'noĭ i Teoreticheskoĭ Fiziki, Vol. 74, No. 2, 2001, pp. 108–111.

Temperature Dependence of the Cu(2) NQR Line Width in $YBa_2Cu_3O_{7-y}$

A. V. Dooglav, M. V. Eremin, Yu. A. Sakhratov, and A. V. Savinkov

Kazan State University, ul. Kremlevskaya 18, Kazan, 420008 Russia

Received June 19, 2001

Systematic measurements of the ^{63}Cu(2) NQR line width were performed in underdoped $YBa_2Cu_3O_{7-y}$ samples over the temperature range 4.2 K < T < 300 K. It was shown that the copper NQR line width monotonically increases with decreasing temperature in the below-critical region, resembling temperature behavior of the superconducting gap. The observed dependence is explained by the fact that the energy of a condensate of sliding charge–current states of the charge-density-wave type depends on the phase of order parameter. Calculations show that this dependence appears only at $T < T_c$. Quantitative estimates of the line broadening at $T < T_c$ agree with the measurement results. © *2001 MAIK "Nauka/Interperiodica".*

PACS numbers: 74.25.Nf; 76.60.Gv; 74.72.Bk; 71.45.Lr

It is generally believed that the Cu(2) NQR lines in high-T_c superconductors of the 123 type with oxygen index close to 7 are strongly broadened due to crystal defects (oxygen vacancies and interstitials, twinning, impurity phases, lattice imperfections, etc.). This is confirmed by the fact that the copper NQR line width in the 1248 compound with stoichiometric composition is appreciably smaller than in the 1237 compound [1]. The NQR line widths in $YBa_2Cu_3O_{7-y}$ (Y1237) samples were studied by different scientific groups and found to vary over a rather wide range: 200–350 kHz at room temperature. The width hardly changes upon changing the temperature from room to critical (T_c). However, starting at T_c (or below T_c at weak doping [2]), the line width starts to increase rapidly. Although the reasons for this broadening are as yet unclear, its quadrupolar origin is evident from the comparison of the line widths of the ^{63}Cu and ^{65}Cu isotopes. As a rule, the larger the NQR line width at $T > T_c$, the larger the broadening. If one assumes that the line width at $T > T_c$, is due to lattice defects, then one should accept that these defects influence, at least in part, the broadening of the NQR lines below T_c. There are grounds to believe that the broadening at $T < T_c$ depends on the doping level of the sample. For instance, the Cu(2) NQR line width measured in [3] for an overdoped Y1237 sample hardly changed in the temperature range 300–10 K, although the line width (about 290 kHz) was not too small; i.e., the sample studied in that work was not defectless.

Therefore, the temperature behavior of the NQR line width of the in-plane copper in a 123-type superconductor is nontrivial and calls for a better understanding. In this work, we report the results of a detailed linewidth study for two Y1237 samples and analyze the possible reasons of broadening. To interpret the additional quadrupole broadening below T_c, we suggest taking into account the retarded motion of charge–current waves and substantiating this by the mean-field calculations.

We carried out experiments using the same two paraffin-packed Y1237 powder samples with crystallite sizes ~30 μm, as in [4]. The critical temperatures (onset of transition) were 91.6 K (sample 1) and 91.2 K (sample 2). The copper NQR spectra were measured on a broadband coherent pulsed NQR/NMR spectrometer over the temperature range 300–4.2 K. Examples of the Cu(2) NQR spectra recorded at temperatures 300 and 4.2 K are given in Fig. 1. In both samples, the ^{63}Cu(2) NQR line shape is well fitted to the Lorentzian curve with temperature-dependent FWHH (Fig. 2). One can see that in both samples the line width varies weakly with temperature from room temperature to ~120 K. The line begins to broaden below 120 K and broadens sharply below T_c. Because of a large error in measuring the line width in sample 1, one cannot judge confidently any details of its behavior below T_c. The line width in sample 2 has a clear maximum at T = 47 K and a minimum at 35 K. These features are due to the spin–spin relaxation processes, which were discussed in [4].

Before analyzing the NQR line broadening near T_c, we adduce several arguments in favor of the assumption that this effect is intrinsic in nature, i.e., that it is inherent in the compound as such and is not associated with the surface effect of crystallites. It is well known that the penetration depth of an rf magnetic field exciting a nuclear spin system decreases upon transition into the superconducting state, as a result of which the NMR/NQR signal intensity also decreases, because the nuclei in the crystallite bulk drop out of the observation. Therefore, the relative contribution to the NMR/NQR signal from the nuclei located in the surface layers of

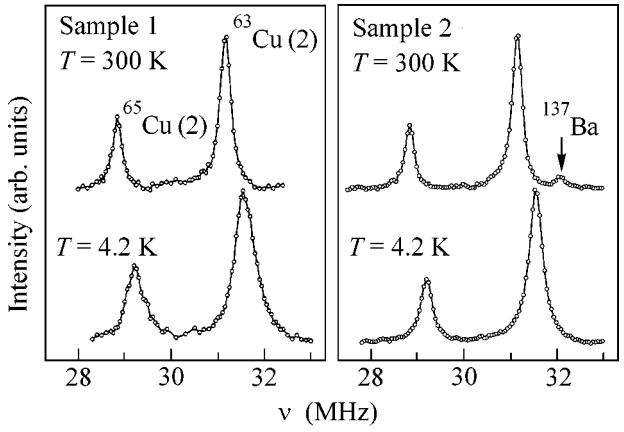

Fig. 1. ^{63,65}Cu(2) NQR spectra of $YBa_2Cu_3O_{7-y}$ at 300 and 4.2 K.

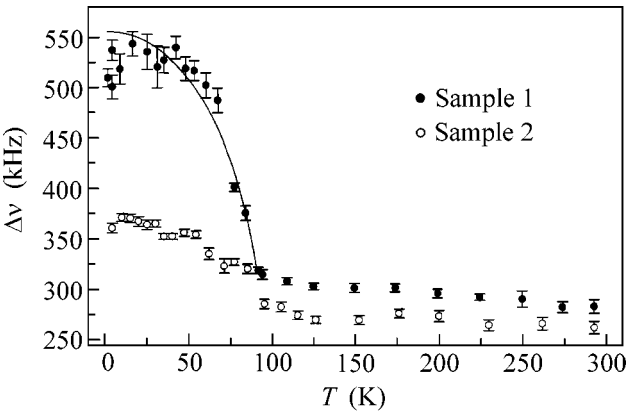

Fig. 2. Temperature dependence of the ^{63}Cu(2) NQR line width in $YBa_2Cu_3O_{7-y}$. The solid line is the result of calculation (see text) with the following parameters: T_c = 91 K, T^* = 120 K, $\Delta(T = 0\ \text{K})$ = 25 meV, $D(T = 0\ \text{K})$ = 30 meV, and $S(T)/D(T)$ = 0.08.

crystallites increases below T_c. Since the crystal lattice is distorted in the surface layers, the NQR line of the nuclei from this layer is ordinarily broader than the bulk line. The thickness of a distorted surface layer is governed by the crystal properties and is about 0.2 μm at worst (crystals mechanically dry-ground in a mortar and having no cleavage planes [5]). Our calculations have shown that, even if the surface NQR line is broader than the bulk line by a factor of 10, then, for the crystallites 30 μm in size and a 2.5-fold decrease in signal intensity below T_c (as is the case in our experiments), a faintly visible influence of the surface on the NQR line broadening occurs for a surface layer one micrometer thick. Since the relative line broadening in our experiments is equal to several tens of percent, we assume that the surface effect on the Cu(2) NQR line width can be ignored.

We believe that the above-mentioned features of the temperature behavior of line width shed new light on the coexistence regime of the pseudogap and superconducting phases in cuprates. Indeed, the energy of a quasiparticle in a superconductor in the presence of a homogeneous spatial modulation with wave vector $\mathbf{Q} = (\pi, \pi)$ is given by the expression

$$
\begin{aligned}
E^2_{1\mathbf{k},2\mathbf{k}} &= \frac{1}{2}(\epsilon^2_{\mathbf{k}} + \epsilon^2_{\mathbf{k}+\mathbf{Q}}) + |G_{\mathbf{k}}|^2 \\
&+ \frac{1}{2}(|\Delta_{\mathbf{k}}|^2 + |\Delta_{\mathbf{k}+\mathbf{Q}}|^2) + |U_{\mathbf{k}}|^2 \\
&\pm \Big\{ \frac{1}{4}[\epsilon^2_{\mathbf{k}} - \epsilon^2_{\mathbf{k}+\mathbf{Q}} + |\Delta_{\mathbf{k}}|^2 - |\Delta_{\mathbf{k}+\mathbf{Q}}|^2]^2 \\
&+ |G_{\mathbf{k}}|^2[(\epsilon_{\mathbf{k}} + \epsilon_{\mathbf{k}+\mathbf{Q}})^2 + |\Delta_{\mathbf{k}}|^2 + |\Delta_{\mathbf{k}+\mathbf{Q}}|^2] \\
&- \Delta^*_{\mathbf{k}}\Delta_{\mathbf{k}+\mathbf{Q}}G^2_{\mathbf{k}} - \Delta_{\mathbf{k}}\Delta^*_{\mathbf{k}+\mathbf{Q}}(G^*_{\mathbf{k}})^2 \\
&+ |U_{\mathbf{k}}|^2[(\epsilon_{\mathbf{k}} - \epsilon_{\mathbf{k}+\mathbf{Q}})^2 + |\Delta_{\mathbf{k}}|^2 + |\Delta_{\mathbf{k}+\mathbf{Q}}|^2] \\
&+ \Delta_{\mathbf{k}}\Delta_{\mathbf{k}+\mathbf{Q}}(U^*_{\mathbf{k}})^2 + \Delta^*_{\mathbf{k}}\Delta^*_{\mathbf{k}+\mathbf{Q}}U^2_{\mathbf{k}} \\
&+ 2\epsilon_{\mathbf{k}}[U^*_{\mathbf{k}}G_{\mathbf{k}}\Delta_{\mathbf{k}+\mathbf{Q}} + U_{\mathbf{k}}G^*_{\mathbf{k}}\Delta^*_{\mathbf{k}+\mathbf{Q}}] \\
&+ 2\epsilon_{\mathbf{k}+\mathbf{Q}}[\Delta_{\mathbf{k}}U^*_{\mathbf{k}}G^*_{\mathbf{k}} + \Delta^*_{\mathbf{k}}U_{\mathbf{k}}G_{\mathbf{k}}] \Big\}^{1/2},
\end{aligned}
\tag{1}
$$

where the Hamiltonian of the model is chosen as in [6]; $\Delta_{\mathbf{k}}$ is the order parameter in the superconducting phase; the real part of the parameter $G_{\mathbf{k}} = S_{\mathbf{k}} + iD_{\mathbf{k}}$ corresponds to the spatially modulated charge or, in other words, charge density waves (CDWs); and the imaginary part of this parameter corresponds to the orbital currents circulating in the neighboring unit cells in opposite directions. The imaginary part of $G_{\mathbf{k}}$ has the *d*-type symmetry, while its real part is characterized by the *s*-type symmetry [6]. In the underdoped samples, the critical temperature T^* of parameter D is higher than the superconducting transition temperature T_c. The parameter $U_{\mathbf{k}}$ describes the inhomogeneous state of the superconductor. According to [4], its value in the crystals under study is comparatively small.

The CDWs and orbital currents are decelerated and, in the limit, pinned by the lattice potential and defects, because the quasiparticle energy depends on the phase of order parameter. Let us substitute $G_{\mathbf{k}} = |G|e^{i\varphi}$ into Eq. (1) and trace how $E_{\mathbf{k}}$ depends on the phase φ. It is seen from Eq. (1) that the energy of a condensate of orbital currents and CDWs is independent of φ at $T_c < T < T^*$. The sliding charge–current states are not decelerated (at least in the mean-field approximation) and, hence, do not contribute to the broadening of the copper

NQR lines. It is also seen from Eq. (1) that the phase dependence appears as $\Delta_{\mathbf{k}}$ becomes nonzero, i.e., at $T = T_c$, and this dependence becomes stronger [proportional to $\Delta_{\mathbf{k}}(T)$ squared] upon lowering the temperature. Qualitatively, this explains a monotonic increase in the Cu(2) NQR line width at $T < T_c$. It also becomes clear that the broadening in overdoped samples is absent [3] because $|G| = 0$ in them.

For quantitative estimates, let us consider Fourier component of the spatially modulated charge on the copper nuclei:

$$e_Q = \frac{1}{N}\sum_j \delta_j \exp(-iQR_j), \tag{2}$$

where δ_j is the number of doped holes per unit cell of the CuO_2 bilayer and N is the number of unit cells. The homogeneous part δ_0 of the distribution does not contribute to e_Q. By separating the term proportional to $\Delta_{\mathbf{k}}$ in the charge modulation Fourier amplitude, one has, according to [6],

$$e_Q \approx \frac{2+\delta_0}{8N}\sum_{\mathbf{k}} \frac{\Delta_{\mathbf{k}}^2 (G_{\mathbf{k}} + G_{\mathbf{k}}^*)}{(E_{1\mathbf{k}}^2 - E_{2\mathbf{k}}^2)} \times \left[\frac{1}{E_{1\mathbf{k}}}\tanh\left(\frac{E_{1\mathbf{k}}}{2k_BT}\right) - \frac{1}{E_{2\mathbf{k}}}\tanh\left(\frac{E_{2\mathbf{k}}}{2k_BT}\right)\right]. \tag{3}$$

For simplicity, we restrict ourselves to the case $U_{\mathbf{k}} = 0$. Note that e_Q is zero if the real component of the pseudogap ($S_{\mathbf{k}}$) is absent. For numerical estimates, we specify the dispersion relation for quasiparticles as

$$\epsilon_{\mathbf{k}} = \frac{2+\delta_0}{2}[t_1(\cos k_x + \cos k_y) + 2t_2 \cos k_x \cos k_y + t_3(\cos 2k_x + \cos 2k_y)], \tag{4}$$

where $t_1 = 78$ meV, $t_2 = 0$, and $t_3 = 12$ meV [6]. In accordance with the photoemission data [7], we assume that $\Delta_{\mathbf{k}} = \Delta(T)(\cos k_x - \cos k_y)$, $D_{\mathbf{k}} = D(T)(\cos k_x - \cos k_y)$, and $\delta_0 \approx 0.3$. The difference between $|G_{\mathbf{k}}|$ and $|\cos k_x - \cos k_y|$ for underdoped $Bi_2Sr_2Ca_{1-x}Dy_xCu_2O_{8+y}$ at $T > T_c$ (see Fig. 2 in [7]) allows the relative value of the S component to be estimated as $S(T)/D(T) \approx 0.05$–0.1. For order-of-magnitude estimates, we ignore the dependence of $S_{\mathbf{k}}$ on the wave vector; i.e., we assume that $S_{\mathbf{k}}$ depends only on temperature. The electric field gradient at the copper nuclei is mainly composed of the lattice and valence contributions [8]. The valence contribution from the copper hole $d_{x^2-y^2}$ orbital dominates and equals approximately $V_{zz}(val) \approx 70$ MHz. In the presence of spatially modulated charge, the copper NQR line width can be estimated as $\Delta\nu \approx 2V_{zz}(val)e_Q$. The temperature dependence of line width thus calculated is shown in Fig. 2 by the solid line. Qualitatively, it agrees well with the experimental results. Agreement in order of magnitude is also observed. It is worth noting that Eq. (2) holds in the limit of slow CDW motion compared to the period of the probe field and does not assume that the CDWs are completely pinned.

A complete picture of the CDW effect on the line width, clearly, should include a contribution from the component that already exists at $T > T_c$. At $T < T^*$, it is given by the expression

$$e_Q' \approx \frac{2+\delta_0}{4N}\sum_{\mathbf{k}} \frac{S_{\mathbf{k}}}{E_{1\mathbf{k}} - E_{2\mathbf{k}}}[f(E_{1\mathbf{k}}) - f(E_{2\mathbf{k}})], \tag{5}$$

where

$$E_{1\mathbf{k},2\mathbf{k}} = \frac{\epsilon_{\mathbf{k}} + \epsilon_{\mathbf{k}+\mathbf{Q}}}{2} \pm \frac{1}{2}[(\epsilon_{\mathbf{k}} - \epsilon_{\mathbf{k}+\mathbf{Q}})^2 + 4|G_{\mathbf{k}}|^2]^{1/2}, \tag{6}$$

and $f(E_{\mathbf{k}})$ is the Fermi distribution function.

We did not observe the e_Q' component in our experiments; though noticeable in Fig. 2, the line broadening is very small in the region slightly above T_c. Within the framework of the picture suggested, this can be explained by the averaging of e_Q' over the relatively fast CDW motion above T_c. In this respect, an important role is played by the fact that the critical temperature of parameter $S(T)$ is smeared due to strong fluctuations that are inherent in the pseudogap phase. As is well known, these fluctuations are not taken into account in the mean-field approximation and, thus, require special calculations.

The presence of the S component can also be derived from the photoemission data for $Bi_2Sr_2Ca_{1-x}Dy_xCu_2O_{8+y}$ at $T > T_c$ [7]. However, its influence on the photoemission spectra is on the verge of experimental accuracy and, probably, was not revealed in [7] for this reason. In our case, the *iD* component does not contribute to the quadrupolar width, and, hence, the S component is more pronounced.

In summary, the measurements of the copper NQR line width in near-optimum doped $YBa_2Cu_3O_{7-y}$ have shown that it starts to increase monotonically at $T < T_c$, resembling, by its temperature dependence, the behavior of the order parameter for a superconducting gap. We relate the observed dependence to the presence of the S-type component in the order parameter of the pseudogap phase. We used the mean-field approximation to show that the energy of a condensate of charge–current states depends on the phase of order parameter only at $T < T_c$. The quantitative estimates agree with the experimental results.

This work was supported by the Russian program "Superconductivity" (project no. 98014-1) and, in part, by the BRHE (grant no. REC-007).

REFERENCES

1. D. Brinkmann, in *Materials and Crystallographic Aspects of HTc-Superconductivity* (Kluwer, Dordrecht, 1994), pp. 225–248.
2. S. Krämer and M. Mehring, Phys. Rev. Lett. **83**, 396 (1999).
3. K. Kumagai, K. Nozaki, and Y. Matsuda, Phys. Rev. B **63**, 144502 (2001).
4. M. V. Eremin, Yu. A. Sakhratov, A. V. Savinkov, *et al.*, Pis'ma Zh. Éksp. Teor. Fiz. **73**, 609 (2001) [JETP Lett. **73**, 540 (2001)].
5. R. Yu. Abdulsabirov, A. A. Bukharaev, M. R. Zhdanov, *et al.*, cond-mat/9808163.
6. S. V. Varlamov, M. V. Eremin, and I. M. Eremin, Pis'ma Zh. Éksp. Teor. Fiz. **66**, 726 (1997) [JETP Lett. **66**, 569 (1997)]; M. V. Eremin and I. A. Larionov, Pis'ma Zh. Éksp. Teor. Fiz. **68**, 583 (1998) [JETP Lett. **68**, 611 (1998)].
7. J. M. Harris, Z.-X. Shen, P. J. White, *et al.*, Phys. Rev. B **54**, R15665 (1996).
8. C. H. Pennington, D. J. Durand, C. P. Slichter, *et al.*, Phys. Rev. B **39**, 2902 (1989).

Translated by V. Sakun

JETP Letters, Vol. 74, No. 2, 2001, pp. 107–110. Translated from Pis'ma v Zhurnal Éksperimental'noĭ i Teoreticheskoĭ Fiziki, Vol. 74, No. 2, 2001, pp. 112–115.

New Relaxation Model for Superparamagnetic Particles in Mössbauer Spectroscopy

A. M. Afanas'ev and M. A. Chuev

Ioffe Physicotechnical Institute, Russian Academy of Sciences, ul. Krasikova 25a, Moscow, 117218 Russia

Received June 4, 2001; in final form, June 21, 2001

A new model is suggested for the relaxation in a system of superparamagnetic particles. The model takes into account the interparticle interaction and ensuing smearing of energy levels for each individual particle, such that the relaxation between the particle states with opposite directions of magnetic moment never occurs as a transition between the states of the same energy. This generalization of the relaxation model accounts for the diversity of relaxation Mössbauer absorption spectra, allowing all the nonstandard features that were observed previously in the experimental spectra of systems with small-sized particles to be described on a qualitative level. © *2001 MAIK "Nauka/Interperiodica".*

PACS numbers: 75.20.-g, 76.80.+y

A system of superparamagnetic particles is one of the most suitable objects of investigation in Mössbauer spectroscopy for the purpose of determining relaxation characteristics of such systems. Mössbauer spectroscopy easily perceives relaxation processes on the time scale 10^{-11}–10^{-6} s, i.e., the scale that corresponds to the relaxation times of superparamagnetic particles in the temperature range from ultralow to room temperatures and higher [1–7]. Beginning in the 1960s and up to the present time, the corresponding spectra have been analyzed using the so-called two-level relaxation model [8, 9], according to which the magnetic moment of an individual particle randomly reverses its direction, remaining parallel to the easy magnetic axis. In doing so, the particle has to overcome a rather high energy barrier U_0, so that the transition rate from one state to another is usually described by the formula suggested by Néel as early as the 1940s [10]:

$$p = p_0 \exp(-U_0/kT), \quad (1)$$

where p_0 is a constant, T is temperature, and k is the Boltzmann constant. In recent years, many attempts have been undertaken at refining the preexponential factor in Eq. (1) and determining its dependence on temperature and particle size. However, despite the great interest in this problem, the state of the art in this field cannot be regarded as being satisfactory. The experimental spectra do not fit the two-level model and necessitate introduction of a rather wide distribution over the particle sizes and, hence, over the magnetic anisotropy energies U_0 and relaxation constants p_0.

Strictly speaking, the two-level model is relevant only to systems with well-defined quantum levels, and its use for describing the relaxation of superparamagnetic particles comprising a large number of atoms (on the order of 10^3–10^5) is quite conjectural. The magnetic moment of the particle is large enough so that even weak interaction with the environment strongly smears its energy levels. As a consequence, the relaxation between the particle states with opposite directions of magnetic moment never proceeds as a transition between the levels with the same energy. On the average, the levels prove to be separated by a certain gap ΔE which may be rather large and comparable to temperature. It will be shown below that taking into account this fact gives rise to variously shaped relaxation Mössbauer spectra and allows one to qualitatively account for all the experimental data that were observed to date in this field.

Let us first turn to the standard two-level model. In the case where one may ignore the deviation of the magnetic moment from the direction of the easy magnetic axis, so that the hyperfine field $\mathbf{H}_{hf}$ at the nucleus can only be reversed during the relaxation, the cross section for absorption of a gamma-ray quantum is usually written as [9]

$$\varphi(\omega) = -\frac{\sigma_a \Gamma_0}{2} \sum_{\alpha} |C_\alpha|^2 \mathrm{Im}\langle W|(\tilde{\omega}\hat{1} - \hat{\omega}_\alpha + i\hat{P})^{-1}|1\rangle, \quad (2)$$

where $\tilde{\omega} = \omega + i\Gamma_0/2$; $\alpha = (M, m)$ labels the hyperfine transitions between the states with nuclear spin projections m and M onto the direction of the hyperfine field in the ground and excited states, respectively; the coefficients C_α are the intensities of the respective transitions; σ_a is the effective thickness of absorber; Γ_0 is the width of the nuclear excited level; $\langle W| = (1/2\ 1/2)$ is the

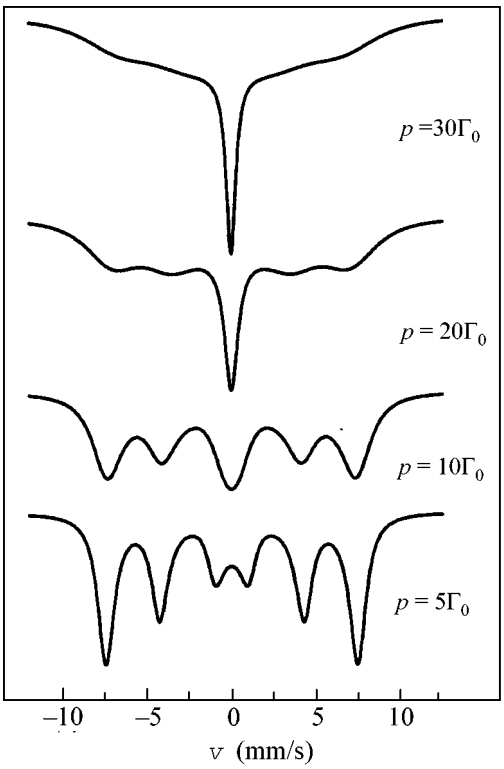

Fig. 1. Mössbauer absorption spectra in the standard two-level relaxation model for different relaxation rates p. Calculations are carried out for the ^{57}Fe nuclei with $\omega_{3/2,\,1/2} = 75\Gamma_0$.

state population vector; $\hat{1}$ is the identity matrix; $|1\rangle$ is the unit column;

$$\hat{\omega}_\alpha = \begin{pmatrix} \omega_\alpha & 0 \\ 0 & -\omega_\alpha \end{pmatrix} \tag{3}$$

is the matrix of hyperfine transitions; and

$$\hat{P} = \begin{pmatrix} p & -p \\ -p & p \end{pmatrix} \tag{4}$$

is the relaxation matrix. Here, $\omega_\alpha = M\omega_e - m\omega_g$, $\omega_{e,\,g} = g_{e,\,g}\mu_N H_{hf}$, μ_N is the nuclear magneton, and $g_{g,\,e}$ is the nuclear g factor in the ground and excited state of the nucleus, respectively.

Typical absorption spectra calculated by Eqs. (2)–(4) within the framework of the two-level model are shown in Fig 1. In the weak relaxation limit ($p < \omega_\alpha$ for all hyperfine transitions), a well-resolved magnetic hyperfine structure (sextet for the ^{57}Fe nuclei) is observed, with the lines identically broadened by $\Delta\Gamma = 2p$ and slightly shifted by a value proportional to $(p/\omega_\alpha)^2$ to the center of the spectrum. As the relaxation rate increases and the parameter p reaches the corresponding ω_α value, the line pairs due to the hyperfine transitions with spin projections m and M coinciding in magnitude but opposite in sign collapse successively. In the fast relaxation limit, the spectrum collapses into a single line (or a quadrupole doublet) (see, e.g., [9]). Examples can be found where the experimental Mössbauer spectra are satisfactorily described by this model.

However, lines of an unusual shape in no way fitting the above-mentioned model are observed in many studies [3–7]. If the hyperfine structure can still be resolved, the lines are highly asymmetric with steep outer and extended inward sides, as depicted in Fig. 2. To explain such spectra, one usually invokes models in which the particles are scattered in size. Up to now, no alternative explanation has been found to explain the lines of such an exotic shape.

As pointed out above, the possibility of applying the two-level relaxation model to the superparamagnetic particles requires a more thorough analysis; one should first of all take into account the fact that the states with oppositely directed moments are energetically separated due to interaction with the environment, so that the relaxation process always occurs between the differently populated states. We will call this model the generalized two-level (GTL) model.

To describe the Mössbauer spectra in this case, one can use the same Eq. (2) but with the relaxation matrix of a different form:

$$\hat{P}(\Delta E) = \begin{pmatrix} p_{12}(\Delta E) & -p_{12}(\Delta E) \\ -p_{21}(\Delta E) & p_{21}(\Delta E) \end{pmatrix}, \tag{5}$$

where $p_{12}(\Delta E)$ and $p_{21}(\Delta E)$ are, respectively, the transition rates from state 1 to state 2 and vice versa. We will assume that the interaction of a particle with the environment is weak; i.e., $\Delta E \ll U_0$. Then the energy of state 1 corresponding to positive projection of the particle magnetic moment onto the direction of a random magnetic field produced by the neighboring particles decreases by a value of ΔE, while, in turn, the energy of state 2 increases by the same value. In this case, to the terms proportional to a small parameter $\Delta E/U_0$, the energy of a particle remains maximal in the position where its magnetic moment is perpendicular to the easy magnetic axis. (A more accurate calculation of the energy barriers for single-domain particles with different orientations of easy magnetic axes in an arbitrary external field can be found, e.g., in the classical work of Stoner and Wohlfarth [11]). The following expression can then be obtained for the relaxation constants:

$$p_{12,\,21}(\Delta E) = p\exp(\mp\Delta E/kT), \tag{6}$$

where p is defined by Eq. (1). The populations of these states can be found from the detailed balance principle:

$$w_{1,\,2}(\Delta E) = \frac{\exp(\pm\Delta E/kT)}{\exp(\Delta E/kT) + \exp(-\Delta E/kT)}. \tag{7}$$

Equations (2), (3), and (5)–(7) can be used to calculate the absorption spectrum for a given ΔE.

The magnetic fields of the neighboring particles are random variables, and, hence, the corresponding energy shifts ΔE are scattered over a certain interval. The simplest distribution function for ΔE can be taken in the Gaussian form

$$P(\Delta E, \sigma) = \frac{1}{\sqrt{2\pi}\sigma}\exp\left(-\frac{(\Delta E)^2}{2\sigma^2}\right). \quad (8)$$

The corresponding absorption cross section is determined by the energy distribution width σ:

$$\bar{\varphi}(\omega) = \int_{-\infty}^{\infty} \varphi(\omega, \Delta E) P(\Delta E, \sigma) d(\Delta E). \quad (9)$$

In the fast relaxation limit $p \gg \omega_\alpha^2/\Gamma_0$, this expression takes the form of a continuous distribution of Lorentzian lines with natural width Γ_0:

$$\bar{\varphi}(\omega) = \frac{\sigma_a \Gamma_0^2}{4}\sum_\alpha |C_\alpha|^2 \times \int_{-\infty}^{\infty} \frac{1}{[\omega - \bar{\omega}_\alpha(\Delta E)]^2 + \Gamma_0^2/4} P(\Delta E, \sigma) d(\Delta E), \quad (10)$$

where the stochastically mean hyperfine transition frequencies

$$\bar{\omega}_\alpha(\Delta E) = \omega_\alpha \tanh(\Delta E/kT) \quad (11)$$

specify the positions of spectral lines corresponding to the energy shift ΔE and $P(\Delta E, \sigma)$ are their intensities. One can see from Eq. (10) that the line shapes in the GTL model are asymmetric and fully determined by the width σ of energy distribution (8) and by temperature.

The absorption spectra calculated using Eq. (9) are shown in Fig. 2. One can see that the relaxation spectra in the generalized relaxation model differ drastically from those calculated with the standard two-level model (Fig. 1). First and foremost, the inclusion of the interaction of particles with the environment leads to a substantial slowing down of the relaxation process, as is clearly seen from the comparison of the diffuse upper spectrum in Fig. 1 ($p = 30\Gamma_0$) with the left spectra in Fig. 2, where the resolved hyperfine structure is observed even for σ values small compared to temperature. In a qualitative sense, the appearance of asymmetrically shaped lines with extended inward wings is the most salient feature of the GTL spectra. Lines of this type are frequently observed in the experimental Mössbauer spectra of superparamagnetic particles (see, e.g., [3–7] and references therein). As a rule, the line shapes of this type are explained using the standard two-level model with size distribution of particles [2]. As to the spectra in Fig. 2, they are calculated for a system of superparamagnetic particles of the same size.

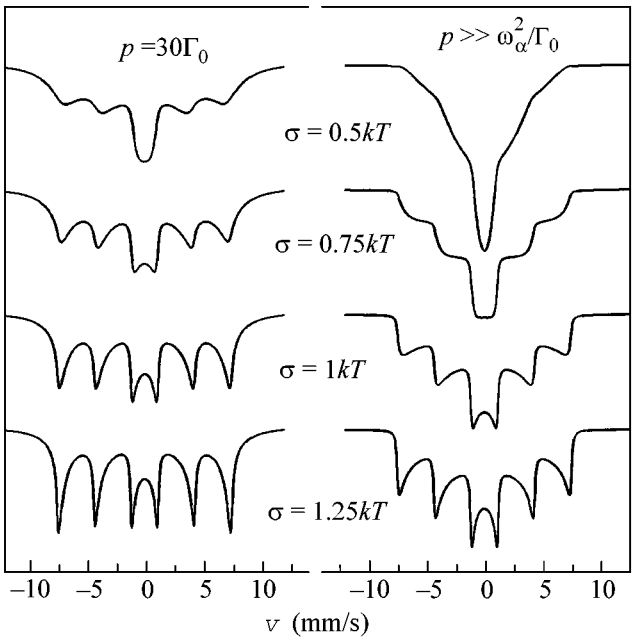

Fig. 2. Absorption spectra of a system of superparamagnetic particles of the same size in the generalized two-level relaxation model for $p = 30\Gamma_0$ and in the fast relaxation limit and for different distribution widths σ of energy shift.

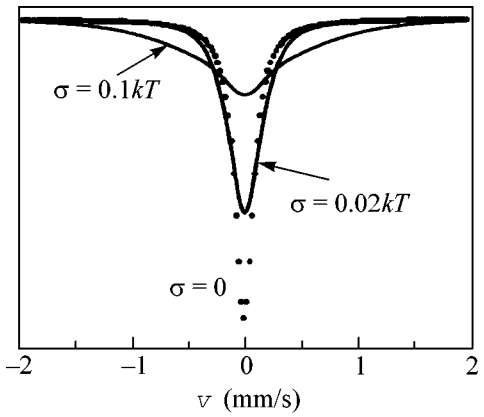

Fig. 3. Absorption spectra in the GTL model for small σ values (solid lines) and in the standard two-level model (dots) in the fast relaxation limit.

The most important feature of the Mössbauer absorption spectra in the GTL model is that, even in the fast relaxation limit, the spectra do not collapse into a single line and exhibit a well-resolved hyperfine structure if σ is on the order of kT (Fig. 2, right). In such a situation, the magnetic hyperfine structure collapses not because of an increase in the relaxation rate but as a result of the competition between the parameters σ and kT. At high temperatures, $kT \gg \sigma$, the spectra collapse into a single line. However, it is seen from Fig. 3

that the spectra in the above two models differ substantially in shape even at very small values of σ (on the order of several hundredths of kT).

Up to now, the interaction between superparamagnetic particles has been investigated in the context of both magnetic dynamics of such systems and analysis of their Mössbauer spectra. However, the main efforts have been focused on refining Eq. (1) and on the influence of this interaction on the barrier heights. In a number of studies (see, e.g., [3]), the problem of transition of a system of superparamagnetic particles into the ordered superferromagnetic state was analyzed. If this transition occurs, one should expect that the lines will undergo an additional shift with changing temperature, but their shapes will not change appreciably. Therefore, the Mössbauer spectra of the type shown in Fig. 2 are theoretically described in this work.

The GTL model suggested in this work does not deny the distribution of particles over their sizes because the corresponding scatter always occurs in a system of paramagnetic particles. However, it is clear that the analysis with inclusion of both factors will lead to an essentially different distribution compared to those reproduced using the standard two-level model.

It is worth noting that the theory of relaxation Mössbauer spectra of a system of mutually interacting superparamagnetic particles must self-consistently take into account, along with the relaxation of an individual particle and the scatter of ΔE over a certain interval, the variation of ΔE with time. The corresponding analysis makes the theory much more complicated and is beyond the scope of this work. However, it is clear that the main qualitative conclusions of the simplified GTL model are the same as in more complicated relaxation models.

REFERENCES

1. J. M. Williams, D. P. Danson, and C. Janot, Phys. Med. Biol. **23**, 835 (1978).
2. N. M. K. Reid, D. P. E. Dickson, and D. H. Jones, Hyperfine Interact. **56**, 1487 (1990).
3. S. Mørup, Hyperfine Interact. **90**, 171 (1994).
4. E. Tronc, P. Prene, J. P. Jolivet, *et al.*, Hyperfine Interact. **95**, 129 (1995).
5. J. L. Dormann, F. D'Orazio, F. Lucari, *et al.*, Phys. Rev. B **53**, 14291 (1996).
6. I. P. Suzdalev, A. S. Plachinda, V. N. Buravtsev, *et al.*, Chem. Phys. Rep. **17**, 1355 (1998).
7. E. Tronc, A. Ezzir, R. Cherkaoui, *et al.*, J. Magn. Magn. Mater. **221**, 63 (2000).
8. A. Abraham, *The Theory of Nuclear Magnetism* (Oxford Univ. Press, London, 1961).
9. H. H. Wickman, in *Mössbauer Effect Methodology*, Ed. by I. J. Gruverman (Plenum, New York, 1966), Vol. 2.
10. L. Neel, Ann. Geophys. **5**, 99 (1949).
11. E. C. Stoner and E. P. Wohlfarth, Philos. Trans. R. Soc. London, Ser. A **240**, 599 (1948).

Translated by V. Sakun

JETP Letters, Vol. 74, No. 2, 2001, pp. 111–114. Translated from Pis'ma v Zhurnal Éksperimental'noĭ i Teoreticheskoĭ Fiziki, Vol. 74, No. 2, 2001, pp. 116–119.

Symmetry of the Order Parameter in the UGe_2 Superconductor

I. A. Fomin

Kapitsa Institute for Physical Problems, Russian Academy of Sciences, Moscow, 117334 Russia

e-mail: fomin@kapitsa.ras.ru

Received June 14, 2001; in final form, June 21, 2001

For the UGe_2 ferromagnetic superconductor, the forms of the order parameter are determined with allowance for the crystal symmetry and with the assumption that a strong spin–orbit interaction is present in the system. The limiting case corresponding to the immediate vicinity of the simultaneous transition to the superconducting and ferromagnetic phases is considered. The opposite limit corresponding to a wide separation of the Fermi surfaces with opposite spin orientations is considered as well. Possible effects of the ferromagnetic domain structure on the properties of UGe_2 in the superconducting state are discussed. © *2001 MAIK "Nauka/Interperiodica".*

PACS numbers: 74.25.Dw; 75.50.Cc; 74.70.Ad

1. The superconductivity recently observed in a UGe_2 band ferromagnet [1, 2] is of interest, because the Curie temperature T_c of this compound is high compared to the superconducting transition temperature T_s everywhere except for the pressure $P_c \approx 16$ kbar, at which both temperatures are equal to zero. The condition $T_c \gg T_s$ rules out the possibility of a singlet Cooper pairing. The question about the possible form of the order parameter in the superconducting phase of UGe_2 was recently discussed in the literature [3]. Physical arguments were presented in favor of the existence of the superconducting state of UGe_2 with the order parameter similar to that of the A_1 phase of ^{3}He, i.e., of a system where the electrons with only one spin direction are paired, whereas the electrons with the opposite spin direction have a gapless energy spectrum. However, in the paper cited, it was noted that the desired order parameter cannot be constructed using the basis functions of four one-dimensional representations of the point symmetry group characterizing orthorhombic crystals such as UGe_2 if the conventional strong spin–orbit interaction scheme is applied. Below, this statement is shown to be invalid: it does not take into account the fact that, in UGe_2, the transition to the superconducting phase occurs from the ferromagnetic phase, and, hence, the time reversal is no symmetry element of the normal phase. Then, the order parameter of the A_1-phase type can be realized in the presence of a strong spin–orbit interaction. This paper presents the list of the types of the superconducting order parameters that are allowed by the UGe_2 crystal symmetry. The consideration follows the standard theory of phase transitions [4] and the classification scheme [5] developed for the superconducting order parameters of crystals (see also [6]).

2. A UGe_2 crystal possesses an inversion center. This allows one to separate the superconducting phases into even and odd ones (singlet and triplet pairing analogs, respectively). As applied to UGe_2, the odd case is of most interest, and, hence, it is selected for the following consideration. In the presence of a strong spin–orbit interaction, the order parameter for this case can be represented in the form [5]

$$\mathbf{d}(\mathbf{k}) = \hat{\mathbf{x}} f_x(\mathbf{k}) + \hat{\mathbf{y}} f_y(\mathbf{k}) + \hat{\mathbf{z}} f_z(\mathbf{k}), \qquad (1)$$

where $\hat{\mathbf{x}}$, $\hat{\mathbf{y}}$, and $\hat{\mathbf{z}}$ are the unit vectors along the binary axes **b**, **c**, and **a**, respectively. The **a** axis coincides with the direction of easy magnetization in the ferromagnetic phase. All functions $f_{x,y,z}(\mathbf{k})$ are odd, i.e., $f_x(-\mathbf{k}) = -f_x(\mathbf{k})$, etc. The symmetry of the directions in the paramagnetic phase of UGe_2 corresponds to the group $D_{2h} = D_2 \times C_i$. Since the type of symmetry with respect to an inversion is fixed, it is sufficient to consider the D_2 group, which has four one-dimensional representations (see table).

Table

$D_2, D_2(C_2)$	E	$C_2^x; RC_2^x$	$C_2^y; RC_2^y$	C_2^z
A	1	1	1	1
B_1	1	–1	–1	1
B_2	1	–1	1	–1
B_3	1	1	–1	–1

0021-3640/01/7402-0111$21.00

The symmetry group of the ferromagnetic phase is the $D_2(C_2)$ magnetic group (see [7]); instead of the C_2^x and C_2^y elements, it contains the RC_2^x and RC_2^y elements, where R is the time reversal operation. The $D_2(C_2)$ group is isomorphic with the initial D_2 group, but the forms of their basis functions are different. By the A representation of the $D_2(C_2)$ group, the following functions are transformed:

$$\Psi_A = \hat{\mathbf{x}}k_x(u_{11}^A + ik_xk_yu_{10}^A) + \hat{\mathbf{y}}k_y(u_{22}^A + ik_xk_yu_{20}^A) + \hat{\mathbf{z}}k_z(u_{33}^A + ik_xk_yu_{30}^A), \quad (2)$$

where $u_{11}^A \ldots$ are real functions of k_x^2, k_y^2, and k_z^2. Similarly, we have

$$\Psi_{B_1} = \hat{\mathbf{x}}k_y(u_{12}^{B_1} + ik_xk_yu_{10}^{B_1}) + \hat{\mathbf{y}}k_x(u_{21}^{B_1} + ik_xk_yu_{20}^{B_1}) + \hat{\mathbf{z}}k_z(iu_{33}^{B_1} + k_xk_yu_{30}^{B_1}), \quad (3)$$

$$\Psi_{B_2} = \hat{\mathbf{x}}k_z(u_{13}^{B_2} + ik_xk_yu_{10}^{B_2}) + \hat{\mathbf{y}}k_z(u_{23}^{B_2} + k_xk_yu_{20}^{B_2}) + \hat{\mathbf{z}}k_x(u_{31}^{B_2} + ik_xk_yu_{30}^{B_2}), \quad (4)$$

$$\Psi_{B_3} = \hat{\mathbf{x}}k_z(iu_{13}^{B_3} + k_xk_yu_{10}^{B_3}) + \hat{\mathbf{y}}k_z(u_{23}^{B_3} + ik_xk_yu_{20}^{B_3}) + \hat{\mathbf{z}}k_y(u_{32}^{B_3} + ik_xk_yu_{30}^{B_3}). \quad (5)$$

All four order parameters generally correspond to nonunitary phases, which have a nonzero z projection of the magnetic moment. This projection is proportional to $\langle\Psi \times \Psi^\star\rangle$, where the angular brackets denote averaging over the directions of $\mathbf{k}$. Functions (2)–(5) take into account only the symmetry constraints for the order parameter and, therefore, allow some arbitrariness. This arbitrariness can be reduced by taking into account the quantitative relations between the physical quantities in UGe_2. Because of the condition $T_c \gg T_s$, the pairing amplitude for electrons with opposite spin projections must be zero. In vector notation, this condition is equivalent to $\mathbf{d}_z = 0$, which allows us to drop all terms proportional to $\hat{\mathbf{z}}$ in functions (2)–(5).

At the point $P = P_c$, $T = 0$, the transition to the superconducting phase and, simultaneously, to the ferromagnetic phase occurs directly from the paramagnetic phase. Away from this critical point, the transition to the ferromagnetic phase is a first-order phase transition. The precision of the available data does not allow us to determine the type of the transition at the very critical point. If the transition is continuous, then, in the vicinity of this point in the phase diagram, the superconducting order parameter must be described by a basis function of one of the representations of the D_2 group [4]. It is easy to verify that expressions (2)–(5) really pass into the basis functions of the corresponding representations of the D_2 group on condition that all terms explicitly involving the imaginary unit, i.e., the functions u_{10}^A, u_{20}^A, etc., become zero at the critical point. In this case, all phases become unitary, the vector $\mathbf{d}(\mathbf{k})$ becomes real correct to a factor, and the pairing amplitudes $\Delta_{\uparrow\uparrow} \sim -d_x + id_y$ and $\Delta_{\downarrow\downarrow} \sim d_x + id_y$ become equal in magnitude. However, this is true only in the vicinity of the critical point. With distance from P_c, the difference between the two amplitudes should increase. One of the amplitudes, e.g., $\Delta_{\downarrow\downarrow}$, can vanish, which, in terms of the components of the vector $\mathbf{d}(\mathbf{k})$, means $d_x(\mathbf{k}) = -id_y(\mathbf{k})$. For this equality to be satisfied, it is sufficient to choose the appropriate coefficients $u_{22}^A, \ldots$. Then, the order parameter will have the form $\mathbf{d}(\mathbf{k}) = f(\mathbf{k})(-\hat{\mathbf{x}} + i\hat{\mathbf{y}})$ for all four representations. Different representations differ only in the form of the function $f(\mathbf{k})$: $f^A(\mathbf{k}) = -k_x(u_{11}^A + ik_xk_yu_{10}^A)$, $f^{B_1}(\mathbf{k}) = -k_y(u_{12}^{B_1} + ik_xk_yu_{10}^{B_1})$, $f^{B_2}(\mathbf{k}) = -k_z(u_{13}^{B_2} + ik_xk_yu_{10}^{B_2})$, and $f^{B_3}(\mathbf{k}) = -k_z(iu_{13}^{B_3} + k_xk_yu_{10}^{B_3})$. Thus, in the case of a strong spin–orbit interaction, the symmetry selection rule that excludes the order parameter of the type $\mathbf{d}(\mathbf{k}) = f(\mathbf{k})(-\hat{\mathbf{x}} + i\hat{\mathbf{y}})$ is effective only near the critical pressure and only when the phase transition at $P = P_c$ is a second-order transition.

We note that the magnetization itself is transformed according to the representation B_1 of the D_2 group (see table). The coincidence of two transitions at the critical point can be either accidental or indicative of a common origin of these two transitions. If we assume that the second case is realized and a single microscopic control parameter exists for the two transitions, the transition at the critical point can be characterized by one order parameter whose components are represented by the magnetization $\mathbf{M}$ and the vector $\mathbf{d}(\mathbf{k})$. By virtue of the general statement that a change of symmetry accompanies a phase transition, all components of the order parameter near the transition should be transformed by one representation of the symmetry group of the symmetric phase; i.e., near P_c, the quantity $\mathbf{d}(\mathbf{k})$ will have the form given by Eq. (3). This form of $\mathbf{d}(\mathbf{k})$ will be retained along the phase transition line up to the point of intersection with the line of another phase transition. Experimentally, no transitions were observed in the superconducting phase up to the pressure P = 13.5 kbar, at which a qualitative change occurred in the temperature dependence of the upper critical field.

In the case of an accidental coincidence of the transitions, $\mathbf{d}(\mathbf{k})$ can have the form given by any of expressions (2)–(5).

3. The spin direction of the dominant amplitude is determined by the magnetization direction. If a UGe_2 ferromagnetic sample consists of magnetic domains, then, away from $P = P_c$, the spin pairing in every single domain occurs for spins with only one orientation, this

orientation alternating from one domain to another. The properties of such a layered (in the simplest case) structure as an electric conductor should differ considerably from the properties of a domain structure with singlet pairing (see [8]). In the singlet case, the superconductivity localized at the domain walls can exist in stronger magnetic fields than the bulk superconductivity. By contrast, in UGe_2, one should expect a suppression of the order parameter at the domain walls, which in this case become weak links. However, this issue needs special analysis. A simpler subject from the viewpoint of both calculation and experiment is the study of the effect of the superconducting transition on the magnetization curve of the ferromagnetic UGe_2 (the dependence **M**(**H**)).

Let us consider a sample in the form of a plate cut normally to the easy magnetization axis. We also assume that the magnetic field is directed normally to the plate. The equilibrium domains exist in the plate in magnetic fields below $4\pi M$. For UGe_2, this value is about 2 to 3 kOe. The domain width is determined by the competition of the domain wall energy with the energy of the magnetic field produced by the plate. For a 0.1-cm-thick plate, with realistic assumptions made for the anisotropy energy, we obtain the estimate for the domain width within 10^{-3}–10^{-4} cm, which is much greater than the correlation length $\xi \sim 10^{-6}$ cm. This result allows us to treat each domain as a massive superconductor. The typical fields inside the domains are about 1 kOe, which is high compared to the estimate for the thermodynamic critical field ($H_{cm} \sim 100$ Oe). Therefore, one should expect that each domain is in a mixed state. In every domain, the field averaged over the vortex structure is expressed as $\mathbf{B} = \mathbf{H} + 4\pi(\mathbf{M_F} + \mathbf{M_s})$, where the magnetization is a sum of the spontaneous magnetization $\mathbf{M_F}$ and the magnetization due to the superconducting currents $\mathbf{M_s}$. We assume that the dependence $\mathcal{M}_s(H_{ext})$ is known (for magnetic superconductors, this dependence was recently discussed in the literature [9]). The role of the external field H_{ext} is played by the combination $\mathbf{B} = \mathbf{H} + 4\pi\mathbf{M_F}$. If the domain walls are not fixed and the structure is an equilibrium one, we have $\mathbf{H} = 0$. In this case, the effect of superconductivity is reduced to a decrease in the saturation magnetization down to the value $M_F + \mathcal{M}_s(4\pi M_F)$ in every domain. If the field $\mathcal{H}$ in which the sample is placed satisfies the condition $\mathcal{H} < \mathcal{H}^* = 4\pi(M_F + \mathcal{M}_s(4\pi M_F))$, the mean magnetization of the plate will be $\langle M\rangle = \mathcal{H}/4\pi$. In higher magnetic fields, no domains are formed. With allowance for the boundary condition, we have $\mathcal{H} = H_{ext} + 4\pi M_s$. The induced magnetization M_s is determined from the equation $M_s = \mathcal{M}_s(\mathcal{H} - 4\pi M_s)$. At $\mathcal{H} = \mathcal{H}^*$, this equation has the solution $M_s = \mathcal{M}_s(4\pi M_F)$, and at $\mathcal{H} = H_{c2}$, it has the solution $M_s = 0$. For fields close to the upper critical one H_{c2}, the dependence $\mathcal{M}_s(H_{ext})$ is linear [10]. In this case, $\mathcal{H}^* = 4\pi M_F + (4\pi M_F - H_{c2})/q$, where $q = (2\kappa^2 - 1)\beta_A$, κ is the Ginzburg–Landau parameter, and β_A is a numerical parameter ~1 depending on the geometry of the vortex lattice. When $\mathcal{H} < \mathcal{H}^*$, we have $\langle M\rangle = \mathcal{H}/4\pi$, as in the case of a normal ferromagnetic plate. The deviation from a normal ferromagnet occurs in the interval $\mathcal{H}^* < \mathcal{H} < H_{c2}$. For $\mathcal{H}$ close to H_{c2}, we obtain

$$M = M_F + \frac{\mathcal{H} - H_{c2}}{4\pi(q+1)}. \tag{6}$$

In the presence of a domain wall pinning, the magnetization curve exhibits a hysteresis. The shape of the hysteresis loop depends on the specific properties of the sample. In the fields close to H_{c2}, we can determine the diamagnetic additive to the magnetization, if we assume that the transition to the superconducting state does not affect the positions of the domain walls. The averaging over the domains should be performed by taking into account that, depending on the orientation of the magnetization, the field **H** is either added to $4\pi\mathbf{M}_F$ or subtracted from it. As a result, we obtain

$$\langle M\rangle = \langle M\rangle_0 + \frac{1}{q+1}\left[\frac{\mathcal{H}}{4\pi} - \langle M\rangle_0\right]. \tag{7}$$

For the domains to exist in a wide interval of fields, it is necessary to assume that the parameter κ is large, i.e., the correction to the magnetization is small. From Eq. (7), one can see that the correction appears in the region where the hysteresis is observed, and the sign of the correction corresponds to the narrowing of the hysteresis loop.

Thus, these ferromagnetic and, simultaneously, superconducting domain structures deserve further investigation.

The major part of this work was completed at the Grenoble Research Center of the Commissariat for Atomic Energy, France. I am grateful to J. Flouquet for hospitality at this research center and for stimulating discussions. I appreciate the financial support provided to me by the Joseph Fourier University during my visit to Grenoble. I am grateful to V.P. Mineev and A. Huxley for valuable comments.

REFERENCES

1. S. S. Saxena, P. Agarwal, K. Ahilan, *et al.*, Nature **406**, 587 (2000).
2. A. Huxley, I. Sheikin, E. Ressouche, *et al.*, Phys. Rev. B **63**, 144519 (2001).
3. K. Machida and T. Ohmi, Phys. Rev. Lett. **86**, 850 (2001).

4. L. D. Landau and E. M. Lifshitz, in *Course of Theoretical Physics*, Vol. 5: *Statistical Physics* (Nauka, Moscow, 1995; Pergamon, Oxford, 1980), Part 1, Chap. XIV.

5. G. E. Volovik and L. P. Gor'kov, Zh. Éksp. Teor. Fiz. **88**, 1412 (1985) [Sov. Phys. JETP **61**, 843 (1985)].

6. V. P. Mineev and K. V. Samokhin, *An Introduction to the Theory of Unusual Superconductivity* (MFTI, Moscow, 1998).

7. L. D. Landau and E. M. Lifshitz, in *Course of Theoretical Physics*, Vol. 8: *Electrodynamics of Continuous Media* (Nauka, Moscow, 1982; Pergamon, New York, 1984), Chap. V.

8. L. N. Bulaevskii, A. I. Buzdin, M. L. Kulić, and S. V. Panjukov, Adv. Phys. **34**, 175 (1985).

9. E. B. Sonin and I. Felner, Phys. Rev. B **57**, R14000 (1998).

10. A. A. Abrikosov, in *Fundamentals of the Theory of Metals* (Nauka, Moscow, 1987; North-Holland, Amsterdam, 1988), Chap. XVIII.

Translated by E. Golyamina

JETP Letters, Vol. 74, No. 2, 2001, pp. 115–117. Translated from Pis'ma v Zhurnal Éksperimental'noĭ i Teoreticheskoĭ Fiziki, Vol. 74, No. 2, 2001, pp. 120–122.

Giant Thermal Hysteresis of Sound Velocity and Internal Friction in a $La_{0.8}Sr_{0.2}MnO_3$ Single Crystal

R. I. Zaĭnullina[1], N. G. Bebenin[1]*, A. M. Burkhanov[1], V. V. Ustinov[1], Ya. M. Mukovskiĭ[2], and A. A. Arsenov[2]

[1] *Institute of Metal Physics, Ural Division, Russian Academy of Sciences, Yekaterinburg, 620219 Russia*
* *e-mail: bebenin@imp.uran.ru*
[2] *Moscow State Institute of Steel and Alloys, Moscow, 117936 Russia*

Received June 25, 2001

Temperature dependences of the velocity of longitudinal sound V_1 and the internal friction Q^{-1} are studied for a $La_{0.8}Sr_{0.2}MnO_3$ single crystal in the temperature range 5–350 K. The latter includes the temperature of the structural phase transition $T_s \approx 95$ K (from the *Pnma* orthorhombic low-temperature phase to the $R\bar{3}c$ rhombohedral high-temperature one) and the Curie point $T_c = 308$ K. Near the temperatures T_s and T_c, the curves $V_1(T)$ and $Q^{-1}(T)$ exhibit pronounced singularities. Outside the vicinities of T_s and T_c, the velocity of sound monotonically decreases with increasing temperature. A thermal hysteresis of giant width is observed in the aforementioned dependences. The hysteresis is attributed to the following mechanism: when the crystal under study is heated starting at temperatures $T < T_s$, some regions occupied by the *Pnma* low-temperature phase are retained in the $R\bar{3}c$ matrix up to the temperature $T = 350$ K. © *2001 MAIK "Nauka/Interperiodica".*

PACS numbers: 62.65.+k, 64.70.Kb

The interest in lanthanum manganites, $La_{1-x}D_xMnO_3$ (where D is a two-valent ion, such as Ca, Sr, Ba, or Pb), as well as in other rare-earth manganites, is caused by the colossal magnetoresistance (CMR) observed in these materials near the Curie point T_c [1–4]. The CMR manganites are characterized by a strong interaction between the electron, spin, and lattice degrees of freedom. The coupling between the conduction electrons and the magnetic subsystem is obvious from the very fact of the observation of the large magnetoresistance near T_c, and the interaction between the magnetic and lattice subsystems is evidenced by, e.g., the large magnetostriction [5] and the considerable shift of the structural transition temperature T_s under an external magnetic field H [6, 7]. The characteristic feature of the CMR manganites is the tendency for a phase separation. Most studies described in the literature are concerned with layering into regions that have different types of conduction or different magnetic orders [1, 8, 9]. Some publications also report on the observation of inclusions of a low-symmetry phase in a higher symmetry matrix [10].

Although the role of the crystal lattice in the formation of the CMR manganite properties is generally recognized, the lattice properties of these materials remain poorly understood. We studied the temperature dependence of the velocity of longitudinal sound V_1 and the temperature dependence of the internal friction Q^{-1} in a $La_{0.8}Sr_{0.2}MnO_3$ single crystal in a wide temperature range, which included both the structural transition from the *Pnma* orthorhombic low-temperature phase to the $R\bar{3}c$ rhombohedral high-temperature phase and the Curie point T_c. We also studied the magnetic properties of this crystal. The results of our studies offer some conclusions about the magnetic and crystalline states of the aforementioned crystal at different temperatures.

The $La_{0.8}Sr_{0.2}MnO_3$ single crystal was grown by the floating zone method with a radiation heating. A detailed description of the growth process can be found in the literature [11]. The magnetization of the crystal was measured on a ball-shaped sample by a vibrating-sample magnetometer in the temperature range 77–380 K. The sound velocity and the internal friction were studied in the temperature range 5–350 K by the compound vibrator technique [12] at frequencies about 80 kHz. The technique is based on the measurement of the resonance frequency and the Q factor of the mechanical system consisting of the sample under study and a piezoelectric transducer attached to it. For these measurements, we used a sample in the form of a cylinder 28 mm in length and 3.5 mm in diameter. The transducer was a conventional crystal vibrator producing longitudinal vibrations. The measurements were performed in a gaseous helium atmosphere. The method used for calculating the sound velocity and the internal friction in the sample was described in the literature [13]. Both cooling and heating of the sample occurred at rates not exceeding 0.5 K/min. The manga-

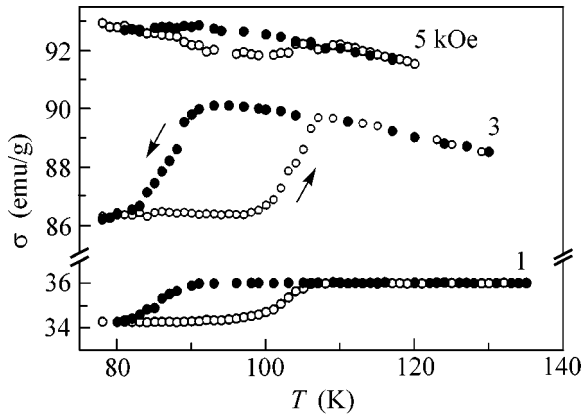

Fig. 1. Temperature dependence of the magnetization σ in the region of the structural phase transition. Empty circles correspond to heating, and full circles correspond to cooling.

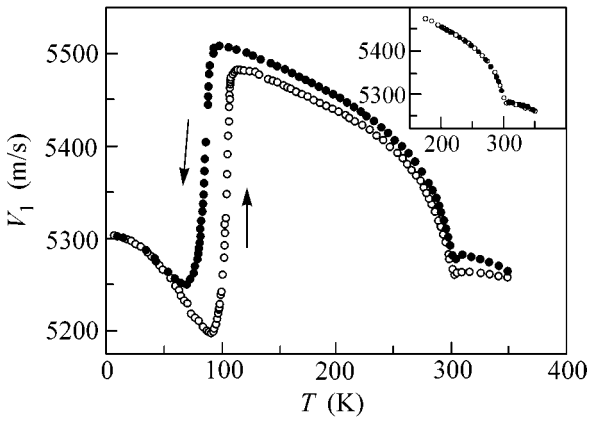

Fig. 2. Temperature dependence of the velocity of longitudinal sound V_1. The inset shows the sound velocity for the case of cooling from 350 to 175 K and a subsequent heating.

nite under study is a typical ferromagnet. At $T = 77$ K in the field $H = 5$ kOe, its magnetization is $\sigma = 92.7$ emu/g, which corresponds to the magnetic moment of a manganese ion $3.8\mu_B$. The Curie point determined by the method of thermodynamic coefficients is 308 K. These values of the magnetic moment and the Curie point practically coincide with the data reported in [14]. In the paramagnetic region, the temperature dependence of the magnetic susceptibility obeys the Curie–Weiss law with the paramagnetic Curie temperature $\theta_c = 310$ K. The close values of T_c and θ_c attest to the magnetic homogeneity of the sample.

The temperature dependence of the magnetization exhibits a hysteresis near the structural phase transition (Fig. 1). The transition temperature T_s can be conveniently determined as a half-sum of the temperatures corresponding to the maximal slopes of the curves $\sigma(T)$ recorded in the cooling and heating runs at a constant magnetic field. The structural phase transition temperature determined in this way is $T_s \approx 95$ K. The noticeable amplitude of the thermal hysteresis loop $\Delta\sigma$ observed in the region of technical magnetization (the curves corresponding to 1 and 3 kOe) is an indication of a change in the magnetic anisotropy under the *Pnma* $\longrightarrow$ $R\bar{3}c$ transformation. In the true magnetization region, $H >$ 5 kOe, the difference in the magnetization values for the *Pnma* and $R\bar{3}c$ phases is small and reaches approximately 0.7 emu/g, which is equal to the value of $\Delta\sigma$ obtained for a $La_{0.8}Ba_{0.2}MnO_3$ single crystal in our earlier study [7]. The width of the thermal hysteresis loop is independent of the magnetic field and is approximately equal to 25 K. In the temperature regions $T >$ 105 K and $T < 80$ K, the curves $\sigma(T)$ obtained in the cooling and heating runs coincide.

The temperature dependence of the velocity of longitudinal sound $V_1(T)$ is shown in Fig. 2. Near T_s, at the transition from the *Pnma* low-temperature phase to the $R\bar{3}c$ high-temperature phase, the velocity V_1 increases drastically. The transition from the ferromagnetic to paramagnetic state manifests itself as a characteristic minimum at $T = 304$ K. Outside the vicinities of T_s and T_c, the sound velocity monotonically decreases with increasing temperature, the dependence of V_1 on T being fairly weak in the paramagnetic state. We note that, in the $La_{0.85}Sr_{0.15}MnO_3$ manganite whose composition is close to that of the sample under study, a considerable growth of V_1 with temperature was observed in the region $T > T_c$ [15].

A distinctive feature of the temperature dependence of the longitudinal sound velocity obtained for the $La_{0.8}Sr_{0.2}MnO_3$ single crystal is the giant width of the thermal hysteresis loop. The coincidence of the curves obtained in the cooling and heating runs is observed for $T < 50$ K and $T > 350$ K. The width of the hysteresis loop is about 300 K, which is approximately three times as great as the value of T_s. From Fig. 2, one can see that the hysteresis loop is asymmetric: its part extending from T_s to higher temperatures occupies a much greater temperature interval than the part lying in the region $T < T_s$. The value of Q^{-1} is small at the helium temperature (Fig. 3). An increase in T leads to an increase in the internal friction. Near the points T_s and T_c, the curve $Q^{-1}(T)$ exhibits maxima. Within the interval $120 < T <$ 280 K, the value of Q^{-1} depends weakly on temperature. In the paramagnetic region, the internal friction increases with increasing T. The thermal hysteresis occurs in the interval $60 < T < 350$ K.

The giant width of the thermal hysteresis loops observed in the dependences $V_1(T)$ and $Q^{-1}(T)$ presumably indicates that, when the $La_{0.8}Sr_{0.2}MnO_3$ single crystal is heated starting from temperatures that are lower than the temperature of the *Pnma* $\longrightarrow$ $R\bar{3}c$ transformation, some regions with the *Pnma* orthorhombic structure are retained inside the $R\bar{3}c$ rhombo-

hedral matrix up to T = 350 K. One of the factors responsible for such a coexistence of phases can be a large scatter that occurs in the values of the structural phase transformation temperature due to the inhomogeneity of the sample. However, if the hysteresis were caused by the scatter in the *Pnma* $\longrightarrow$ $R\bar{3}c$ transition temperature, the hysteretic behavior would be observed in any region within the interval $100 < T < 350$ K. As one can see from the inset in Fig. 2, no hysteresis occurs when the sample is cooled from 350 to 175 K and then heated. Hence, the aforementioned coexistence of phases is caused not by the scatter in the structural phase transition temperature, but by the proximity of the thermodynamic potentials of the two phases. This conclusion agrees well with the fact that the latent heat of the *Pnma* $\longrightarrow$ $R\bar{3}c$ transition in lanthanum manganites is small: e.g., for a $La_{0.85}Sr_{0.15}MnO_3$ single crystal [16], it was found to be $q \approx 0.5$ kJ/mol, which amounts to only 5 meV per formula unit. In the region $T > T_s$, the value of Q^{-1} obtained for the manganate under study on its heating from liquid helium temperature is greater than the corresponding value obtained on cooling from the paramagnetic region. Hence, when the sample is heated starting from $T < T_s$, it contains additional scattering centers for the sound waves at temperatures up to T = 350 K. This conclusion agrees well with the assumption that, at $T > T_s$, inclusions of the *Pnma* phase are present in the $R\bar{3}c$ matrix if the sample is heated starting from the temperature region $T < T_s$. When the sample is cooled starting from 350 K, the inclusions of the *Pnma* phase are presumably absent in the rhombohedral matrix down to the vicinity of T_s. Using the data presented in Fig. 2, we can estimate the relative volume x of the orthorhombic phase in the rhombohedral matrix at $T > T_s$. Assuming that $V_l = V_l^{\text{rhom}}(1 - x) + V_l^{\text{orto}} x$ and the velocity difference between the phases, $V_l^{\text{rhom}} - V_l^{\text{orto}} = 260$ m/s, does not depend on T, we obtain that, in the temperature interval 120–320 K, the fraction of the orthorhombic phase is about 6%. Such an inhomogeneity is difficult to detect by magnetic measurements, because the magnetizations of the *Pnma* and $R\bar{3}c$ phases are fairly close to each other.

Thus, in the temperature dependences of the longitudinal sound velocity and the internal friction in a $La_{0.8}Sr_{0.2}MnO_3$ single crystal, we observed a thermal hysteresis of giant width. When the single crystal is heated starting from temperatures below the point of the *Pnma* $\longrightarrow$ $R\bar{3}c$ transition, some regions occupied by the *Pnma* orthorhombic phase are presumably retained inside the $R\bar{3}c$ rhombohedral matrix up to the temperature T = 350 K, whereas, when the crystal is cooled down from 350 K, orthorhombic inclusions in the rhombohedral matrix are absent down to the close vicinity of T_s.

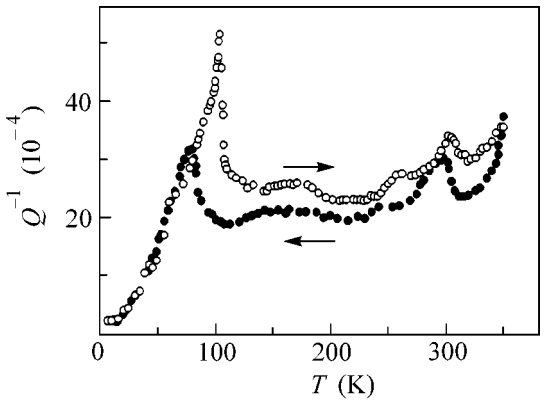

Fig. 3. Temperature dependence of the internal friction Q^{-1} obtained in the cooling and heating runs.

This work was supported by the Russian Foundation for Basic Research, project nos. 00-02-17544 and 00-15-96745.

REFERENCES

1. É. L. Nagaev, Usp. Fiz. Nauk **166**, 833 (1996) [Phys. Usp. **39**, 781 (1996)].
2. A. P. Ramirez, J. Phys.: Condens. Matter **9**, 8171 (1997).
3. Y. Tokura and Y. Tomioka, J. Magn. Magn. Mater. **200**, 1 (1999).
4. J. M. D. Coey, M. Viret, and S. von Molnar, Adv. Phys. **48**, 167 (1999).
5. A. M. Kadomtseva, Yu. F. Popov, G. P. Vorob'ev, *et al.*, Fiz. Tverd. Tela (St. Petersburg) **42**, 1077 (2000) [Phys. Solid State **42**, 1110 (2000)].
6. A. Asamitsu, Y. Moritomo, R. Kumai, *et al.*, Phys. Rev. B **54**, 1716 (1996).
7. V. E. Arkhipov, N. G. Bebenin, V. P. Dyakina, *et al.*, Phys. Rev. B **61**, 11229 (2000).
8. A. Moreo, S. Yunoki, and E. Dagotto, Science **283**, 2034 (1999).
9. N. N. Loshkareva, Yu. P. Sukhorukov, É. A. Neĭfel'd, *et al.*, Zh. Éksp. Teor. Fiz. **117**, 440 (2000) [JETP **90**, 389 (2000)].
10. M. Hervieu, G. van Tendeloo, V. Caignaert, *et al.*, Phys. Rev. B **53**, 14274 (1996).
11. D. Shulyatev, S. Karabashev, A. Arsenov, and Ya. Makovskii, J. Cryst. Growth **198/199**, 511 (1999).
12. H. J. McSkimin, in *Physical Acoustic. Principles and Methods*, Ed. by W. P. Mason (Academic, New York, 1964; Mir, Moscow, 1966), Vol. I, Part A, p. 272.
13. A. M. Burkhanov, V. V. Gudkov, I. V. Zhevstovskikh, *et al.*, Fiz. Met. Metalloved., No. 1, 68 (1990).
14. A. Urushibara, Y. Moritomo, T. Arima, *et al.*, Phys. Rev. B **51**, 14103 (1995).
15. R. I. Zaĭnullina, N. G. Bebenin, V. V. Mashkautsan, *et al.*, Zh. Éksp. Teor. Fiz. **120**, 139 (2001) [JETP **93**, 121 (2001)].
16. V. E. Arkhipov, N. G. Bebenin, K. M. Demchuk, *et al.*, in *Abstract Book of the EASTMAG-2001, Institute of Metal Physics, Ural Division of the Russian Academy of Science, Yekaterinburg, 2001*, p. 120.

Translated by E. Golyamina

JETP Letters, Vol. 74, No. 2, 2001, pp. 118–121. Translated from Pis'ma v Zhurnal Éksperimental'noĭ i Teoreticheskoĭ Fiziki, Vol. 74, No. 2, 2001, pp. 123–126.

Screening of Exciton States by Quasi-Two-Dimensional Electron Gas in Quantum Wells

D. V. Kulakovskiĭ[1]*, S. I. Gubarev[1], and Yu. E. Lozovik[2]

[1] *Institute of Solid-State Physics, Russian Academy of Sciences, Chernogolovka, Moscow region, 142432 Russia*

[2] *Institute of Spectroscopy, Russian Academy of Sciences, Troitsk, Moscow region, 142092 Russia*

* *e-mail: kulakovd@issp.ac.ru, lozovik@isan.troitsk.ru*

Received June 27, 2001

Changes in the binding energy and oscillator strength of an exciton state due to screening by a quasi-two-dimensional electron gas were calculated self-consistently in a nonlinear approximation. It was shown that the collapse of the bound state proceeds at very small concentrations $N_s \simeq 5 \times 10^9$ cm^{-2}, which is a consequence of taking into account the nonlinearity of the system response to the Coulomb perturbation. © *2001 MAIK "Nauka/Interperiodica".*

PACS numbers: 71.35.Cc; 73.21.Fg

The occurrence of mobile electrons in selectively doped GaAs/AlGaAs-based quantum wells (QW) leads to the screening of the Coulomb interaction in two-dimensional structures and, thus, essentially affects both the stability of impurity and many-particle Coulomb centers and the character of large-scale fluctuations in QWs. In spite of the fact that the electron spectrum in the QWs for which experiments were performed is actually dimensionally quantized and may be considered as purely two-dimensional, these structures are quasi-two-dimensional as applied to the problem of the screening of the Coulomb interaction, because the width of typical QWs (200–300 Å) is several times larger than the exciton Bohr radius. Therefore, the screening of the Coulomb interaction in real QWs is of mixed character, varying from purely two-dimensional at large distances (much larger than the QW width) to virtually three-dimensional at small distances. The screening effect is revealed most directly in experiments on the screening of exciton states upon increasing the quasi-two-dimensional gas density. It was shown experimentally in [1] that the threshold concentration at which the collapse of exciton states took place depended strongly on the structure quality and was observed at extremely small concentrations $N_s = 5 \times 10^9$ cm^{-2} for most perfect structures. This value corresponds to the dimensionless parameter r_s, which describes the average distance between electrons in the gas in units of the Bohr radius a_B, $r_s = 1/a_B\sqrt{2\pi N_s} \approx 8$. This value is several times higher than the values observed previously in experiments with structures of lower quality [2], where the collapse of exciton states was observed at higher (by an order of magnitude) electron gas concentration. The screening of the Coulomb interaction by a two-dimensional electron gas was considered theoretically by Bauer [3] within the framework of the theory of dielectric screening and by Kleinman [4] in the approximation of linear dielectric response for a purely two-dimensional electron gas. However, both these approaches give considerably higher threshold concentrations than those observed in perfect GaAs/AlGaAs structures.

In this work, we developed a method for self-consistent calculations of the screening of the Coulomb interaction by a two-dimensional electron gas. This method took into account to some extent the nonlinearity of screening, as a result of which the threshold values of concentration were shifted from $r_s \sim 3$ to the region of values $r_s \sim 8$, which is in qualitative agreement with the results of recent experiments.

In the subsequent discussion, our interest will be with the binding energy of an exciton state in the presence of a quasi-two-dimensional electron gas with the concentration N_s. It is known that the problem of determining the binding energy of a large-radius exciton is reduced to the problem of a Coulomb center with the particle mass equal to the reduced exciton mass $\mu = m_e m_h/(m_e + m_h)$, where m_e and m_h are the planar masses of an electron and a hole, respectively, in the quantum well.

Consider a quantum well of width l_0 with infinitely high walls such that the wave function of electrons in the z direction is strictly restricted by the QW sizes. As a model of an exciton, consider a positively charged Coulomb center located at the middle of the QW at $z = 0$ and an electron bound with this center with the mass equal to the reduced exciton mass μ. The Hamil-

tonian of such a center in cylindrical coordinates takes the following form:

$$\hat{H} = -\frac{\hbar^2}{2\mu}\Delta + U(\rho, z), \tag{1}$$

where

$$U(\rho, z) = -\frac{e^2}{\epsilon\rho} + F(z). \tag{2}$$

Here, $\rho = \sqrt{r^2 + z^2}$, $F(z) = 0$ at $z \le |l_0/2|$, and $F(z) = \infty$ at $z > |l_0/2|$.

The ground state energy will be sought by the Ritz variational method with the trial wave function of the bound state in the form

$$\Psi(r, z) = N\cos\left(\frac{\pi z}{l_0}\right)\exp\left(-\frac{\sqrt{r^2 + \gamma^2 z^2}}{r_0}\right). \tag{3}$$

There are two variable parameters in this function: the effective radius r_0 of the Coulomb center (exciton) in the (x, y) plane and the parameter γ taking into account the anisotropy due to the finiteness of motion in the z direction. This wave function correctly describes the behavior of the system in both narrow QWs when $l_0 \ll r_0$ (in this case, $\gamma \longrightarrow 0$, and the function coincides with the purely two-dimensional one) and wide QWs when $l_0 \ge r_0$. In the case of wide QWs, $\gamma \sim 1$, and the function is spherically symmetric as in three-dimensional systems.

For variational calculations, it is convenient to introduce an effective two-dimensional potential $U_{\text{eff}}(r)$ that can be written in the adiabatic approximation in the following form:

$$U_{\text{eff}}(r) = \int |\Psi(r, z)|^2 U(r, z)dz. \tag{4}$$

The Fourier transform of this potential will take the form

$$\begin{aligned} U_{\text{eff}}(q) &= \iint e^{i\mathbf{qr}} U_{\text{eff}}(r)d\mathbf{r} \\ &= 2\pi\int J_0(qr)U_{\text{eff}}(r)rdr, \end{aligned} \tag{5}$$

where $J_0(x)$ is a Bessel function of the first kind.

The ground state energy of a quasi-two-dimensional exciton is found from the minimum of the functional F,

$$F = \langle\Psi(r, z)| - \frac{\hbar^2}{2\mu}\Delta|\Psi(r, z)\rangle + \langle|U_{\text{eff}}(r)|\rangle, \tag{6}$$

with respect to parameters r_0 and γ.

The screening of the effective potential $U_{\text{eff}}(r)$ by a quasi-two-dimensional electron gas will be taken into account through the dielectric function $\epsilon(q)$,

$$U_{\text{eff}}^{\text{scr}}(r) = \int J_0(qr)(U_{\text{eff}}(q)/\epsilon(q))rdr. \tag{7}$$

Within the random phase approximation, the dielectric function is determined by the susceptibility $\chi(q, \omega)$ of the system,

$$\epsilon^{\text{RPA}}(q, \omega) = 1 - U_{\text{eff}}(q)\chi(q, \omega). \tag{8}$$

In the case of noninteracting electrons, $\chi(q, \omega)$ is the Lindhard polarization operator $\Pi^0(q, \omega)$ [5],

$$\Pi^0(q, \omega) = \frac{1}{L^2}\lim_{\alpha \to 0}\sum\frac{f_0(E_k) - f_0(E_{k+q})}{E_{k+q} - E_k - \hbar\omega - i\hbar\alpha}, \tag{9}$$

where f_0 is the Fermi–Dirac distribution function and L^2 is the area of the system. At $T = 0$ and the Fermi wave vector $k_F = \sqrt{2\pi N_s}$, the static dielectric function may be written as (see, for example, [6])

$$\begin{aligned} \epsilon^{\text{RPA}}(q) &= 1 + U_{\text{eff}}(q) \\ &\times \frac{m_e}{\pi\hbar^2}[1 - \Theta(q - 2k_F)\sqrt{1 - (2k_F/q)^2}], \end{aligned} \tag{10}$$

where $U_{\text{eff}}(q)$ is determined by Eq. (5).

The ground state energy of an exciton in the effective screened potential $U_{\text{eff}}^{\text{scr}}(r)$ obtained by numerically solving the integral equation (7) was calculated by varying the functional in Eq. (6) with respect to parameters r_0 and γ. Because $U_{\text{eff}}^{\text{scr}}(r)$ itself depends on the wave function parameters r_0 and γ, self-consistent values of r_0, γ, and, hence, $U_{\text{eff}}^{\text{scr}}(r)$ were obtained by successive iterations. It should be noted that this procedure of self-consistent calculations goes beyond the limitations of the linear response of the electron subsystem and takes into account to some extent the nonlinear character of the screening of the Coulomb potential by the two-dimensional gas.

The results of a numerical calculation of the binding energy of an exciton are displayed in Fig. 1 as a function of the dimensionless parameter r_s. It is evident that the binding energy of an exciton decreases in a threshold way with increasing concentration of the two-dimensional electron gas (TDEG). For a QW with the width $l_0 = 300$ Å, a sharp decrease (collapse) in the binding energy occurs in the region $r_s \approx 8$. With decreasing well width, the threshold concentration at which the screening of exciton states arises shifts to the region of smaller r_s, that is, larger concentrations (curves in Fig. 1). Assuming for definiteness that the threshold concentration is the concentration at which the binding energy drops by a factor of e, one may construct the dependence of the critical parameter r_s^c on the width of a GaAs/AlGaAs QW (Fig. 2).

The calculated results indicate that the collapse of exciton states arises at significantly lower concentrations of the electron gas, $r_s \approx 8$, than in the previous calculations made by Bauer [3] ($r_s = 1.8$), where the

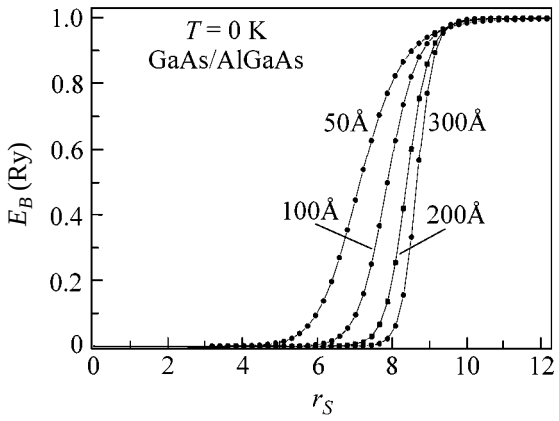

Fig. 1. Dependence of the binding energy of an exciton state E_B in GaAs/AlGaAs QWs with different width in the dimensionless parameter r_s. The planar masses of an electron $m_e = 0.067m_0$ and a hole $m_h = 0.26m_0$ and the static dielectric permittivity $\epsilon = 12.8$ were used in the calculations.

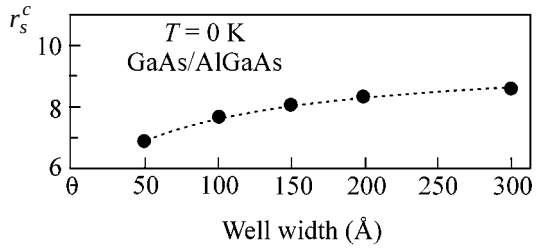

Fig. 2. Dependence of the critical parameter r_s^c at which the collapse of exciton states takes place on the quantum well width.

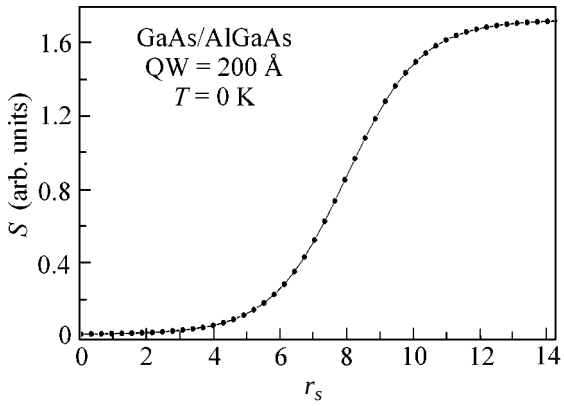

Fig. 3. Variation of the oscillator strength S of an exciton transition on the dimensionless parameter r_s calculated for a GaAs/AlGaAs QW of width 200 Å.

dielectric screening of the Coulomb interaction was considered, or in the work by Kleinman [4] ($r_s = 2.8$), in which the calculations were performed for a purely two-dimensional case within the approximation of linear screening.

Noteworthy are several points that turned out to be very important in this problem. First is taking into account the dependence of the dielectric function on the parameters of the effective interaction $U_{\text{eff}}(r)$, that is, the use of a nonlinear approximation for the system response. If the procedure of self-consistent calculations used in this work is restricted to the linear response approximation, the threshold concentration at which the screening of exciton states is observed shifts to the region of higher concentrations corresponding to $r_s = 3.5$, which is close to the results obtained in [4, 7]. Secondly, the singularity at $q = 2k_F$ in the dielectric function given by Eq. (10) leads, as well as in the three-dimensional case, to oscillations of the TDEG concentration. In contrast to three-dimensional systems, the effect of these oscillations turns out to be significant, because the screened potential exhibits a power-law asymptotic behavior in the two-dimensional case, and the contribution of the oscillation behavior of the local concentration in the vicinity of the Coulomb center turns out to be considerable, leading to a more effective screening of the potential.

As a rule, information on the variation of the binding energy of exciton states as a function of the TDEG density is lacking in experiments on studying the screening of exciton states by the quasi-two-dimensional electron gas, because this information requires knowledge of the energy of the noncorrelated electron and hole, which exhibit no characteristic features in luminescence and absorption spectra. At the same time, a threshold change in the oscillator strength of the exciton transition is clearly observed in optical experiments upon attaining a certain threshold value by the TDEG density. For convenience of comparison with experimental data, we, in addition to the binding energy, also calculated the behavior of the oscillator strength $S \propto |p_{cv}|^2 a_B^{-2} |\Psi(r = 0, z = 0)|^2$ [4] of the exciton transition as a function of the electron gas concentration in the QW (Fig. 3). It is evident that the exciton transition intensity decreases with increasing TDEG density less sharply than the binding energy of the exciton state. This leads to the fact that the exciton absorption line may be observed even at relatively high electron concentrations, when the electron binding energy has already decreased significantly as a result of screening by the quasi-two-dimensional electron gas.

The Lindhard susceptibility approximation, which corresponds to the case of noninteracting electrons in the gas, was used in the given procedure. To a certain degree, the interelectron Coulomb interaction at small distances can be taken into account within the local field approximation [8, 9] by replacing the polarization

operator given by Eq. (9) with a more complicated operator taking into account correlation corrections. This replacement in the procedure of self-consistent calculations proposed in this work leads to a certain displacement of the threshold density towards smaller r_s. It should be noted that the local field approximation is strictly applicable only at $r_s \leq 4$, so that the results obtained within this approximation are of a qualitative character in the region of values $r_s \sim 8$ of our interest.

Thus, the changes in the binding energy and oscillator strength of an exciton state due to screening by a quasi-two-dimensional electron gas in a GaAs/AlGaAs QW of width 50–300 Å have been calculated in this work. It is shown that taking into account the response nonlinearity leads to a stronger screening of the Coulomb interaction as compared to the linear approximation and, as a consequence, shifts the threshold concentration at which the collapse of exciton states occurs towards smaller TDEG densities and, correspondingly, larger r_s ($r_s = 8.3$ for a well 300 Å in width, which significantly exceeds the values calculated within the framework of the dielectric screening theory or within the framework of linear screening by a quasi-two-dimensional electron gas). With decreasing QW width, the threshold electron concentration at which the transition takes place shifts towards the region of smaller parameters r_s. It is also interesting to note that the collapse of exciton states is accompanied by a multiple increase in the effective Bohr radius of the exciton state. In this case, even in wide QWs with $l_0 = 300$ Å at high electron gas densities, the Bohr radius of the exciton is several times larger than the QW width, and the exciton is virtually two-dimensional. On the other hand, the Bohr radius of the exciton at low densities is significantly smaller than the well width, and the exciton wave function in the well only slightly differs from a three-dimensional one. Thus, the screening of an exciton state in wide QWs is additionally accompanied by the 3D $\longrightarrow$ 2D crossover, that is, by the transition of the exciton state from the three-dimensional to the two-dimensional case. This fact may serve as an additional reason explaining the sharpness of the dissociation process of the exciton state observed in the exciton state.

This work was supported by the Russian Foundation for Basic Research and by INTAS, project no. 99-1146.

REFERENCES

1. S. I. Gubarev, I. V. Kukushkin, S. V. Tovstonog, *et al.*, Pis'ma Zh. Éksp. Teor. Fiz. **72**, 469 (2000) [JETP Lett. **72**, 324 (2000)].
2. G. Finkelstein, H. Strikman, and I. Bar-Joseph, Phys. Rev. Lett. **74**, 976 (1995).
3. G. E. W. Bauer, Phys. Rev. B **45**, 9153 (1992).
4. D. A. Kleinman, Phys. Rev. B **32**, 3766 (1985).
5. H. Ehrenreich and M. H. Cohen, Phys. Rev. **115**, 786 (1959).
6. F. Stern, Phys. Rev. Lett. **18**, 546 (1967).
7. E. A. Andryushin and A. L. Silin, Fiz. Tverd. Tela (Leningrad) **21**, 219 (1979) [Sov. Phys. Solid State **21**, 129 (1979)].
8. K. S. Singwi, M. P. Tosi, and R. H. Land, Phys. Rev. **176**, 589 (1968).
9. H. V. da Silvera, M. H. Degani, and K. S. Singwi, Phys. Rev. B **46**, 2995 (1992).

Translated by A. Bagatur'yants

JETP Letters, Vol. 74, No. 2, 2001, pp. 122–127. Translated from Pis'ma v Zhurnal Éksperimental'noĭ i Teoreticheskoĭ Fiziki, Vol. 74, No. 2, 2001, pp. 127–132.

Electronic Structure of the New $MgCNi_3$ Superconductor and Related Intermetallic Compounds

I. R. Shein*, A. L. Ivanovskiĭ, and N. I. Medvedeva

Institute of Solid-State Chemistry, Ural Division, Russian Academy of Sciences, Yekaterinburg, 620219 Russia

** e-mail: irshein@mail.ur.ru*

Received June 13, 2001

The band structure of the new perovskite-like $MgCNi_3$ superconductor is studied by the self-consistent FP-LMTO method. The superconducting properties of $MgCNi_3$ are associated with the occurrence of an intense peak in the density of Ni3*d* states at the Fermi level. The absence of superconductivity for nonstoichiometric $MgC_{1-x}Ni_3$ compositions is caused by the transition of the system to a magnetic state. The possibilities of finding superconductivity for $ScBNi_3$, $InBNi_3$, $MgCCo_3$, and $MgCCu_3$ isostructural with $MgCNi_3$ are discussed.

PACS numbers: 71.20.Lp; 74.70.Dd

The discovery of the superconducting transition ($T_c \approx 39$ K) for the intermetallic MgB_2 compound [1] stimulated a wide search for new superconductors among related systems, which is now performed along three main lines. Within the first line, the class of superconductors based on MgB_2 is extended by its doping or by creating superstructures [2]. The second line covers a wider range of systems: the search for superconducting candidates is performed among binary or multicomponent phases possessing either structural or chemical elements of similarity with MgB_2. As a result, critical transitions were found in ZrB_2 (5.5 K [3]), TaB_2 (9.5 K [4]), Re_3B (4.7 K [5]), and a new beryllium boride phase (0.72 K, composition $BeB_{2.75}$, the unit cell contains 110.5 atoms [6]).

The development of the third line was initiated by observing [7] superconductivity in the ternary intermetallic perovskite-like $MgCNi_3$ compound ($T_c \approx 8$ K). The result obtained in [7] is of special interest due to several circumstances.

1. The high-symmetry $MgCNi_3$ structure (space group $Pm3m$) is a favorable factor for superconductivity. However, all the superconducting perovskites known by now contain oxygen atoms at the positions of type 3*c* (0; 1/2; 1/2), whose electron–hole states have a dominant role in the formation of superconductivity [8]. In the case of $MgCNi_3$, Ni atoms occupy these positions; that is, the nature of the superconductivity mechanism in this compound must be principally different.

2. The majority of the known nonoxide perovskite-like MXM'_3 phases (so-named anti-perovskites, where M = Zn, Al, Ga, In, and Sn; M' = Mn and Fe; and X = C and N) exhibit ferromagnetic, antiferromagnetic, or more complicated (mixed) types of spin ordering [9]. Hence, in the series of its *structural analogues*, $MgCNi_3$ can be considered as a phase boundary between the classes of perovskite-like superconductors (oxides) and magnets (oxygen-free perovskites).

3. Superconducting intermetallic boron carbides (IBC) of general composition LnM_2B_2C are the closest *chemical analogues* of $MgCNi_3$. Nickel-containing $LuNi_2B_2C$ ($T_c \approx 16$ K) and YNi_2B_2C ($T_c \approx 15.6$ K) phases also belong to this family. However, in contrast to $MgCNi_3$, IBC (i) are magnetic superconductors, (ii) possess a quasi-two-dimensional structure composed of (Lu,Y)C layers and NiB_4 tetrahedrons [10], and (iii) contain much less Ni (magnetic metal) than $MgCNi_3$ (35.6–48.9 vs. 82.9 at. %).

The first investigations of some properties of $MgCNi_3$ (critical field H_{c2}, Hall coefficient, and other electrophysical characteristics, [11–14]) allowed $MgCNi_3$ to be assigned to conventional type II superconductors with the electron–phonon interaction type. In this case, the critical temperature can be estimated from the McMillan formula $T_c \approx \langle\omega\rangle \exp\{f(\lambda)\}$, where $\langle\omega\rangle$ is the averaged phonon frequency and λ is the electron–phonon coupling constant $\lambda \sim N(E_F)\langle I^2\rangle$, where $N(E_F)$ is the density of states at the Fermi level. From here, it follows that information on the band structure is of paramount importance in interpreting the superconducting (and some other) properties of $MgCNi_3$ as well as in searching for possible superconducting analogues.

In this communication, we present the results of studying the band structure of the new $MgCNi_3$ superconductor, discuss the effect of the occurrence of C vacancies (carbon nonstoichiometry) on its electronic properties, and analyze the specific features of electronic and magnetic states in the series of related perovskite-like alloys ($ScBNi_3$, $InBNi_3$, $MgBCo_3$, and

Total and orbital densities of states at the Fermi level ($N(E_F)$ and $N_l(E_F)$, 1/eV) for $MgCNi_3$ and related intermetallic compounds

MXM'_3 phase	Total $N(E_F)$	Orbital $N_l(E_F)$							
		M_s	M_p	M_d	X_s	X_p	M'_s	M'_p	M'_d
$MgCNi_3$	4.57	0.00	0.12	0.02	0.01	0.23	0.07	0.09	4.04
$Mg\square Ni_3$	2.38	0.04	0.04	0.04	0.02	0.00	0.02	0.06	2.16
$MgCCo_3$	2.41	0.01	0.01	0.03	0.00	0.01	0.00	0.01	2.33
$MgCCu_3$	0.38	0.04	0.06	0.03	0.00	0.03	0.02	0.04	0.17
$ScBNi_3$	2.59	0.00	0.11	0.20	0.00	0.11	0.05	0.09	2.03
$InBNi_3$	1.47	0.01	0.06	0.01	0.01	0.08	0.02	0.05	1.24

$MgCCu_3$) as possible superconductors. The self-consistent spin-polarized full-potential linear muffin-tin orbital method (FP-LMTO) [15] within the local (spin) density approximation (LDA) was used in calculations with allowance for the relativistic effects according to [16] and with the exchange–correlation potential proposed in [17].

In the $MgCNi_3$ structure, atoms occupy the following positions: 3Ni (0; 1/2; 1/2), Mg (0; 0; 0), and C (1/2; 1/2; 1/2). Their coordination polyhedrons (CPs) are the $[NiC_2Mg_4]$ and $[CNi_6]$ octahedrons for Ni and C and the $[MgNi_{12}]$ cuboctahedron for magnesium. The theoretical equilibrium lattice parameter of $MgCNi_3$ (3.721 Å) was determined in a good agreement with the experiment (3.8066 Å for the $MgC_{0.96}Ni_3$ [18]) by minimizing the total energy.

The results of calculations for $MgCNi_3$ are given in Figs. 1–4 and in the table. The most important feature of the spectrum of $MgCNi_3$ is the occurrence of an intense peak in the density of states (DOS) at E_F associated with the quasi-flat π antibonding Ni3*d* bands (in the X–M and the M–Γ directions of the Brillouin zone)—see Fig. 1. The Fermi level E_F is located at the high-energy slope of this peak. The value of $N(E_F)$ comprises

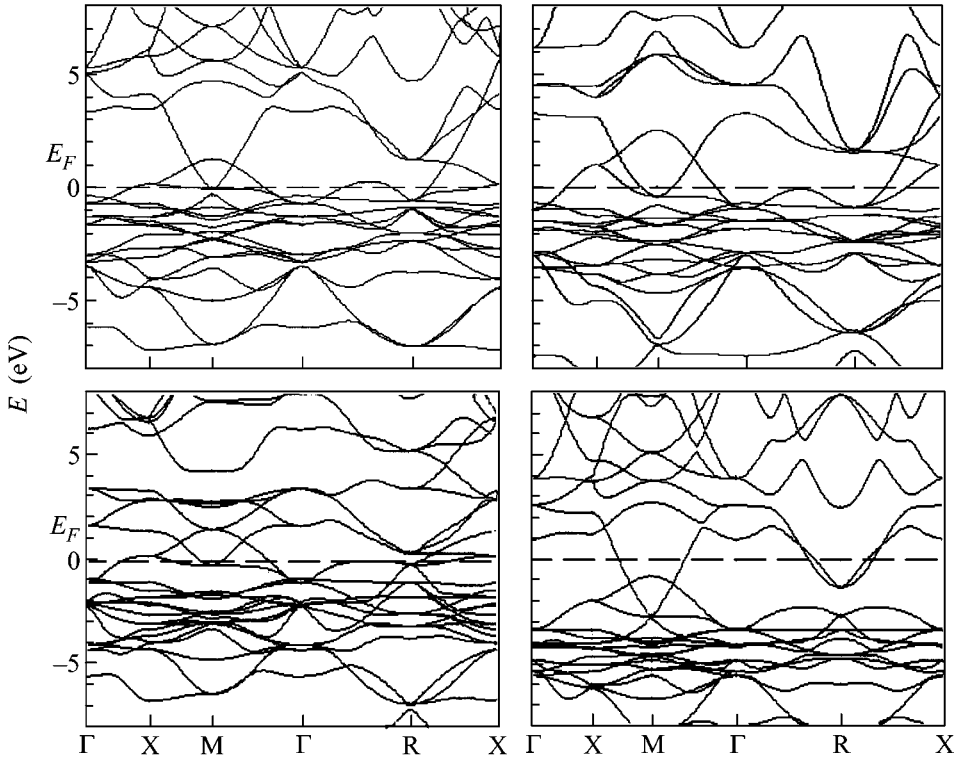

Fig. 1. Energy bands for (*1*) $MgCNi_3$, (*2*) $InBNi_3$, (*3*) $ScBNi_3$, and (*4*) $MgCCu_3$.

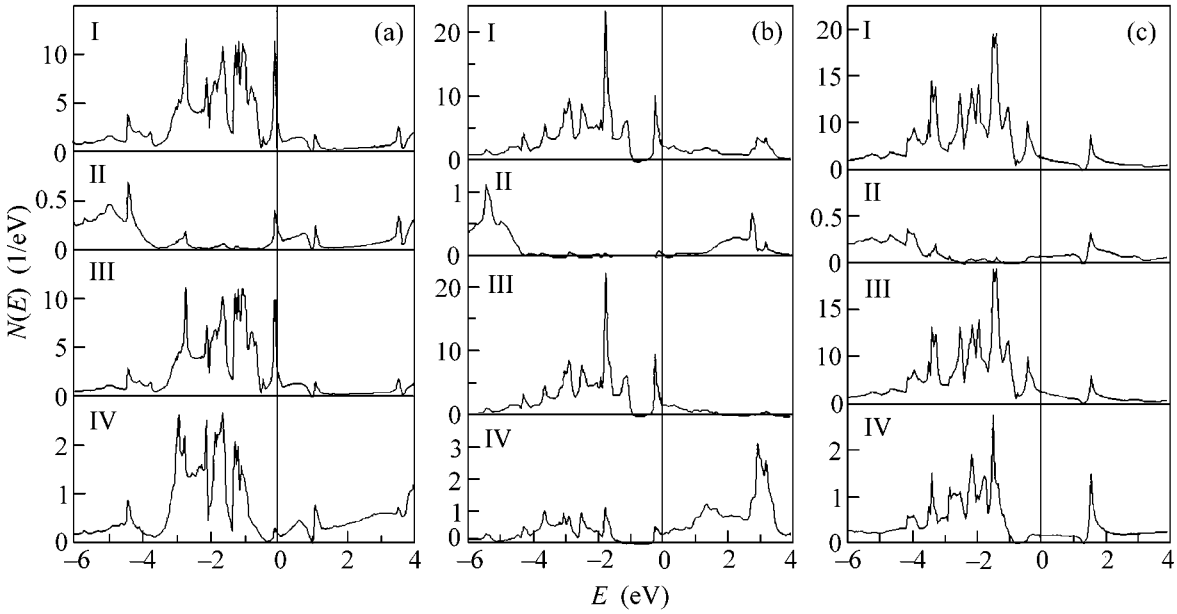

Fig. 2. (I) Total and (II–IV) atomic partial densities of states for (*1*) $MgCNi_3$, (*2*) $ScBNi_3$, and (*3*) $InBNi_3$. The distributions correspond to (II) C and B; (III) Ni; and (IV) Mg, Sc, and In.

4.57 states/eV, which is in good agreement with the result of the full-potential FLAPW calculation [19] 4.99 states/eV. The decomposition of $N(E_F)$ into orbital components ($N_l(E_F)$) indicates (see table) that the largest contribution to $N(E_F)$ (4.04 states/eV or 88.2%) is due to the Ni3*d* states. The contributions to the $N(E_F)$ from the C2*s*, *p* and Mg3*s*, *p*, *d* states equal 0.23 (5.08%) and 0.14 states/eV (3.03%), respectively. The Stoner parameter $S = N(E_F)I_{ex}$ (I_{ex} is the exchange integral) is ≈0.55, and there are no magnetic moments on atoms. The upper of the two antibonding Ni3*d* bands, whose dispersion is more clearly defined, determines the electronic type of the Fermi surface (Fig. 3) in the form of spheroids in the vicinity of the Γ point and small sheets along the Brillouin zone (BZ) boundaries and angles. The flatter Ni3*d* band forms lobe-type singularities at the BZ faces with the center at the point X and cigar-shaped figures along the Γ–R direction.

For comparison of individual bonds, crystal orbital overlap populations (COOP) were calculated within the tight-binding method for $MgCNi_3$ and $ScBNi_3$. The corresponding values for $MgCNi_3$ were found to be 0.298 (Ni–C), 0.027 (Ni–Ni), and 0.039 e/bond (Ni–Mg). Thus, the Ni–C bonds form the basis of interatomic interactions in $MgCNi_3$ (in the $[CNi_6]$ CP, Fig. 4). The C–Mg bonding is negligible (0.002 e/bond). For $ScBNi_3$, these values were 0.338 (Sc–B), 0.050 (Ni–Ni), 0.033 (Ni–Sc), and 0.005 e/bond (B–Sc). These results provide an explanation for the data [13] on studying the temperature dependence of the Debye–Waller factors (DWF) of atoms in $MgCNi_3$. The minimal (isotropic) temperature factor of carbon corresponds to its most strongly bound (and highly symmetric, at the center of the Ni_6 octahedron) state in the crystal, whereas the DWF for Ni is large and anisotropic: in the NiCP ($[NiC_2Mg_4]$ octahedra) the COOPs of different-type (Ni–C and Ni–Mg) bonds differ by an order of magnitude. The minimal mean-square displacements observed for Ni (U_{11}) correspond to the directions of the strongest Ni–C bonds.

Based on the results presented in Fig. 2, it may be expected within the rigid-band model that introducing electron or hole dopants into $MgCNi_3$ will result in a decrease or increase in $N(E_F)$, respectively. In the former case, one may expect that the superconductivity of the system will deteriorate. Doping with holes, being favorable to the growth of $N(E_F)$ and to an increase in T_c, can, however, induce the transition of the system to a magnetic state accompanied by the loss of superconductivity. A similar structure of the spectrum (the occurrence of an intense peak of metallic states at the Fermi level, which points in the general case to the instability of the nonmagnetic state of the system) is accomplished in superconducting IBCs, and this structure determines the formation of atomic magnetic moments (MM) in these systems [4].

We carried out calculations for systems modeling the variants of spectrum modifications indicated above. The effect of a decrease in the occupation of energy bands was considered as the result of the occurrence of vacancies in the C sublattice of $MgCNi_3$ (hypothetical $Mg\square Ni_3$ perovskite with the empty C sublattice was calculated; from here on, □ designates a structural vacancy) or the substitution of Co for Ni ($MgCCo_3$

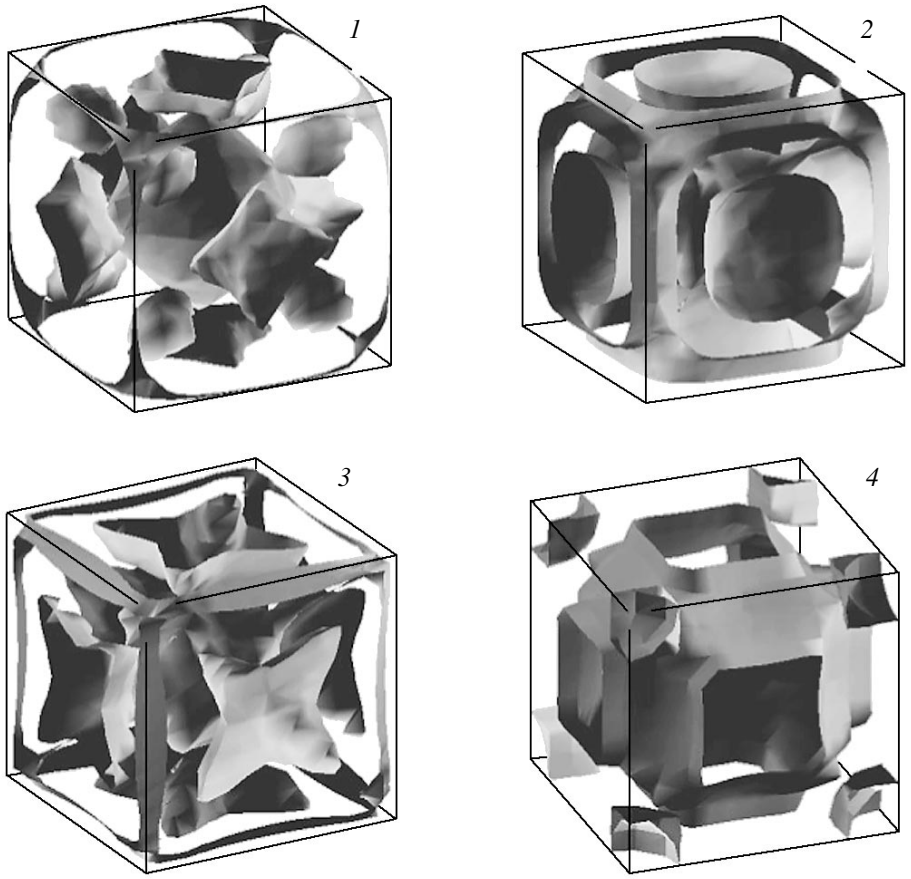

Fig. 3. Fermi surfaces for (*1*) $MgCNi_3$, (*2*) $InBNi_3$, (*3*) $ScBNi_3$, and (*4*) $MgCCu_3$.

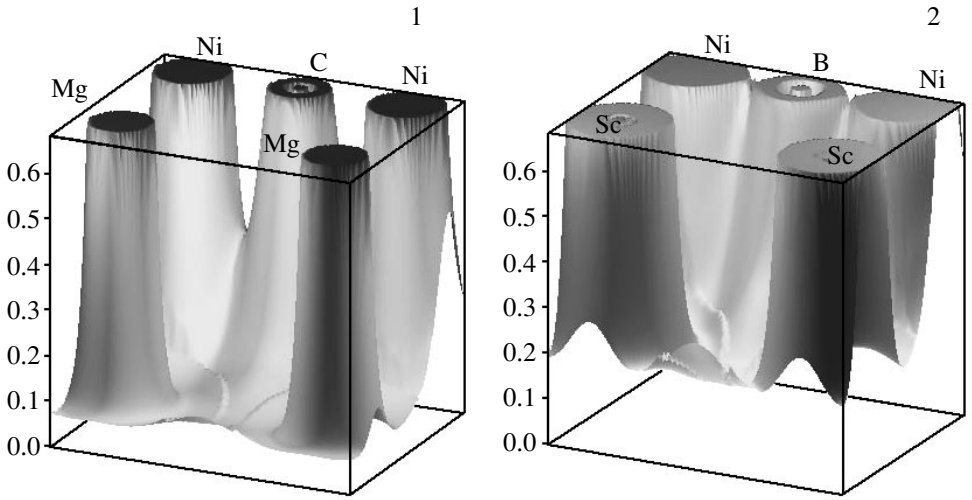

Fig. 4. Charge densities for (*1*) $MgCNi_3$ and (*2*) $ScBNi_3$.

phase). The growth of the electron concentration was modeled using the $MgCCu_3$ phase as an example. In addition, stable boron-containing $ScBNi_3$ and $InBNi_3$ phases with lattice parameters taken according to [20], which are isostructural and isoelectronic with $MgCNi_3$, were considered as possible superconductors.

For the nonstoichiometric anti-perovskite, it was obtained that $Mg\square Ni_3$ occurs in a magnetic state, and the MM of atoms were found to be $0.44\mu_B$ for the Ni atoms and $-0.05\mu_B$ for the Mg atoms. A similar result was also obtained for $In\square Ni_3$: the MM of atoms were $0.20\mu_B$ for the Ni atoms and $-0.01\mu_B$ for In atoms. From here, it follows that the condition of obtaining superconducting $MgCNi_3$ as a phase of strictly stoichiometric composition (at a deficiency of carbon, $MgC_{1-x}Ni_3$ samples ($x > 0.1$) lose superconductivity) noted in the experiments [7] is determined primarily by the peculiarities of its electronic structure.

The ground state of the $MgCCo_3$ anti-perovskite is magnetic: according to calculations, the MM of atoms equal 0.36 for Co and $-0.05\mu_B$ for Mg. For $MgCCu_3$, it was found that (a) an increase in the electron concentration results in the filling of the antibonding bands (Fig. 1), and (b) $N(E_F)$ decreases by more than an order of magnitude as compared with $MgCNi_3$, in the case of which delocalized *sp* states dominate (Fig. 3). The data obtained offer an explanation for the change in the superconducting properties of $MgCNi_3$ upon doping the Ni sublattice with 3*d* transition metals. It is known that the critical transition temperature for $MgCNi_{3-x}M_x$ alloys (M = Mn, Co, and Cu) [13, 14] drops (a) with the growth of the concentration of dopants and (b) with the decrease in their atomic number from Co to Mn. Studying the dependence of T_c on the copper concentration showed that T_c decreases systematically in the range $0 < x < 0.1$. The partial substitution of Co atoms for nickel leads to the disappearance of superconductivity already for $x = 0.03$. The effect of suppressing superconductivity is enhanced for substitutions of Mn for Ni. According to the calculated data, various dopants principally differ in the nature of the effect observed. Spin fluctuations are the reason in the case of alloys with substituted Mn and Co, whereas the growth of the total electron concentration in the system and a sharp decrease in $N(E_F)$ are the reason in the case of Cu.

The calculated results for boron-containing $ScBNi_3$ and $InBNi_3$ anti-perovskites are presented in Figs. 1–4 and in the table. A comparison of chemical bonding in $MgCNi_3$ and $ScBNi_3$ (charge density maps, Fig. 4) reveals that the covalent overlap in the case of Sc–B bonds is stronger than that for Mg–C bonds, which fully coincides with the data that we obtained within the tight-binding model, as shown above.

As one goes from $MgCNi_3$ to $ScBNi_3$ and $InBNi_3$, the Fermi level shifts towards the high-energy region of the Ni3*d* peak, and $N(E_F)$ decreases significantly. In this series of compounds, one of the antibonding bands decreases in reference to the Fermi level along the M–Γ direction and shifts upward in the vicinity of the point X. At the point M, the band shifts upward, and the band drops below the Fermi level in the Γ–R direction. These changes in the band structure result in a modification of the Fermi surface. The spheroidal surfaces of the electronic type in the vicinity of the point Γ undergo only slight changes, and the quasi-cylindrical electronic surface along the BZ boundaries increases in the series of compounds under consideration. The hole-type cigar-shaped figures along the Γ–R direction are absent for $ScBNi_3$ and $InBNi_3$, whereas the lobe-type singularities at the BZ faces with the center at the point X increase for $ScBNi_3$ and degenerate into spheroids for $InBNi_3$. Thus, the topology of the Fermi surface for the given compounds retains the main features of superconducting $MgCNi_3$. The Fermi surface for $MgCCu_3$ is also shown in Fig. 3. A rise in the Fermi level for this compound leads to a qualitatively different topology: surfaces of both electronic and hole types are absent in the vicinity of the Γ and X points.

The double substitution of this kind for the given isoelectronic systems leads to changes in the electronic structure, for which the appearance of superconducting properties can be expected upon hole doping. The most probable method is the introduction of B vacancies (boron nonstoichiometry, all the more that this possibility for $InBNi_3$ is known from the experiment [20]) or the partial replacement of Sc by atoms of group I or II. Doping the Ni sublattice with magnetic impurities (Co, Mn) may be more problematic because of magnetic instability.

Thus, the band structure of the new perovskite-like $MgCNi_3$ superconductor was studied in this work. The superconducting properties of the intermetallic compound are due to the occurrence of an intense peak in the density of Ni3*d* states at the Fermi level. The deterioration of the superconducting characteristics of $MgCNi_3$ upon hole doping of the (nonstoichiometric in carbon) $MgC_{1-x}Ni_3$ compositions or upon doping the nickel sublattice with Co or Mn is determined by the transition of the system to a magnetic state. The deterioration of superconductivity upon electron doping ($MgCNi_{3-x}Cu_x$ alloys) is due to the filling of antibonding states and a sharp drop in $N(E_F)$. The probability of discovering superconductivity in the stoichiometric $ScBNi_3$ and $InBNi_3$ anti-perovskites is indicated.

REFERENCES

1. J. Nagamatsu, N. Nakagawa, T. Muranaka, *et al.*, Nature **410**, 63 (2001).
2. N. I. Medvedeva, Yu. E. Medvedeva, A. L. Ivanovskiĭ, *et al.*, Pis'ma Zh. Éksp. Teor. Fiz. **73**, 378 (2001) [JETP Lett. **73**, 336 (2001)].
3. V. A. Gasparov, N. S. Sidorov, I. I. Zver'kova, *et al.*, JETP Lett. **73**, 532 (2001).

4. D. Kaczorowski, J. Klamut, and A. Zaleski, cond-mat/0104479 (2001).
5. G. K. Strukova, V. F. Degtyareva, D. V. Shivkun, *et al.*, cond-mat/0105293 (2001).
6. D. Young, P. Adams, J. Chan, *et al.*, cond-mat/0104063 (2001).
7. T. He, Q. Huang, A. P. Ramirez, *et al.*, cond-mat/0103296 (2001).
8. A. Taraphder, R. Pandit, H. R. Krishnamurthy, and T. V. Ramakrishnan, Int. J. Mod. Phys. B **10**, 863 (1996).
9. A. L. Ivanovskiĭ, Usp. Khim. **64**, 499 (1995).
10. A. L. Ivanovskiĭ, Usp. Khim. **67**, 493 (1998).
11. S. Y. Li, R. Fan, X. H. Chen, *et al.*, cond-mat/0104554 (2001).
12. Z. Q. Mao, M. M. Rosario, R. Nelson, *et al.*, cond-mat/0105280 (2001).
13. M. A. Hayward, M. K. Haas, T. He, *et al.*, cond-mat/0104541 (2001).
14. Z. A. Ren, G. C. Che, S. L. Jia, *et al.*, cond-mat/0105366 (2001).
15. M. Methfessel and M. Scheffler, Physica B (Amsterdam) **172**, 175 (1991).
16. S. Y. Savrasov, Phys. Rev. B **54**, 16470 (1996).
17. S. H. Vosko, L. Wilk, and M. Nusair, Can. J. Phys. **58**, 1200 (1980).
18. Q. Huang, T. He, K. A. Regan, *et al.*, cond-mat/0105240 (2001).
19. J. D. Singh and I. I. Mazin, cond-mat/0105577 (2001).
20. Yu. B. Kuz'ma, *Crystal Chemistry of Borides* (Vishcha Shkola, Lvov, 1983).

Translated by A. Bagatur'yants

JETP Letters, Vol. 74, No. 2, 2001, pp. 65–71. Translated from Pis'ma v Zhurnal Éksperimental'noĭ i Teoreticheskoĭ Fiziki, Vol. 74, No. 2, 2001, pp. 69–75.

An Inclusive Approach to Scanning $e^+e^- \longrightarrow \pi^+\pi^-$ Cross Section below 1 GeV by the Radiative-Return Method

N. P. Merenkov* and O. N. Shekhovtsova

Kharkov Institute of Physics and Technology, National Science Center, ul. Akademicheskaya 1, Kharkov, 61108 Ukraine

** e-mail: merenkov@kipt.kharkov.ua*

Received June 6, 2001; in final form, June 28, 2001

An inclusive approach to measuring $e^+e^- \longrightarrow \pi^+\pi^-$ cross section by the radiative-return method is discussed. This approach is substantially based on the choice of selection rules that exclude three-pion events and reduce the radiation background in the final state. Radiative corrections in the process with emission in the initial state are calculated for the DAPHNE conditions by treating the cross section form and the kinematics of the radiative process in the quasi-real electron approximation. © *2001 MAIK "Nauka/Interperiodica".*

PACS numbers: 13.10.+q; 13.40.-f; 12.20.Ds

1. Recent measurement [1] of the muon anomalous magnetic moment $(g-2)_\mu$ cast some doubt upon correctness of the SM. V. Hughes, spokesman for the experiment [2], said, "There are three possibilities of interpreting this result. First, the manifestation of new physics beyond the SM such as supersymmetry. Second, there is a low statistical probability that the experimental and theoretical values are consistent. Third, the history of science has taught us that low-probability errors in both experiments and theories are always possible."

Before the ultimate conclusion about SM violation is drawn, the second possibility should be very thoroughly analyzed. The dominant uncertainty in the theoretical $(g-2)_\mu$ value comes from the hadronic vacuum polarization whose contribution is related to the total hadronic cross section for electron–positron annihilation by the dispersion integral [3]. For high energies, this cross section can be analytically calculated by the QCD rules, which, however, cannot be applied to energies below several gigaelectronvolts. For this reason, precision data on the hadronic cross section for low and intermediate energies are of great importance.

Recent data obtained in Novosibirsk [4] and Beijing [5] have not yet been included in any analysis, but new experiments with a percent accuracy should undoubtedly be carried out.

In this work, we discuss the possibility of scanning the total hadronic cross section by the radiative-return method [6] with the inclusive selection of events (ISE). The ISE implies precision measurement of the invariant hadron mass, which makes the detection of a photon emitted in the initial state unnecessary [7]. Of course, some extra conditions should be imposed on the selection of events in this case (see below). This approach, which requires that the final hadronic state be known, can be realized at DAPHNE, where the $\pi^+\pi^-$ channel dominates because of radiative return to the ρ resonance and the momenta of charged pions can be measured with high accuracy by a drift chamber. In addition, the expected luminosity of the DAPHNE accelerator is high enough to ensure necessary high statistics of the corresponding radiative events.

The ISE cross section in the Born approximation coincides with the cross section for events with identified photons (if a photon falls into a narrow photon detector placed in the electron-beam direction), but the radiative corrections (RCs) are different in these cases because the emission of two hard photons is possible. This case is reminiscent of the RCs in deep inelastic scattering for leptonic (an analogue is events with identified photons) and hadronic (an analogue is ISE) variables. In the latter case, the RCs are factorized, whereas, in the former one, they necessarily include some integrals with the hadronic cross section, which should be extracted from the experimental data. This circumstance makes the ISE approach more attractive.

2. Let us consider the above-mentioned extra event-selection conditions that are appropriate for DAPHNE and must primarily ensure selecting only the $\pi^+\pi^- + n\gamma$ final states. Moreover, these conditions must reduce the background caused by the emission in the final state and simplify the RC calculation. First, to exclude the $\pi^+\pi^-\pi^o$ states, one should select only events in which the difference between the lost energy and lost momentum is small in absolute value. This condition has the form

$$2E - E_+ - E_- - \left|\mathbf{P}_\Phi - \mathbf{p}_+ - \mathbf{p}_-\right| < \eta E, \quad \eta \ll 1, \qquad (1)$$

where E is the beam energy; $E_\pm$ and $\mathbf{p}_\pm$ are, respectively, the energy and momentum of $\pi^\pm$; and $\mathbf{P}_\Phi$ is the initial total momentum, which appears because the laboratory

coordinate system at DAPHNE does not coincide with the center-of-mass system, $|\mathbf{P}_\Phi| = 12.5$ MeV. It is convenient to represent Eq. (1) in terms of the total energy Ω and absolute value $|\mathbf{K}|$ of the total momentum of all photons in the $e^+ + e^- \longrightarrow \pi^+ + \pi^- + n\gamma$ reaction:

$$\Omega - |\mathbf{K}| < \eta E. \tag{2}$$

The optimal value $\eta = 0.02$ also considerably reduces the background caused by emission in the final state [8].

The second condition must select only events for which an undetected photon is collinear at $n = 1$:

$$\mathbf{K}\mathbf{p_1} > |\mathbf{K}| E c_0, \quad c_0 = \cos\theta_0, \tag{3}$$

where $\mathbf{p_1}$ is the electron momentum and θ_0 is taken to be 5°–6°. This restriction considerably increases the contribution to the cross section from the emission in the initial state by a factor of $\ln(E^2\theta_0^2/m^2)$, where m is the electron mass, and provides the possibility of applying the very useful method of quasi-real electrons [9] to the calculation of the RCs to the Born cross section.

In the Born approximation, which corresponds to $n = 1$, Eq. (2) is always satisfied. Therefore, nontrivial restrictions caused by Eqs. (2) and (3) arise only at the RC level when the contribution from the emission of two hard photons ($n = 2$) is calculated.

3. Let us consider the case where the angular phase space of pions is unrestricted. In this case, the Born cross section can be written as

$$d\sigma^B = \sigma(q^2)\frac{\alpha}{4\pi^2}L^\gamma_{\mu\nu}(p_1, p_2, k)\tilde{g}_{\mu\nu}\frac{d^3k}{s\omega},$$
$$\sigma(q^2) = \frac{\pi\alpha^2|F_\pi(q^2)|^2}{3q^2}\left(1 - \frac{4m_\pi^2}{q^2}\right)^{3/2}, \tag{4}$$

where k and ω are, respectively, the 4-momentum and energy of a photon; q^2 is the squared invariant mass of pions; m_π is the pion mass; $F_\pi(q^2)$ is the pion electromagnetic form factor; and p_1 and p_2 are the 4-momenta of an electron and positron, respectively. For collinear events that are selected by Eq. (3), the leptonic tensor can be represented as

$$L^\gamma_{\mu\nu}(p_1, p_2, k) = \left[\frac{(q^2 - t_1)^2 + (q^2 - t_2)^2}{t_1 t_2} - \frac{2m^2q^2}{t_1^2}\right]\tilde{g}_{\mu\nu}$$
$$+ \frac{4q^2}{t_1 t_2}\tilde{p}_{1\mu}\tilde{p}_{1\nu} + \left(\frac{4q^2}{t_1 t_2} - \frac{8m^2}{t_1^2}\right)\tilde{p}_{2\mu}\tilde{p}_{2\nu},$$

where

$$\tilde{g}_{\mu\nu} = g_{\mu\nu} - \frac{q_\mu q_\nu}{q^2}, \quad \tilde{p}_{1,2\mu} = p_{1,2\mu} - \frac{p_{1,2}q}{q^2}q_\mu,$$
$$t_1 = -2kp_1, \quad t_2 = -2kp_2,$$
$$s = 2p_1p_2, \quad q^2 = s + t_1 + t_2$$

and terms on the order of m^2/t_2 are omitted.

The contraction of tensors on the right-hand side of Eq. (4) is

$$L^\gamma_{\mu\nu}(p_1, p_2, k)\tilde{g}_{\mu\nu}$$
$$= 2\left[\frac{(q^2 - t_2)^2 + (q^2 - t_1)^2}{t_1 t_2} - \frac{2q^2m^2}{t_1^2}\right]. \tag{5}$$

According to the collinearity condition (3), it is convenient to work in the coordinate system where the Z and X axes are directed along $\mathbf{p_1}$ and $\mathbf{P}_\Phi$, respectively. In this system, we have

$$p_1 = (E, 0, 0, |\mathbf{p_1}|), \quad p_2 = (E, |\mathbf{P}_\Phi|, 0, -p_{2z}),$$
$$p_{2z} = E\left(1 - \frac{\mathbf{P}_\Phi^2}{2E^2}\right) \tag{6}$$

and

$$t_1 = -2\omega(E - |\mathbf{p_1}|\cos\theta),$$
$$t_2 = -2\omega E\left[1 + \left(1 - \frac{\mathbf{P}_\Phi^2}{2E^2}\right)\cos\theta\right] + 2\omega|\mathbf{P}_\Phi|\sin\theta\cos\phi, \tag{7}$$
$$s = 4E^2 - \mathbf{P}_\Phi^2,$$
$$q^2 = 4E^2 - 4E\omega - \mathbf{P}_\Phi^2\left(1 - \frac{\omega}{E}\cos\theta\right) + 2\omega|\mathbf{P}_\Phi|\sin\theta\cos\phi,$$

where θ and ϕ are, respectively, the polar and the azimuthal emission angles of a photon emitted in the initial state.

Integration with respect to the angles on the right-hand side of Eq. (4) can be preformed by using the formulas

$$\int\frac{d\phi d\cos\theta}{-t_2} = \frac{\pi\theta_0^2}{4\omega_0 E},$$
$$\int\frac{d\phi d\cos\theta}{-t_1} = \frac{\pi}{\omega_0 E}\left[\left(1 - \frac{\mathbf{P}_\Phi^2}{4E^2}\right)L_0 - \frac{\theta_0^2}{12}\right],$$

$$\int\frac{d\phi d\cos\theta m^2}{t_1^2} = \frac{\pi}{\omega_0^2}\left(1-\frac{\mathbf{P}_\Phi^2}{2E^2}\right),$$
$$\int\frac{d\phi d\cos\theta t_2}{t_1} = 4\pi\left[\left(1-\frac{\mathbf{P}_\Phi^2}{4E^2}\right)L_0-\frac{\theta_0^2}{3}\right], \quad (8)$$
$$\int\frac{d\phi d\cos\theta}{t_1 t_2} = \frac{\pi}{4\omega_0^2E^2}\left[\left(1-\frac{\mathbf{P}_\Phi^2}{4E^2}\right)L_0+\frac{\theta_0^2}{6}\right],$$
$$\omega_0 = \frac{4E^2-q^2-\mathbf{P}_\Phi^2}{4E}, \quad L_0 = \ln\frac{E^2\theta_0^2}{m^2}.$$

For integration, one can set

$$|\mathbf{P}_\Phi|\sin\theta\cos\phi = 0, \quad \mathbf{P}_\Phi^2\cos\theta = \mathbf{P}_\Phi^2,$$

which corresponds to the omission of very small terms on the order of $\mathbf{P}_\Phi^2\theta_2^2/E^2$. With the same accuracy, one can use the relationship

$$\omega d\omega = \frac{\omega_0 dq^2}{4E}\left(1+\frac{\mathbf{P}_\Phi^2}{2E^2}\right), \quad (9)$$

which makes it possible to represent the Born cross section for the process ($n = 1$) in the form

$$\frac{d\sigma^B}{dq^2} = \frac{\sigma(q^2)}{s}\frac{\alpha}{2\pi}\left[\left(\frac{q^4}{8\omega_0E^3}+\frac{q^2}{2E^2}+\frac{\omega_0}{E}\right)\left(1+\frac{\mathbf{P}_\Phi^2}{4E^2}\right)L_0\right.$$
$$\left.-\frac{q^2}{2\omega_0E}+\frac{\theta_0^2}{6}\left(\frac{q^4}{8\omega_0E^3}+\frac{q^2}{2E^2}-\frac{2\omega_0}{E}\right)\right]. \quad (10)$$

In the limiting case $\mathbf{P}_\Phi \longrightarrow 0$, $\theta_0 \longrightarrow 0$, this formula transforms into the well-known result corresponding to the quasi-real electron approximation [9]:

$$\frac{d\sigma^B}{dq^2} = \frac{\sigma(q^2)}{s}\frac{\alpha}{2\pi}P(z, L_0),$$
$$P(z, L_0) = \frac{1+z^2}{1-z}L_0-\frac{2z}{1-z}, \quad z = \frac{q^2}{4E^2}, \quad s = 4E^2.$$

The parameter $|\mathbf{P}_\Phi|$ enters into the cross section through the ratio $|\mathbf{P}_\Phi^2/4E^2|$ (see also the definitions of s and ω_0), which is approximately equal to 1.5×10^{-4} and $\theta_0^2 \approx 10^{-2}$. Therefore, the respective contributions can be ignored in the calculation of the RCs to cross section (10).

4. In the general case, the photon RCs include the contributions from the emission of hard and soft real and virtual photons. The contribution from the virtual- and soft-photon corrections to the ISE cross section has the form

$$\frac{d\sigma^{S+V}}{dq^2} = \frac{\sigma(q^2)}{s}\left(\frac{\alpha}{2\pi}\right)^2$$
$$\times[\rho P(z, L_0) + D(L_s, L_0, z) + K(z)], \quad (11)$$

where the first two terms in square brackets include all logarithmically enhanced contributions (see the first reference in [6]), whereas the third term determines the nonlogarithmic contribution:

$$\rho = 4(L_s-1)\ln\Delta + 3(L_s+\ln z) + \frac{2\pi^2}{3}-\frac{9}{2}, \; L_s = \ln\frac{4E^2}{m^2},$$
$$D(L_s, L_0, z) = \frac{1+z^2}{1-z}L_0\left[(L_0-2L_s-\ln z)\ln z\right.$$
$$\left.+\frac{\pi^2}{3}-2Li_2(z)\right]+\frac{1+2z-z^2}{2(1-z)}L_0+\frac{4z\ln z}{1-z}L_s, \quad (12)$$
$$K(z) = -\frac{1}{1-z}-\frac{8z\ln z}{1-z}+2z\left[\ln^2(1-z)+\frac{\ln^2 z}{1-z}\right]$$
$$+\frac{\pi^2}{6}\left(4z+6-\frac{5}{1-z}\right)+\left(4z-6+\frac{5}{1-z}\right)Li_2(z),$$

where ΔE ($\Delta \ll 1$) is the maximal energy of the soft photon.

It is convenient to divide the contribution from the emission of an extra hard photon to the ISE cross section into three parts. The first part corresponds to events in which the extra photon of energy ω_2 is emitted in the positron-beam direction. This part is calculated by introducing an auxiliary angular parameter $\theta_0' \ll 1$ and applying the quasi-real electron approximation to describe the emission of both photons (one with energy ω_1 along the electron-beam direction and the second along the positron-beam direction). The result is

$$\frac{d\sigma_1^H}{dq^2} = \frac{\sigma(q^2)}{s}\int_{y_0}^{1-\Delta}\left(\frac{\alpha}{2\pi}\right)^2 P(x, L_0)P(y, L_0')\frac{dy}{y},$$
$$L_0' = \ln\frac{E^2\theta_0'^2}{m^2}, \quad x = 1-\frac{\omega_1}{E}, \quad y = 1-\frac{\omega_2}{E}, \quad (13)$$

where $q^2 = sxy$ is taken to be fixed. The maximal energy ω_2 can be obtained from Eq. (2) by taking into account

that the kinematics for these events in the quasi-real electron approximation gives

$$\Omega = \omega_1 + \omega_2, \quad |\mathbf{K}| = \omega_1 - \omega_2, \quad \longrightarrow \quad \omega_2 < \frac{\eta E}{2}, \qquad y_0 = 1 - \frac{\eta}{2}. \tag{14}$$

Because $\eta \ll 1$, the terms proportional to η in the expression for the RCs can be neglected. This enables one to replace x by z (because $q^2 = sz = sxy$) and perform the elementary integration with respect to y on the right-hand side of Eq. (13):

$$\frac{d\sigma_1^H}{dq^2} = \frac{\sigma(q^2)}{s}\left(\frac{\alpha}{2\pi}\right)^2 P(z, L_0) 2(L_0' - 1)\ln\frac{\eta}{2\Delta}. \tag{15}$$

The second part is caused by the emission of two hard collinear photons (each having energy above ΔE) by an electron when both photons are emitted within a narrow cone with angle $2\theta_0$ in the electron-beam direction. With the same accuracy as the contribution from the virtual- and soft-photon corrections, the result can be written as

$$\frac{d\sigma_2^H}{dq^2} = \frac{\sigma(q^2)}{s}\left(\frac{\alpha}{2\pi}\right)^2 \times [A(z, \Delta)L_0^2 + B(z, \Delta)L_0 + C(z, \Delta)]. \tag{16}$$

Here [10],

$$A(z, \Delta) = \frac{1}{2}P_{2\theta}(z) + \frac{1+z^2}{1-z}\left(\ln z - \frac{3}{2} - 2\ln\Delta\right),$$

$$B(z, \Delta) = 3(1-z) + \frac{(3+z^2)\ln^2 z}{2(1-z)} - \frac{2(1+z)^2}{1-z}\ln\frac{1-z}{\Delta},$$

where $P_{2\theta}(z)$ is the θ term of the second-order electron structure function [11] and

$$C(z, \Delta) = \frac{4z}{1-z}\ln\frac{1-z}{\Delta} - \frac{4z}{3(1-z)} - \frac{\pi^2}{6}\frac{4z}{3} + \left(-\frac{17}{3} + \frac{28}{3(1-z)} - \frac{8}{3(1-z)^2}\right)\ln z + \frac{3 - 24z + 54z^2 - 48z^3 + 7z^4}{6(1-z)^3}\ln^2 z + \left(1 - \frac{7z}{3}\right)Li_2(1-z) + J, \tag{17}$$

$$J = \int_0^{1-z}\left[\frac{z^2 + (1-x)^4}{x(1-x-z)(1-x)^2}\int_0^1 \frac{dt}{t}L(t, x, z) + \frac{z+x}{2(1-x)}L_1(x, z) + \frac{x(1-x-z) - 3z}{2(1-x)^2}L_2(x, z)\right]dx,$$

where the logarithmic functions L, L_1, and L_2 have the form

$$L(t, x, z) = \ln\frac{(1-x)\sqrt{F(t, x, z)} + tx[z - x(1-x-z)] + (1-x-z)(1-x)^2}{2\left(1 + \frac{(1-x-z)t}{zx}\right)(1-x-z)(1-x)^2},$$

$$L_1(x, z) = \ln\frac{(x+z)\sqrt{F(1, x, z)} + (1-x-z)[z - x(1-x-z)] + x(x+z)^2}{2z(1-x-z)},$$

$$L_2(x, z) = \ln\frac{(1-x)\sqrt{F(1, x, z)} + x[z - x(1-x-z)] + (1-x-z)(1-x)^2}{2(1-x-z)(1-x)^2},$$

$$F(t, x, z) = (1-x-z)^2(1-x)^2 + 2tx(1-x-z)[z - x(1-x-z)] + t^2x^2(x+z)^2.$$

The integral with respect to the variable x on the right-hand side of Eq. (17) diverges if $x \longrightarrow 0$ and $x \longrightarrow 1 - z$. However, the structure of the integral is such that these divergences cancel each other, which can be seen by taking into account that

(i) the integral with respect to t converges,

(ii) $$\lim_{x\to 0}\frac{z^2 + (1-x)^4}{x(1-x-z)(1-x)^2}L(t, x, z) = -\frac{1+z^2}{x(1-z)}\ln\frac{t(1-z)}{xz},$$

$$\lim_{x\to 1-z}\frac{z^2 + (1-x)^4}{x(1-x-z)(1-x)^2}L(t, x, z) = \frac{1+z^2}{(1-x-z)(1-z)}\ln\frac{t(1-z)}{(1-x-z)z}. \tag{18}$$

For this reason, the integral in Eq. (17) can be numerically estimated (the inner integral with respect to t is analytically calculated, but the result is unwieldy and is not presented in this brief paper).

The third part of the contribution from the emission of two hard photons is related to the events in which one

photon of energy ω_1 is collinear and the other (of energy ω_2) is emitted within the angle range from $\pi - \theta_0'$ to θ_0. To describe the cross-section form and satisfy conditions (2) and (3) for these events, we set $k_1 = (1 - x)p_1$ according to the approximation used. In this approach, we start with the differential cross section in the form

$$d\sigma_3^H = \sigma(q^2)\frac{\alpha}{2\pi}P(x, L_0)$$

$$\times L_{\mu\nu}^{\gamma}(xp_1, p_2, k_2)\tilde{g}_{\mu\nu}\frac{\alpha}{4\pi^2}\frac{d^3k_2 dx}{\omega_2 xs}, \qquad (19)$$

$$\frac{d^3k_2}{\omega_2} = 2\pi\omega_2 d\omega_2 dc_2, \quad c_2 = \cos\theta_2, \quad x = 1 - \frac{\omega_1}{E},$$

where θ_2 is the polar angle of the noncollinear photon. To obtain the distribution in the squared invariant mass q^2 of pions, it is convenient to use the relationships

$$q^2 = 4E(E - \Omega) + 2\omega_1\omega_2(1 - c_2), \quad \omega_2 = \Omega - \omega_1,$$
$$dc_2 = \frac{dq^2}{2\omega_1\omega_2}, \quad d\omega_2 = d\Omega. \qquad (20)$$

In this case, we can also ignore the electron mass in the leptonic tensor $L_{\mu\nu}^{\gamma}$. The corresponding differential cross section has the form

$$\frac{d\sigma_3^H}{dq^2} = \frac{\sigma(q^2)}{s}\left(\frac{\alpha}{2\pi}\right)^2\left\{P(x, L_0)\left[\frac{2q^4}{xu_1u_2}\right.\right.$$

$$\left.\left. - 2q^2\left(\frac{1}{xu_1} + \frac{1}{u_2}\right) + \frac{xu_1}{u_2} + \frac{u_2}{xu_1}\right]\frac{d\omega_1 d\Omega}{\omega_1(E - \omega_1)}\right\},$$

$$u_1 = -2k_2p_1 = -\frac{4E^2\Omega_z}{\omega_1}, \qquad (21)$$

$$u_2 = -2k_2p_2 = -\frac{4E}{\omega_1}[\omega_1(\Omega - \omega_1) - E\Omega_z],$$
$$\Omega_z = \Omega - E(1 - z).$$

It is instructive to recast the expression in braces in a form convenient for integration with respect to ω_1 and Ω:

$$\left\{-L_0 - \frac{zE^2L_0}{(E - \omega_1)^2} + \frac{[2z - (1 + z)L_0]E}{E - \omega_1}\right.$$

$$\left. + \frac{2(1 + z^2)L_0 - 4z - (1 - z)^2 - (1 - z)(\Omega - 2\omega_1)}{\omega_1(\Omega - \omega_1) - E\Omega_z}\right\} \qquad (22)$$

$$\times \frac{d\omega_1 d\Omega}{E\Omega_z},$$

where we omit the terms whose denominator does not include a small factor Ω_z, which is equal to $\eta\Delta$ in order of magnitude [see Eqs. (24) and (25) for Ω_{max} and Ω_{min}, respectively].

We must now find the domain of integration which is determined by constraints (2) and (3) on the selection of events and by the inequalities

$$-c_0' < c_2 < c_0, \quad E\Delta < \omega_1 < \Omega - E\Delta_1, \quad c_0' = \cos\theta_0' \qquad (23)$$

for the possible angles of noncollinear photon and the energy of collinear one. Condition (2) determines the maximal Ω value, and Eq. (3) determines the minimal ω_1 value for a fixed Ω value:

$$\Omega_{max} = E(1 - z)\left(1 + \frac{\eta}{2}\right),$$
$$\omega_1 \geq \frac{2E\Omega_z}{\Omega - |\mathbf{K}|c_0}, \quad |\mathbf{K}| = \sqrt{\Omega^2 - 4E\Omega_z}. \qquad (24)$$

To obtain the minimal value of Ω Ω_{min}, one should use the first of Eqs. (20) with $\omega_2 = \Delta E$ and $c_2 = c_0$:

$$\Omega_{min}\Delta(1 - c_0) = 2E[\Omega_{min} - E(1 - z)], \longrightarrow \Omega_{min}$$
$$= E(1 - z)\left(1 + \frac{\Delta(1 - c_0)}{2}\right). \qquad (25)$$

It follows from the condition $c_2 > -c_0'$ that

$$\omega^- < \omega_1 < \omega^+,$$
$$\omega^{\pm} = \frac{\Omega}{2}\left[1 \pm \sqrt{1 - \frac{4E\Omega_z}{\Omega^2}\left(1 + \frac{1 - c_0'}{2}\right)}\right]. \qquad (26)$$

Finally, the inequality $c_2 < c_0$ yields

$$\omega_1 > \omega_+ \text{ or } \omega_1 < \omega_-$$
$$if\ \Omega \leq E(1 - z)\left(1 + \frac{(1 - c_0)(1 - z)}{8}\right),$$
$$\omega_{\pm} = \frac{\Omega}{2}\left[1 \pm \sqrt{1 - \frac{8E\Omega_z}{\Omega^2(1 - c_0)}}\right]. \qquad (27)$$

To obtain the domain of integration, it is necessary to combine Eqs. (23)–(27) consistently. As a result, we obtain

$$\omega_{min} < \omega_1 < \omega_- \text{ and } \omega_+ < \omega_1 < \Omega - \Delta E,$$
$$\Omega_{min} < \Omega < E(1 - z)(1 + \Delta),$$
$$\omega_{min} < \omega_1 < \omega_- \text{ and } \omega_+ < \omega_1 < \omega^+,$$
$$E(1 - z)(1 + \Delta) < \Omega < E(1 - z)\left(1 + \frac{(1 - c_0)(1 - z)}{8}\right), \qquad (28)$$

$$\omega_{\min} < \omega_1 < \omega^+,$$

$$E(1-z)\left(1+\frac{(1-c_0)(1-z)}{8}\right) < \Omega < \Omega_{\max},$$

where $\omega_{\min}$ is determined by the inequality in Eq. (24).

The necessary integrals over region (28) are the following:

$$\int\frac{d\omega_1 d\Omega}{E\Omega_z} = (1-z)\left(2-\ln\frac{1+\xi}{\xi}\right), \quad \xi = \frac{\eta}{(1-c_0)(1-z)},$$

$$\int\frac{d\omega_1 d\Omega}{(E-\omega_1)\Omega_z} = -\ln z\ln\xi + Li_2(1-z)$$

$$-Li_2(-\xi z) + Li_2(-\xi) - Li_2\left(-\frac{1-z}{z}\right),$$

$$\int\frac{E d\omega_1 d\Omega}{(E-\omega_1)^2\Omega_z} = \frac{1}{z}\left[-(1+z)\ln z - (1-z)\ln\frac{1+\xi z}{\xi}\right],$$

$$\int\frac{(\Omega-2\omega_1)d\omega_1 d\Omega}{[\omega_1(\Omega-\omega_1)-E\Omega_z]\Omega_z} = -\frac{\pi^2}{6} - \frac{1}{2}\ln^2\frac{1-c_0}{2}$$

$$+\ln\frac{\eta}{2\Delta}\ln\frac{(1-c_0)(1-c_0')}{4} - 2Li_2(-\xi),$$

$$\int\frac{E d\omega_1 d\Omega}{[\omega_1(\Omega-\omega_1)-E\Omega_z]\Omega_z} = \frac{1}{1-z}\left[\frac{\pi^2}{2} + \frac{1}{2}\ln^2\frac{1-c_0}{2}\right.$$

$$\left.-\ln\frac{\eta}{2\Delta}\ln\frac{(1-c_0)(1-c_0')}{4} - \ln^2\xi\right]. \tag{29}$$

Using Eq. (22) and these integrals, one can represent the contribution of the third part from the emission of two photons in the form

$$\frac{d\sigma_3^H}{dq^2} = \frac{\sigma(q^2)}{s}\left(\frac{\alpha}{2\pi}\right)^2[2P(z,L_0)G_1 + L_0G_2 + G_3],$$

$$G_1 = \frac{\pi^2}{2} + \frac{1}{2}\ln^2\frac{1-c_0}{2} - \ln\frac{\eta}{2\Delta}\ln\frac{(1-c_0)(1-c_0')}{4} - \ln^2\xi,$$

$$G_2 = (1-z)\left[-2+\ln\frac{(1+\xi)(1+\xi z)}{\xi^2}\right]$$

$$+(1+z)\left[(1+\ln\xi)\ln z + Li_2(-\xi z) + Li_2\left(-\frac{1-z}{z}\right)\right. \tag{30}$$

$$\left.-Li_2(-\xi) - Li_2(1-z)\right],$$

$$G_3 = -(1-z)\left(\frac{\pi^2}{3} - \ln^2\xi\right) + 2Li_2(-\xi)$$

$$+2z\left[Li_2(1-z) - Li_2(-\xi z) - Li_2\left(-\frac{1-z}{z}\right)\right].$$

5. The total radiative correction to Born cross section (10) is represented as a sum

$$\frac{\sigma^{RC}}{dq^2} = \frac{\sigma^{S+V}}{dq^2} + \frac{\sigma_1^H}{dq^2} + \frac{\sigma_2^H}{dq^2} + \frac{\sigma_3^H}{dq^2}. \tag{31}$$

The auxiliary infrared parameter Δ enters into the terms in Eq. (31) through the expression

$$2P(z,L_0)\ln\Delta\left[2(L_s-1) - (L_0'-1)\right.$$

$$\left.-(L_0-1) + \ln\frac{\theta_0^2\theta_0'^2}{16}\right]. \tag{32}$$

Hereafter, we use the decomposition of c_0 and c_0'. Expression (32) is equal to zero according to the definition of large logarithms L_0, L_s, and L_0' [see Eqs. (8), (12), and (13)]. It is easy to check that the auxiliary angular parameter θ_0' is also canceled in Eq. (31), which can be represented as

$$\frac{d\sigma^{RC}}{dq^2} = \frac{\sigma(q^2)}{s}\left(\frac{\alpha}{2\pi}\right)^2\left\{\frac{1}{2}L_0^2P_{2\theta}(z)\right.$$

$$+P(z,L_0)\left[L_s\left(\frac{3}{2}+2\ln\frac{\eta}{2}\right) + \ln\frac{4}{\theta_0^2}\left(\frac{3}{2}+2\ln\frac{\eta}{z\theta_0}\right)\right. \tag{33}$$

$$\left.\left.-2\ln^2\xi - 2\ln\frac{\eta}{2} + 3\ln z + \frac{5\pi^2}{3} - \frac{9}{2}\right] + L_0F_1 + F_2\right\},$$

where

$$F_1 = \frac{3-8z+z^2}{2(1-z)} - \frac{2(1+z)^2}{1-z}\ln(1-z)$$

$$+\left[\frac{4z}{1-z} + (1+z)(1+\ln\xi)\right]\ln z + \frac{1}{2}(1+z)\ln^2 z$$

$$+\frac{1+z^2}{1-z}\left(\frac{\pi^2}{3} - 2Li_2(z)\right) + (1-z)\ln\frac{(1+\xi)(1+\xi z)}{\xi^2}$$

$$+(1+z)\left[Li_2(-\xi z) + Li_2\left(-\frac{1-z}{z}\right) - Li_2(-\xi) - Li_2(1-z)\right],$$

$$F_2 = (1-z)\ln^2\xi - \frac{3+4z}{3(1-z)} + \frac{4z}{1-z}\ln(1-z)$$

$$+\left[-2z\ln\xi + \frac{3-18z+7z^2}{3(1-z)^2}\right]\ln z + 2z\ln^2(1-z)$$

$$+\frac{3-12z+30z^2-36z^3+7z^4}{6(1-z)^3}\ln^2 z$$

$$+\frac{\pi^2}{6}\left(4+\frac{14z}{3}-\frac{5}{1-z}\right) + Li_2(z)\left(4z-6+\frac{5}{1-z}\right)$$

$$+\left(1-\frac{z}{3}\right)Li_2(1-z)+2Li_2(-\xi)$$

$$-2z\left[Li_2(-\xi z)+Li_2\left(-\frac{1-z}{z}\right)\right]+J.$$

As was mentioned above, the RCs have a factorized form; the low-energy cross section $\sigma(q^2)$ for the pion pair production, which is the object of precision measurements capable of deciding the fate of SM, enters into Eq. (33) as a separate multiplier. Another multiplier (expression in braces) is of purely electrodynamical origin and is independent of the strong pion interaction. It is determined by the squared invariant mass q^2 of pions as well as by the physical parameters η and θ_0, which appear in the ISE rules.

One more contribution to the RCs comes from the emission of two hard photons under the condition that none of them is emitted within a narrow cone in the electron-beam direction but collinear condition (3) is satisfied. This contribution cannot be calculated in the quasi-real electron approximation and should be estimated by other methods. In particular, the leptonic double bremsstrahlung current tensor can be taken in the limit $m \longrightarrow 0$. We intend to calculate it elsewhere, but we are sure that, because of stringent restriction (2) on the event selection, this contribution is small and cannot affect the cross section within a percent accuracy.

The above consideration corresponds to the case where the final $e^+e^-\pi^+\pi^-$ state is excluded from the analysis of the ISE cross section. Otherwise, there would be an extra contribution from the e^+e^- pair production in the initial state [6]. The dominant part of this contribution is related to the collinear kinematics, when an e^+e^- pair is emitted in the electron-beam direction. In the NLO approximation (in our case, it takes into account only the logarithmically enhanced terms), this contribution can be represented as

$$\frac{d\sigma^{e^+e^-}}{dq^2} = \frac{\sigma(q^2)}{s}\left(\frac{\alpha}{2\pi}\right)^2[P_1(z)L_0^2+P_2(z)L_0], \qquad (34)$$

where the functions $P_1(z)$ and $P_2(z)$ can be set off from the corresponding cross section for low-angle Bhabha scattering [12]. In this case, one should estimate the extra background caused by the two-photon mechanism of pion pair production. We intend to analyze this problem elsewhere.

The Born cross section (10) and the corresponding RCs (33) and (34) considered in this work describe events with at least one collinear (with respect to the electron-beam direction) photon or one collinear electron–positron pair. The DAPHNE conditions allow the selection of the same events along the positron beam. For this reason, all contributions should be doubled.

We are grateful to V.A. Khoze and G. Venanzoni for the discussion of ISE rules at DAPHNE.

REFERENCES

1. H. N. Brown, G. Bunce, R. M. Carey, *et al.*, Phys. Rev. Lett. **86**, 2227 (2001).
2. Brookhaven Bulletin, BNL 01-12, February 8, 2001.
3. F. Jegerlehner, Preprint DESY 99-007, hep-ph/9901386; M. Davier and A. Höcker, Phys. Lett. B **419**, 419 (1998); **435**, 427 (1998); A. Czarnecki and W. Marciano, hep-ph/0102122; F. J. Yndurain, hep-ph/0102312.
4. R. R. Akhmetshin *et al.* (CDM-2 Collab.), Preprint Budker INP-99-10; hep-ex/9904027; Nucl. Phys. A **675**, 424 (2000); Phys. Lett. B **475**, 190 (2000).
5. D. Kong, hep-ph/9903521; J. Z. Bai *et al.* (BES Collab.), Phys. Rev. Lett. **84**, 594 (2000).
6. A. B. Arbuzov, E. A. Kuraev, N. P. Merenkov, and L. Trentadue, JHEP **12**, 009 (1998); S. Spangolo, Eur. Phys. J. C **6**, 637 (1999); S. Binner, J. H. Kühn, and K. Melnikov, Phys. Lett. B **459**, 279 (1999); J. Kühn, hep-ph/0101100.
7. V. A. Khoze, M. I. Konchatnij, N. P. Merenkov, *et al.*, Eur. Phys. J. C **18**, 481 (2001).
8. G. Catani, A. Denig, W. Kluge, and G. Venanzoni, KLOE MEMO 195, August 13, 1999.
9. V. N. Baier, V. S. Fadin, and V. A. Khoze, Nucl. Phys. B **65**, 381 (1973).
10. N. P. Merenkov, Yad. Fiz. **48**, 1782 (1988) [Sov. J. Nucl. Phys. **48**, 1073 (1988)].
11. S. Jadach, M. Skrzypek, and B. F. L. Ward, Phys. Rev. D **47**, 3733 (1993).
12. A. B. Arbuzov, E. A. Kuraev, N. P. Merenkov, and L. Trentadue, Zh. Éksp. Teor. Fiz. **108**, 1164 (1995) [JETP **81**, 638 (1995)].

Translated by R. Tyapaev

JETP Letters, Vol. 74, No. 2, 2001, pp. 72–76. Translated from Pis'ma v Zhurnal Éksperimental'noĭ i Teoreticheskoĭ Fiziki, Vol. 74, No. 2, 2001, pp. 76–80.

Asymptotic Behavior of Weakly Collapsing Solutions of the Nonlinear Schrödinger Equation

Yu. N. Ovchinnikov[1,2]* and V. L. Vereshchagin[3]

[1] *Max-Planck Institute for Physics of Complex Systems, D-01187 Dresden, Germany*

[2] *Landau Institute for Theoretical Physics, Russian Academy of Sciences, ul. Kosygina 2, Moscow, 117940 Russia*

** e-mail: ovc@itp.ac.ru*

[3] *Institute of Mathematics and Computer Center, Ural Division, Russian Academy of Sciences, Ufa, 450000 Bashkortostan, Russia*

Received June 21, 2001

The generic asymptotic behavior of a three-parameter weakly collapsing solution of a nonlinear Schrödinger equation is examined. A discrete set of zero-energy states is shown to exist. In the (A, C_1) parameter space, there are two close lines along which the amplitude of oscillating terms is exponentially small in the parameter C_1.

PACS numbers: 03.65.Ge; 02.30.Jr

The nonlinear Schrödinger equation

$$i\frac{\partial\psi}{\partial t} + \Delta\psi + |\psi|^{2\sigma}\psi = 0, \tag{1}$$

where ψ is a scalar function in the d-dimensional space and Δ is the Laplacian, has weakly collapsing solutions of the form

$$\psi(r, t) = \lambda^{\nu}\varphi(\rho\lambda)\exp(i\chi(\rho, t)). \tag{2}$$

Here, $\lambda = \lambda(t)$, φ is a real function, and $\rho = |r|$. Weakly collapsing solutions were studied by Zakharov *et al.* [1–3]. The number of particles and the total energy are conserved for any solution to Eq. (1). These two conservation laws lead to the following equations for the parameter ν and functions λ and χ [4, 5]:

$$\nu\sigma = 1, \quad \chi(\rho, t) = \chi_0(t) + \tilde{\chi}(\rho\lambda),$$
$$\lambda = \frac{C}{\sqrt{t_0 - t}}, \quad \chi_0(t) = \frac{C_1}{2}\ln(t_0 - t), \tag{3}$$

where C and C_1 are constants and t_0 is the time instant of collapse. The set of equations for the functions φ and $\tilde{\chi}$ reduces to one third-order ordinary differential equation [4, 5]

$$Z''' - \frac{(Z'')^2}{2Z'} - \frac{(d-1)(d-3)}{2y^2}Z'$$
$$- \frac{1}{C^2}\left[C_1 Z' - \frac{y(yZ' + (2/\sigma - d)Z)}{4C^2}\right] \tag{4}$$
$$- \frac{(yZ' + (2/\sigma - d)Z)^2}{8C^4 Z'} + \frac{2(Z')^{\sigma+1}}{y^{(d-1)\sigma}} = 0.$$

The functions φ and $\tilde{\chi}$ are expressed in terms of the function Z through the simple relationships

$$\varphi = \frac{\sqrt{Z'}}{y^{(d-1)/2}}, \quad \tilde{\chi}' = -\frac{yZ' + (2/\sigma - d)Z}{4C^2 Z'}. \tag{5}$$

We examine possible types of asymptotic behavior of the solutions to Eq. (4). For simplicity, we consider only the physically most interesting case $d = 3$ and $\sigma = 1$. The parameter C corresponds to the following scale transformation in Eq. (4):

$$y = C\tilde{y}; \quad Z = C\tilde{Z}(\tilde{y}). \tag{6}$$

In what follows, we will set $C = 1$.

Equation (4) has only one one-parameter family of solutions satisfying the physical boundary conditions at the zero point [4, 5]:

$$Z(y) = Ay^3 + Ay^5\left(\frac{C_1}{10} - \frac{3}{5}A\right) + \ldots. \tag{7}$$

To examine the solution in the asymptotic region $y \longrightarrow \infty$, we multiply both sides of Eq. (4) by $8Z'$ and differentiate with respect to y. Omitting immaterial terms, we obtain the linear equation

$$Z'\{4Z'''' + y(Z' + yZ'') - 8C_1 Z'' - Z\} = 0. \tag{8}$$

In the asymptotic region $y \longrightarrow \infty$, the general solution

of this equation has the form

$$Z = By + \frac{B_1}{y}\left(1 + \frac{16C_1}{9y^2} + \ldots\right) - \frac{4}{y^2}(1 + \ldots) \times \left[d_1 \cos\left(\frac{y^2}{4} - 2C_1 \ln y\right) + d_2 \sin\left(\frac{y^2}{4} - 2C_1 \ln y\right)\right], \quad (9)$$

involving expansion in $1/y^2$ powers. Four coefficients B, B_1, d_1, and d_2 are related to one another by a single relationship, which can easily be obtained by substituting Eq. (9) into Eq. (4) (see also [6]):

$$B_1 = -2BC_1 - \frac{(d_1^2 + d_2^2)}{B}. \quad (10)$$

The necessary and sufficient condition for solution (7), (9) to correspond to zero energy has the form

$$d_1 = d_2 = 0. \quad (11)$$

The coefficients d_1 and d_2 are analytical functions of the parameters A and C_1. Therefore, the set of points $\{A, C_1\}$ at which the energy is equal to zero is discrete (finite or infinite). One of these points was numerically calculated in [7]:

$$\{A, C_1\} = \{0.644; 1.09\}. \quad (12)$$

Apart from this point, there are other points corresponding to zero-energy solutions. Some of them are

$$\{A, C_1\} = \{0.365; 3.113\}; \quad (13)$$

$$\{A, C_1\} = \{0.913; 4.41\}; \ \{A, C_1\} = \{0.924; 5.89\};$$

$$\{A, C_1\} = \{1.2619; 7.26\}; \ \{A, C_1\} = \{1.435; 8.66\};$$

$$\{A, C_1\} = \{1.689; 10.04\}; \ \{A, C_1\} = \{1.907; 11.42\};$$

$$\{A, C_1\} = \{2.137; 12.79\}; \ \{A, C_1\} = \{2.362; 14.16\}.$$

Let us now turn to the region of parameters $C_1 \gg 1$. In the region $y \ll \sqrt{C_1}$, Eq. (4) reduces to the simpler equation

$$Z''' - \frac{(Z'')^2}{2Z'} + \frac{2(Z')^2}{y^2} - C_1 Z' = 0. \quad (14)$$

By setting

$$Z' = \phi, \quad (15)$$

we obtain the following second-order equation for the function ϕ:

$$\phi'' - \frac{(\phi')^2}{2\phi} + \frac{2\phi^2}{y^2} - C_1\phi = 0. \quad (16)$$

In the region $1 \ll y \ll \sqrt{C_1}$, the general solution to Eq. (16) has the form

$$\phi = \frac{C_1}{2}y^2 + \tilde{\phi}, \quad (17)$$

where $\tilde{\phi}$ is the solution of the linear equation

$$\tilde{\phi}'' + C_1\tilde{\phi} + \frac{2}{y^2}\tilde{\phi} - \frac{2}{y}\tilde{\phi}' = 0. \quad (18)$$

The general solution of Eq. (18) is

$$\tilde{\phi} = \tilde{B}_1 y \sin(\sqrt{C_1}y) + \tilde{B}_2 y \cos(\sqrt{C_1}y). \quad (19)$$

Therefore, for large C_1 values, the domain of y values exists such that $y \ll \sqrt{C_1}$, where the solutions have the intermediate asymptotic form

$$Z' = \phi = \frac{C_1}{2}y^2 + y(\tilde{B}_1 \sin(\sqrt{C_1}y) + \tilde{B}_2 \cos(\sqrt{C_2}y)). \quad (20)$$

Let us assume that the inequality

$$\left|A - \frac{C_1}{6}\right| \ll C_1 \quad (21)$$

is satisfied. Then the function

$$\phi = \frac{C_1}{2}y^2 + \frac{3y}{\sqrt{C_1}}\left(A - \frac{C_1}{6}\right)\sin(\sqrt{C_1}y) \quad (22)$$

is the solution to Eq. (16) in the region $y \ll \sqrt{C_1}$ and satisfies the boundary conditions for the function Z.

Let us show that, in the $\{A, C_1\}$ plane, there are two close lines along which the amplitudes $d_{1,2}$ in Eq. (9) are exponentially small at large values of parameter C_1. These lines also include those values of parameters A and C_1 for which the energy is zero. Let us multiply both sides of Eq. (4) by Z' and differentiate with respect to y. As a result, the equation for the function Z takes the form

$$Z'''' + \frac{y}{4}(Z' + yZ'') - 2C_1 Z'' - \frac{1}{4}Z = 4(Z')^2/y^3 - 6Z'Z''/y^2. \quad (23)$$

The solution to this equation satisfying the boundary condition at zero can be represented in the form

$$Z = AZ_4 + D_1 Z_1 + D_2 Z_2 + D_3 Z_3 + D_4 Z_4, \quad (24)$$

where the constant A is determined in Eq. (7) and the functions $Z_{1,2,3,4}$ are the solutions of the linear equation

$$Z_k'''' + \frac{y}{4}(Z_k' + yZ_k'') - 2C_1 Z_k'' - \frac{Z_k}{4} = 0, \quad k = 1, 2, 3, 4. \quad (25)$$

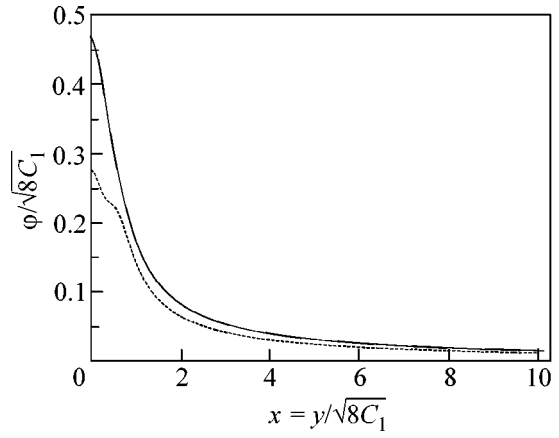

Fig. 1. The functions $\varphi/\sqrt{8C_1}$ at zero-energy points $\{A, C_1\}$ = (solid line) {0.644, 1.09} and (dashed line) {0.913, 4.41}; $x = y/\sqrt{8C_1}$.

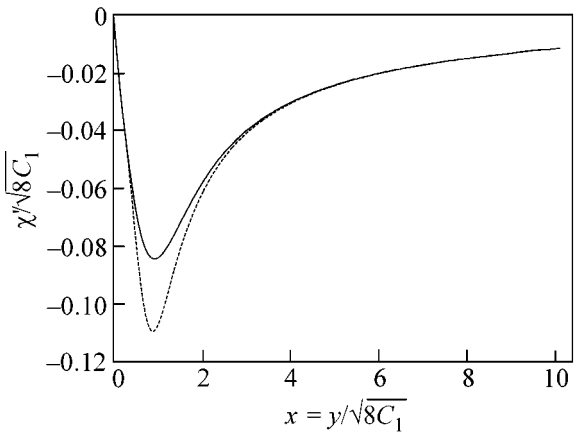

Fig. 2. The same as in Fig. 1 but for the functions $\chi/\sqrt{8C_1}$.

The functions Z_k are taken in the form

$$Z_1 = y, \quad Z_2 = \left[1 + \sum_{n=2}^{\infty} A_n^{(1)} y^{2n}\right],$$
$$Z_3 = y^2\left[1 + \sum_{n=1}^{\infty} A_n^{(2)} y^{2n}\right], \qquad (26)$$
$$Z_4 = y^3\left[1 + \sum_{n=1}^{\infty} A_n^{(3)} y^{2n}\right].$$

The functions D_k in Eq. (24) are expressed through the integrals of the derivatives of function Z:

$$D_k = -\frac{1}{12}\int_0^y dy P_{k4}(4(Z')^2/y^3 - 6Z'Z''/y^2), \qquad (27)$$

where

$$P_{14} = -\det\begin{pmatrix} Z_2 & Z_3 & Z_4 \\ Z_2' & Z_3' & Z_4' \\ Z_2'' & Z_3'' & Z_4'' \end{pmatrix},$$
$$P_{24} = \det\begin{pmatrix} y & Z_3 & Z_4 \\ 1 & Z_3' & Z_4' \\ 0 & Z_3'' & Z_4'' \end{pmatrix},$$
$$P_{34} = -\det\begin{pmatrix} y & Z_2 & Z_4 \\ 1 & Z_2' & Z_4' \\ 0 & Z_2'' & Z_4'' \end{pmatrix}, \qquad (28)$$
$$P_{44} = \det\begin{pmatrix} y & Z_2 & Z_3 \\ 1 & Z_2' & Z_3' \\ 0 & Z_2'' & Z_3'' \end{pmatrix}.$$

In the region $y \ll \sqrt{C_1}$, the functions Z_3 and Z_4 can be represented in the form

$$Z_3 = \frac{1}{C_1}[\cosh(\sqrt{2C_1}y) - Z_2],$$
$$Z_4 = \frac{3}{C_1}\left(\frac{1}{\sqrt{2C_1}}\sinh(\sqrt{2C_1}y) - Z_1\right). \qquad (29)$$

After passing through the turning point $\{y = 2\sqrt{2C_1}\}$, the functions Z_3 and Z_4 acquire oscillating terms, the relation between which is determined with exponential accuracy by Eq. (29). The condition that these terms in Eq. (24) be zero determines those lines in the $\{A, C_1\}$ plane on which the amplitude of the oscillating addition is exponentially small:

$$A + \frac{1}{12}\int_0^{\infty}\left(-\frac{6Z'Z''}{y^2} + 4\frac{(Z')^2}{y^3}\right)$$
$$\times \det\begin{pmatrix} y & Z_2 & T \\ 1 & Z_2' & T' \\ 0 & Z_2'' & T'' \end{pmatrix} = 0, \qquad (30)$$

where $T = (\sqrt{2C_1}/3)Z_4 - Z_3$.

Taking into account Eqs. (26) and (29), Eq. (30) reduces to

$$A + \frac{1}{6}\int_0^\infty dy e^{-\sqrt{2C_1}y}\left(4\frac{(Z')^2}{y^3} - 6\frac{Z'Z''}{y^2}\right) = 0, \qquad (31)$$

which can be recast in a more convenient form

$$A = \int_0^\infty dy \frac{(Z')^2}{y^2}\left\{\sqrt{\frac{C_1}{2}} + \frac{1}{3y}\right\}e^{-\sqrt{2C_1}y}. \qquad (32)$$

The values $y \sim 1/\sqrt{C_1}$ are substantial in Eq. (32). Let us assume that Eq. (32) has a solution in the region

$$\left|A - \frac{C_1}{6}\right| \ll C_1. \qquad (33)$$

In this case, the function Z_1 is determined by Eq. (22). From Eqs. (22) and (32), we obtain

$$\left(A - \frac{C_1}{6}\right)\left\{1 - \frac{1}{2\sqrt{2}}\int_0^\infty dt e^{-t}(3t+2)\sin\left(\frac{t}{\sqrt{2}}\right) - O\left(\frac{A}{C_1} - \frac{1}{6}\right)\right\} = 0. \qquad (34)$$

Because

$$\frac{1}{2\sqrt{2}}\int_0^\infty dt e^{-t}(3t+2)\sin\left(\frac{t}{\sqrt{2}}\right) = 1, \qquad (35)$$

Eq. (32) has two close solutions

$$6A = C_1 + O(1/C_1), \qquad (36)$$

which split only if the terms exponentially small in C_1 are taken into account. Figures 1 and 2 show, respectively, the functions $\varphi/\sqrt{8C_1}$ and $\chi'/\sqrt{8C_1}$ of parameter $x = y/\sqrt{8C_1}$ at zero-energy points $\{A, C_1\} = \{0.644, 1.09\}$ and $\{0.913, 4.41\}$. According to Eq. (22), all functions are smooth with no visible oscillations.

Let us consider the equation

$$\frac{t}{4}(Z' + tZ'') - \frac{1}{4}Z'' - \frac{1}{4}Z = \frac{4}{t^3}(Z')^2 - \frac{6}{t^2}Z'Z''. \qquad (37)$$

It has the following solution Z_0 regular at zero:

$$Z_0 = \frac{t^3}{48} - \frac{t^5}{90} + \frac{2t^7}{2835} + \ldots. \qquad (38)$$

In the region $t \gg 1$, the general solution to Eq. (37) has the form

$$\hat{Z}_0(t \gg 1) = Bt + \frac{B_1}{t} + \ldots. \qquad (39)$$

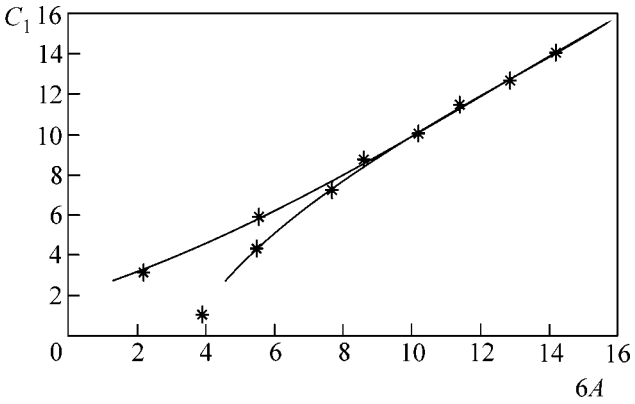

Fig. 3. Zero-energy points in the $\{6A, C_1\}$ plane; the solid lines are determined by Eqs. (42).

We will demonstrate in the forthcoming paper that the zero-energy solutions to Eq. (4) satisfy the estimate

$$\left|\frac{Z(2\sqrt{2C_1}t, C_1)}{(2\sqrt{2C_1})^5} - Z_0(t)\right|/Z_0(t) < \frac{\text{const}}{C_1^2} \qquad (40)$$

uniformly in the solution number and coordinate y. Equation (36) can be refined; in the next order in C_1, it takes the form

$$6A = C_1 + \frac{2}{3C_1} + O(1/C_1^3), \quad C_1 \gg 1. \qquad (41)$$

The zero-energy solutions form at $C_1 \longrightarrow \infty$ two equidistant sets. The parameters A and C_1 of zero-energy solutions satisfy Eq. (41). As the parameter C_1 increases, the accuracy of numerical calculation of the zero-energy points decreases rapidly. In Fig. 3, the points correspond to zero energy. The solid lines correspond to two split lines on which the amplitude of oscillating terms is exponentially small in parameter C_1:

$$6A = \left\{C_1 + \frac{2}{3C_1} - \frac{8}{9C_1^3} + \ldots\right\} \mp 3.3C_1^{1.25}\exp(-0.712C_1). \qquad (42)$$

The derivation of Eq. (42) will be given in the forthcoming paper.

The zero-energy solutions likely do not stand out in any respect among other solutions. Because the integral of the total number of particles diverges, any weakly collapsing solution should be cut off. At nonzero energy, there is a region of parameters A, C, and C_1 where the function φ has a deep minimum at a certain point $y = y^*$ [4, 5]. It is this point which should be taken as the cutoff point. No such point exists at zero energy. Since the solution decreases smoothly, the cutoff should be made at sufficiently large y values. This drastically reduces the probability of formation of the col-

lapsing state. For the generic points $\{A, C, C_1\}$, there exists a set of parameters such that a deep minimum of φ lies at $y \sim 1$ [4, 5]. It should be expected that these are precisely the solutions that will be obtained in numerical calculations or for actual physical objects.

We are grateful to A.B. Shabat and S.V. Iordanskiĭ for valuable remarks. Yu.N. Ovchinnikov acknowledges the support of the CRDF (USA) (grant no. RP1-2251) and the Russian Foundation for Basic Research. V.L. Vereshchagin is grateful for the support of the INTAS (grant no. 99-01782) and the Russian Foundation for Basic Research (project nos. 99-01-00656 and 01-01-00931).

REFERENCES

1. V. E. Zakharov, Zh. Éksp. Teor. Fiz. **62**, 1746 (1972) [Sov. Phys. JETP **35**, 908 (1972)].
2. V. E. Zakharov and L. N. Shchur, Zh. Éksp. Teor. Fiz. **81**, 2019 (1981) [Sov. Phys. JETP **54**, 1064 (1981)].
3. A. Dyachenko, A. C. Newell, A. Pushkarev, and B. E. Zakharov, Physica D (Amsterdam) **57**, 96 (1992).
4. Yu. N. Ovchinnikov, Pis'ma Zh. Éksp. Teor. Fiz. **69**, 387 (1999) [JETP Lett. **69**, 418 (1999)].
5. Yu. N. Ovchinnikov and I. M. Sigal, Zh. Éksp. Teor. Fiz. **116**, 67 (1999) [JETP **89**, 35 (1999)].
6. P. L. Sulem and Catherine Sulem, *Nonlinear Schroedinger Equation: Self-Focusing and Wave Collapse* (Springer-Verlag, Berlin, 1999).
7. V. E. Zakharov and E. A. Kuznetsov, Zh. Éksp. Teor. Fiz. **91**, 1310 (1986) [Sov. Phys. JETP **64**, 773 (1986)].

Translated by R. Tyapaev

JETP Letters, Vol. 74, No. 2, 2001, pp. 77–81. From Pis'ma v Zhurnal Éksperimental'noĭ i Teoreticheskoĭ Fiziki, Vol. 74, No. 2, 2001, pp. 81–85.

Large Amplitude Oscillations Sustained by Stochastic Plasma Density Fluctuations in Plasma Sheaths[1]

G. Sorasio[1], D. P. Resendes[1], and P. K. Shukla[2]

[1] *Centro de Física de Plasmas, Instituto Superior Técnico, 1096 Lisboa Codex, Portugal*

[2] *Institut für Theoretische Physik IV, Fakultät für Physik und Astronomie, Ruhr-Universität Bochum, D-44780 Bochum, Germany*

Received May 21, 2001; in final form, June 13, 2001

We have examined the dynamics of a dust grain immersed in a plasma sheath. It is shown that the presence of stochastic plasma-density variations can sustain large-amplitude dust-grain oscillations once these have been induced by a slow plasma number density variation. Such dust oscillations have been observed in the sheath region of a radiofrequency or dc plasma discharge at very low pressures. A physical mechanism for the excitation and maintenance of large-amplitude grain oscillations is discussed. © *2001 MAIK "Nauka/Interperiodica".*

PACS numbers: 52.27.Lw; 52.40.Hf; 52.35.-g

About seven years ago, several groups [1–5] reported experimental observations of dust crystals in radiofrequency (rf) and dc plasma discharges. It was observed that charged dust grains may, in fact, not only levitate in the sheath of an rf or dc plasma discharge, but also "crystallize" due to a strong intergrain coupling. In laboratory experiments on the Earth, the negatively charged dust grains of a plasma crystal are suspended/levitated over a negatively biased electrode owing to a balance between the sheath electric and gravity forces. Numerous properties [6–8] of these new plasma states, as well as their phase transitions [9, 10], were investigated, since the individual grains can be visualized and followed kinetically. The presence of gravity restricts the experiments that can be carried out on the Earth. However, under microgravity conditions [11], new features appear in the dust grain dynamics and collective interactions involving heartbeat instability and the formation of dust voids and vortices.

The dynamics of a dust particle at high pressure is dominated by neutral drag, which damps its motion. The situation changes when the pressure is reduced to a few millitorr. Several experiments have recently been carried out and careful observations have been made under very low gas pressures [12–15]. Under low pressures, the dust crystal is organized in a single layer. Nunomura *et al.* [14] reported that in the 1–10 mtorr range a reduction of the plasma number density induces large-amplitude vertical grain oscillations. Such oscillations were observed in both one- and two-dimensional dust crystals [12, 13]. It was reported that the neighboring grains do not necessarily oscillate coherently; some do not oscillate at all, while others, with oscillation amplitude larger than a critical value (~1 mm), drop onto the negative electrode. The typical oscillation frequency is in the range 10–14 Hz.

When a dust grain is immersed in an electron–ion plasma, it needs a finite time to acquire an equilibrium charge that is defined to be the charge that results from a zero net current onto the dust grain surface. Assuming that the electron current is dominant, we can estimate the charging time of a dust particle when it has reached an equilibrium potential. Considering a plasma electron temperature $T_e = 1$ eV, an electron number density $n_0 \sim 1 \times 10^8$ cm^{-3}, and a particle radius $R = 2.5$ μm, we obtain a charging time $\tau \sim 6 \times 10^{-4}$ s [16]. The charge delay of a dust particle can be important in the dust dynamics and give rise to many effects that have been studied by several authors [17, 18]. An index of the importance of the charge delay for an oscillating dust particle is the ratio between the characteristic grain charging time and the grain oscillation time. In our case, this ratio is $N_D \sim 6 \times 10^{-3}$. As pointed out by Nitter *et al.* [19], when N_D is small the effect of the charge delay can be neglected. Accordingly, in the following, we will not consider the damping of dust oscillations due to the charge delay.

A negatively charged dust grain levitated over an electrode in a plasma chamber is trapped in a potential well. In this letter, we show that under low pressure conditions the potential well is strongly dependent on the plasma number density n_0. Small variations in the plasma number density (~1% n_0) modify the shape of the potential well as well as the position of its stable equilibrium point, leading to large amplitude vertical oscillations of the dust grains. Under appropriate circumstances, the sensitivity of the potential well to the plasma number density increases as the plasma number

[1] This article was submitted by the authors in English.

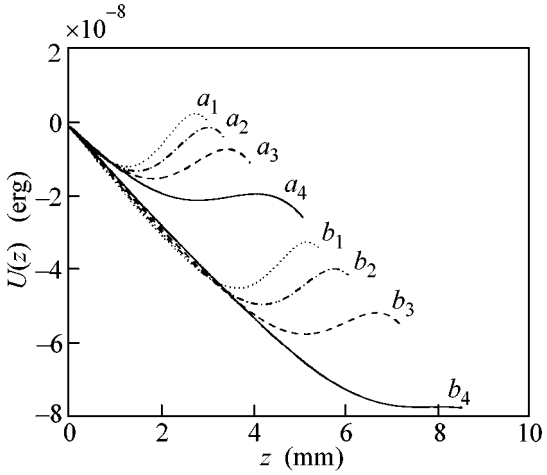

Fig. 1. Profiles of the potential energy of a dust grain in the sheath region: (*a*) curves correspond to P = 20 mtorr, and (*b*) curves correspond to P = 1 mtorr. The plasma number densities are: (a_1, b_1) 4×10^8 cm^{-3}, (a_2, b_2) 3×10^8 cm^{-3}, (a_3, b_3) 2×10^8 cm^{-3}, and (a_4, b_4) 1×10^8 cm^{-3}. The grain radius is R = 2.9 μm.

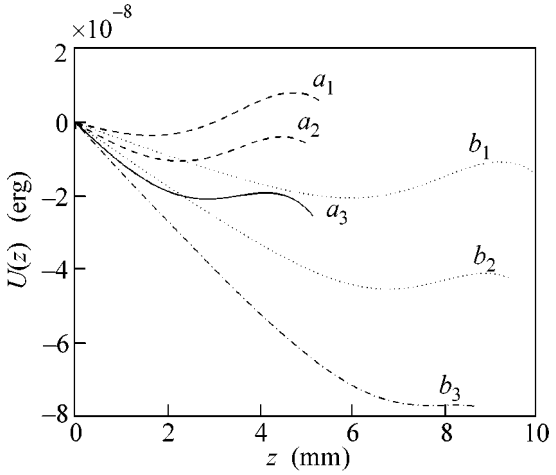

Fig. 2. Profiles of the potential energy as a function of position: (*a*) curves are calculated at P = 20 mtorr, and (*b*) curves at P = 1 mtorr. (a_1, b_1) R = 2 μm, (a_2, b_2) R = 2.5 μm, and (a_3, b_3) R = 2.9 μm. The parameters are the same as in Fig. 1 except for the plasma number density, which is fixed at $n_0 = 1 \times 10^8$ cm^{-3}.

density decreases. The lower the plasma density, the greater the importance of small variations that can create and sustain oscillations. If the plasma number density is decreased below a critical value (n_{0C}) that depends on the grain radius R and the background pressure P, the grain will eventually fall onto the electrode, its kinetic energy being larger than the potential-well confinement. This point will be discussed further in connection with Figs. 1 and 2.

In the following, we have examined the dynamics of an isolated dust grain, but the results of the investigation are expected to be applicable to linear chains and sheets. In a 2D crystal, if we consider an electron Debye radius $\simeq$430 μm (equal to the intergrain separation distance) and an average grain charge $|Q/e| \approx 10^4$ (with Q and e the grain and elementary charges, respectively), the interaction energy is $U_{\rm int} = (Q^2/R)\exp(-R/\lambda_{D_e}) \sim 10^{-10}$ erg. As will become clear, the horizontal interaction energy is two orders of magnitude smaller than the external vertical interaction energy.

We consider a one-dimensional, source-free, weakly collisional glow discharge model [20] to describe the unmagnetized sheath region. As the dust particles do not contribute significantly to the total space charge, since $|Qn_d/en_0| \ll 1$, we assume an "empty sheath" [19]. In order to focus our attention on the importance of stochastic plasma number density fluctuations, we have kept the pressure constant (P = 1–20 mtorr) and no pressure oscillations are considered.

In the sheath, the electrons are thermalized and their number density is $n_e = n_0\exp(e\phi_s/k_BT_e)$, where k_B is the Boltzmann constant, ϕ_s is the electrostatic potential, and T_e is the electron temperature. The ions, which are accelerated in the sheath region, experience a drag force $\mathbf{F}_c = m_i\nu_{in}\mathbf{v}_i$ due to collisions with neutrals. Consequently, an ion, on average, loses its momentum while traveling through the sheath. Here, m_i is the ion mass, $\nu_{in} = n_n\sigma_s v_i$ is the ion-neutral collision frequency, n_n is the neutral gas number density, $\mathbf{v}_i$ is the ion velocity, and σ_s is the momentum-transfer cross section for collisions between ions and neutrals. Elastic and charge exchange are the main collision mechanisms in the sheath, and its cross section is almost constant over the energy range of interest (1–100 eV). The cross section for collisions between ions and neutrals, σ_s, is typically 5×10^{-15} cm^2 [21] over the energy range that is appropriate for dusty plasma laboratory experiments. The ions obey the continuity equation $\nabla\cdot(n_i\mathbf{v}_i) = 0$ and the steady state equation of motion $m_i(\mathbf{v}_i\cdot\nabla\mathbf{v}_i) = -e\nabla\phi_s - F_c$. Here, n_i is the ion number density. Introducing Poisson's equation, we obtain a complete set of differential equations describing the plasma sheath region. In the Gaussian unit, they are

$$v_i\frac{dv_i}{dz} = -\frac{e}{m_i}\frac{d\phi_s}{dz} - n_n\sigma_s v_i^2 \qquad (1)$$

and

$$\frac{d^2\phi_s}{dz^2} = -4\pi e n_0\left[\frac{v_{i0}}{v_i} - \exp\left(\frac{e\phi_s}{k_BT_e}\right)\right], \qquad (2)$$

where z is the particle distance from the sheath edge (z = 0). The electrode is at $z = D$. The ion velocity v_{i0} at the sheath edge, following the Bohm criterion, is the ion sound velocity. The electrostatic potential and the ion acceleration are chosen to be zero at the sheath edge

[22]. The latter condition leads to $d\phi/dx|_{z=0} = -m_i n_n \sigma_s v_i^2/e$.

The sheath model gives the ion and electron number densities n_i and n_e, the ion velocity v_i, and the electrostatic potential ϕ_s. Thus, one can calculate the forces that act on a dust particle and that are responsible for its equilibrium. For our parameters, the main forces are the electrostatic force acting vertically upwards and gravity and ion drag acting vertically downwards. Since the damping due to charge delay is negligible, the friction is due only to neutral drag. We consider a dust particle of size 2.9 μm and the mass density $\rho = 1.3$ g/cm^3.

As we already pointed out, the charge delay is so small that the grain is always in the equilibrium potential relative to its position in the sheath. Since the grain radius R is much smaller than the Debye radius (≈430 μm) and the Debye length is much less than the neutral collision mean free path (~10 cm), we can use the orbital motion limited (OML) theory [23] to obtain the collection currents. For the ion current, we replace the thermal velocity and energy terms in the OLM expression by the mean speed $v_s = \sqrt{8k_BT_i/\pi m_i + \bar{v}_i^2}$. Here, $\bar{v}_i = v_i - v$ is the ion speed relative to a dust grain moving with velocity v. The ion current thus may be regarded as a monoenergetic current if the ion velocity is large compared to the ion thermal velocity and as a spherically symmetric current in the opposite limit [24]. The normalized potential $y(z) \equiv e(\phi_g - \phi_s)/k_BT_e$ can now be calculated equating the sum of the electron and ion currents to zero. The electric force, considering a conducting dust grain, can be expressed as $F_e(z, v) = Q(z, v)E(z)$, where $Q(z, v) = k_BT_eRy(z, v)/e$.

In the sheath region, there is a continuous flow of ions towards the electrode driven by the electric field. The momentum transferred by the ions to the dust grain consists of two components: the collection and the orbit forces [24, 25]. It is found that the latter dominates since the collection radius is much smaller than the impact radius, $(b_\pi/2)$. The orbit force is [25]

$$F_{io}(z, v) = 4\pi n_i v_{th_i} \tilde{v}_s m_i \bar{v}_i b_{\frac{\pi}{2}}^2 \Gamma, \qquad (3)$$

where $b_{\frac{\pi}{2}}^2 = (eQ)^2/(m_i\bar{v}_i^2)^2$ and $\Gamma = \frac{1}{2}\ln(1 + b_{\max}^2/b_{\min}^2)$. The maximum and minimum impact parameters, corresponding to maximum and minimum deflection angles, are $b_{\max} = \bar{\lambda} = (2n_e\lambda_{D_e} + n_i\lambda_{D_i})/(n_e + n_i)$ and $b_{\min} = r_p$, respectively. Here, the ion and electron Debye radii are $\lambda_{D_i} = [4\pi e^2 n_i/((1/2)m_i\bar{v}_i^2 + k_BT_i)]^{-1/2}$ and $\lambda_{D_e} = (4\pi e^2 n_e/k_BT_e)^{-1/2}$, respectively.

In the low-pressure regime, the molecular mean free path ($l \sim 10$ cm) is larger than the grain dimension (i.e., $K_n = l/R \gg 1$). In such a "free-molecular regime," taking into consideration that the dust mass m_d is 12 orders of magnitude larger than the gas molecules, the drag force for specular reflection is [24, 26]

$$F_{n_d}(v) = -(8/3)\sqrt{2\pi}r_p^2 n_n k_B T_n (v/v_{th_n}),$$

where $v_{th_n} = \sqrt{T_n/m_n}$ is the neutral thermal speed.

The total force F_t that acts on a dust particle is $F_t = F_e + F_g + F_{io} + F_{nd}$, where $F_g = \frac{4}{3}\pi R^3 \rho g$ and g represents gravity. The potential energy obtained for zero grain speed $U_t(z) = -\int_0^z dz' F_t(z')$ results from the total force as a function of z, and its shape and equilibrium points are strongly dependent on the discharge parameters.

The equations of motion for a dust grain, in normalized units, are

$$dz/dt = v \qquad (4)$$

and

$$dv/dt = \tau_0 F_t/m_p v_0. \qquad (5)$$

In Eqs. (4) and (5), although the same symbols are used, they are to be understood as normalized quantities. Thus, z is normalized to the ion Debye length in the plasma, the time is normalized to $\tau_0 = \sqrt{m_i/32n_0e^2}$, the total force F_t is normalized to $(k_BT_e/e)^2$, and the velocity is normalized to $v_0 = v_{thi} = \sqrt{8k_BT_i/\pi m_i}$.

Figure 1 shows the potential energy $U(z)$ for different plasma densities ($n_0 = 4\times10^8$–3×10^8 – 2×10^8–1×10^8 cm^{-3}) at two different pressures $P = 1$ mtorr and $P = 20$ mtorr. The grain radius is $R = 2.9$ μm. The argon plasma parameters are $T_e = 1$ eV, $T_i = 0.05$ eV, and $T_n = 0.05$ eV. At $P = 1$ mtorr, the potential energy depends strongly on the plasma density. As the plasma density decreases, the potential well becomes wider and the wall on electrode side becomes lower. When the plasma density is $n_0 = 1\times10^8$ cm^{-3}, the confining potential almost disappears. Below the critical plasma number density $n_{0c}(P, R) = 0.96\times10^8$ cm^{-3}, the grain confinement vanishes and the particle falls onto the electrode. It is important to observe that the energy a particle would gain from a jump in the plasma number density from 2×10^8 cm^{-3} to 1×10^8 cm^{-3} is 1.2×10^{-8} erg and is 10 times larger than the energy that the particle would gain with the same jump but from 4×10^8 cm^{-3} to 3×10^8 cm^{-3}. Further, even a small plasma density fluctuation (~0.1%) near 1×10^8 cm^{-3} is able to offset the neutral damping. As an example, we can consider a grain velocity of $v = 4$ cm/s (conservative hypothesis) at 1 mtorr pressure (with $n_n = 1.16\times10^{13}$ cm^{-3}). The neutral drag force resulting from these values is $F_{nd} = 4.3\times10^{-11}$ dyne. If we consider an average 0.1% plasma number density fluctuation near $n_0 = 1\times10^8$ cm^{-3} the

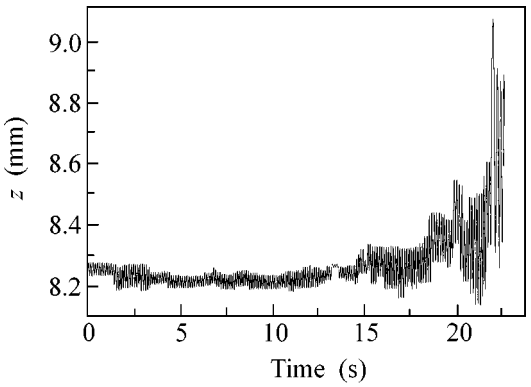

Fig. 3. Position of an oscillating dust grain in the sheath as a function of time. The parameters are the same as in Fig. 1 except for P = 1 mtorr. The plasma number density decreases from 1.5×10^8 cm^{-3} to 0.96×10^8 cm^{-3} over a time interval of 23 s.

vertical energy gain would be $\sim 1.2 \times 10^{-11}$ erg. Considering an oscillation amplitude of 1 mm, the resulting force would be $\sim 1.2 \times 10^{-10}$ dyne, more than enough to offset the neutral damping and sustain the oscillations. From Fig. 1 (with P = 1 mtorr), it can be argued that when a grain gains enough energy, it can fall onto the electrode. In other words, if the amplitude of the oscillations is larger than a critical value, the grain simply falls. On the other hand, when the pressure is higher (viz. P = 20 mtorr), the neutral friction is large and the energy gain for the same step described above (at P = 1 mtorr) is five times smaller. In the high-pressure regimes, the stochastic plasma number density fluctuations described in this letter do not influence the grain dynamics.

In Fig. 2, the potential energy profiles are represented as a function of position for different grain radii (R = 2.9 – 2.5 – 2 μm) and for different values of pressures (P = 1 mtorr and P = 20 mtorr). The parameters are the same as in Fig. 1, except for the plasma number density, which is now $n_0 = 1 \times 10^8$ cm^{-3}. Different grains have different equilibrium positions, and the heavier the grain, the lower the electrode side of the potential well. Therefore, the influence of plasma number density variations changes with the grain radius, with the light particles being more stable.

In a real experiment, plasma density fluctuations are always present. In our numerical simulation, the amplitude of the fluctuation is random with a maximum value of 2% n_0. The plasma density variations have a random time frequency with a maximum time step of 0.3 s. Since the fluctuations are random in amplitude and frequency, they can actually either excite or damp the dust oscillations. Thus, some grains will gain energy and will have a large-amplitude oscillation, some will stand still, and others may actually fall onto the electrode.

Figure 3 shows the position of a dust grain as a function of time for a particle of radius R = 2.9 μm immersed in a plasma sheath at a constant background pressure P = 1 mtorr. The simulation stops when the grain falls onto the electrode. The plasma number density decreases from $n_0 = 1.5 \times 10^8$ cm^{-3} to $n_0 = 0.96 \times 10^8$ cm^{-3}. We presume that stochastic density fluctuations are always present in the plasma sheath [8], and in order to have a plasma number density reduction, we impose negative fluctuations 55% of the time. This is done to simulate experimental procedures whereby the plasma number density is decreased very slowly. At the beginning of the simulation, the plasma number density oscillates around a quasi fixed value (at P = 1.5 mtorr). As the plasma number density is slowly decreased on average, at some point the grain starts to oscillate with a high amplitude displaying a threshold behavior. For the simulation run presented in Fig. 3, the grain oscillation amplitude suddenly increases after roughly 15 seconds, corresponding to a plasma density of 1.2×10^8 cm^{-3}.

To summarize, we have presented a novel mechanism that explains the salient features of dust grain oscillations which are observed in several dusty plasma experiments performed at low pressures [12–15]. The grain gains energy from the plasma number density reduction and stochastic plasma density fluctuations which are always present, but they are relevant only in the 1–10 mtorr pressure range when the neutral drag is weak. Depending on the final value of the plasma number density, either large amplitude dust grain oscillations appear, which are subsequently sustained due to random density fluctuations, or the grains actually fall onto the electrode. The dust oscillation frequencies that result from our simulation (9–11 Hz) are comparable with the frequencies that are observed experimentally [14].

G. Sorasio thanks R. Fonseca, L.O. Silva, N. Lopes, G. Figueira, and J.M. Dias for helpful discussions. This work was partially supported by the European Commission (Brussels) through contract no. HPRN-CT-2000-00140 for performing the task of the Human Potential Research Training Network “Complex Plasmas: The Science of Laboratory and Colloidal Plasmas and Mesospheric Charged Aerosols.” The authors also acknowledge the support of the International Space Science Institute at Bern (Switzerland) for the team “Complex Plasmas in Space: Applications to Solar System and Near Earth Space.”

REFERENCES

1. J. H. Chu, J. B. Du, and Lin I, Phys. Rev. Lett. **72**, 4009 (1994).
2. H. Thomas, G. E. Morfill, V. Demmel, *et al.*, Phys. Rev. Lett. **73**, 652 (1994).
3. A. Melzer, T. Trottenberg, and A. Piel, Phys. Lett. A **191**, 301 (1994).
4. Y. Hayashi and K. Tachibana, Jpn. J. Appl. Phys. **33**, L804 (1994).

5. V. E. Fortov, A. P. Nefedov, V. M. Torchinskiĭ, *et al.*, Pis'ma Zh. Éksp. Teor. Fiz. **64**, 86 (1996) [JETP Lett. **64**, 92 (1996)].
6. G. Morfill, H. M. Thomas, and M. Zuzic, in *Advances in Dusty Plasmas*, Ed. by P. K. Shukla *et al.* (World Scientific, Singapore, 1997), p. 99.
7. V. E. Fortov *et al.*, Phys. Plasmas **6**, 1759 (1999); G. Morfill, H. M. Thomas, U. Konopka, and M. Zuzic, Phys. Plasmas **6**, 1769 (1999); H. Totsuji, Phys. Plasmas **8**, 1856 (2001).
8. P. K. Shukla, Phys. Rev. Lett. **84**, 5328 (2000); Phys. Plasmas **8**, 1791 (2001).
9. H. M. Thomas and G. E. Morfill, Nature **379**, 806 (1996); G. Morfill and H. M. Thomas, J. Vac. Sci. Technol. A **14**, 490 (1996).
10. F. Melandsø, Phys. Rev. E **55**, 7495 (1997); V. V. Zhakhovskiĭ, I. Molotkov, A. P. Nefedov, *et al.*, Pis'ma Zh. Eksp. Teor. Fiz. **66**, 419 (1997) [JETP Lett. **66**, 420 (1997)]; K. Avinash and P. K. Shukla, Phys. Lett. A **255**, 82 (1999); **258**, 195 (1999).
11. G. Morfill, H. M. Thomas, U. Konopka, *et al.*, Phys. Rev. Lett. **83**, 1598 (1999); V. Fortov *et al.*, Phys. Scr. T **T89**, 12 (2001); H. Thomas *et al.*, Phys. Scr. T **T89**, 16 (2001).
12. T. Misawa *et al.*, Jpn. J. Appl. Phys. **39**, L551 (2000).
13. T. Misawa, N. Ohno, K. Asano, *et al.*, Phys. Rev. Lett. **86**, 1219 (2001).
14. S. Nunomura, T. Misawa, N. Ohno, *et al.*, Phys. Rev. Lett. **83**, 1970 (1999).
15. S. Takamura *et al.*, in *Frontiers in Dusty Plasmas*, Ed. by Y. Nakamura, T. Yokota, and P. K. Shukla (Elsevier, Amsterdam, 2000), p. 337.
16. R. C. Hazelton and E. J. Yadlowsky, IEEE Trans. Plasma Sci. **22**, 91 (1994).
17. F. Melandsø, T. K. Aslaksen, and O. Havnes, J. Geophys. Res. **98 (**A8), 13315 (1993); P. K. Shukla, Phys. Lett. A **268**, 100 (2000).
18. J. R. Hill and D. A. Mendis, Moon Planets **23**, 53 (1980).
19. T. Nitter, T. K. Aslaksen, F. Melandsø, and O. Havnes, IEEE Trans. Plasma Sci. **22**, 159 (1994).
20. T. E. Sheridan and J. Goree, Phys. Fluids B **3**, 2796 (1991).
21. D. L. Book, in *NRL Plasma Formulary*, NRL publication (1990), pp. 177–4405.
22. T. Nitter, Plasma Sources Sci. Technol. **5**, 93 (1996).
23. B. Walch, M. Horányi, and S. Robertson, Phys. Rev. Lett. **75**, 838 (1995).
24. M. Barnes *et al.*, Phys. Rev. Lett. **68**, 313 (1992).
25. D. Winske and M. E. Jones, IEEE Trans. Plasma Sci. **22**, 454 (1994).
26. M. J. Baines *et al.*, Mon. Not. R. Astron. Soc. **130**, 63 (1965).

JETP Letters, Vol. 74, No. 2, 2001, pp. 82–83. Translated from Pis'ma v Zhurnal Éksperimental'noĭ i Teoreticheskoĭ Fiziki, Vol. 74, No. 2, 2001, pp. 86–87.

New Magnetically Ordered $CoBO_3$ Crystal

M. L. Afanas'ev, A. D. Balaev, A. D. Vasil'ev, D. A. Velikanov, S. G. Ovchinnikov, G. A. Petrakovskiĭ, and V. V. Rudenko

Kirenskiĭ Institute of Physics, Siberian Division, Russian Academy of Sciences, Akademgorodok, Krasnoyarsk, 660036 Russia

Received June 7, 2001

Crystals of a new $CoBO_3$ compound were synthesized from a solution in melt. According to the X-ray diffraction data, $CoBO_3$ crystallizes in the calcite structure with lattice parameters $a_H = 4.631 \pm 0.005$, $c_H = 14.51 \pm 0.01$ Å. Measurements on SQUID and vibrating-coil magnetometers suggested that $CoBO_3$ is a magnetically ordered crystal with a saturation magnetization of 50 emu/g in the basal plane at 4.2 K and a Néel temperature of 53 K. © *2001 MAIK "Nauka/Interperiodica".*

PACS numbers: 75.50.Ee; 75.60.Ej

In recent years, antiferromagnetic 3D metal oxides have attracted widespread attention as Mott–Hubbard insulators with strong electron correlation. Upon doping, copper oxides become high-temperature superconductors, while manganese oxides exhibit the colossal magnetoresistance effect. A series of 3D metal borates MBO_3 (M = Ti, V, Cr, Fe) provide an example of one more class of isostructural oxides [1] with strong electron correlation, among which $FeBO_3$ is the most familiar, and its solid solutions $V_{1-x}Fe_xBO_3$ were found to undergo concentration transition of the metal–insulator type [2]. We developed a method for synthesizing a new member of this crystal family—$CoBO_3$. Up to now, the possibility of this compound existing has seemed to be highly conjectural. However, our systematic work on the preparation of compounds containing Co^{3+} ions and stable at relatively high temperatures provided a way of synthesizing $CoBO_3$ crystals from a solution in melt. The crystals were synthesized using components of the $Na_3[Co(NO_2)_6] \cdot (1/2)H_2O$–$Na_2B_4O_7 \cdot 10H_2O$–$B_2O_3$–$PbO$–$PbF_2$ system and obtained as black plates with a diameter up to 0.5 mm.

This work reports the results of studying the crystal structure and magnetic properties of $CoBO_3$.

To identify the compound, a plate-shaped crystal of size about 0.3 mm was placed in a KM-4 (KUMA-diffraction) X-ray diffractometer. The reflection intensities and Bragg angles suggested that the parameters of this compound were similar to those of crystal borates $TiBO_3$, VBO_3, $CrBO_3$ [1], and $GaBO_3$ [3]. One could

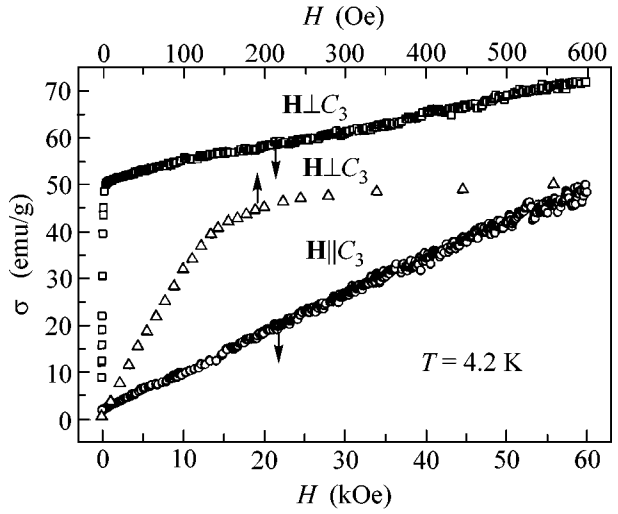

Fig. 1. Field dependences of the magnetization of $CoBO_3$ crystals at $T = 4.2$ K.

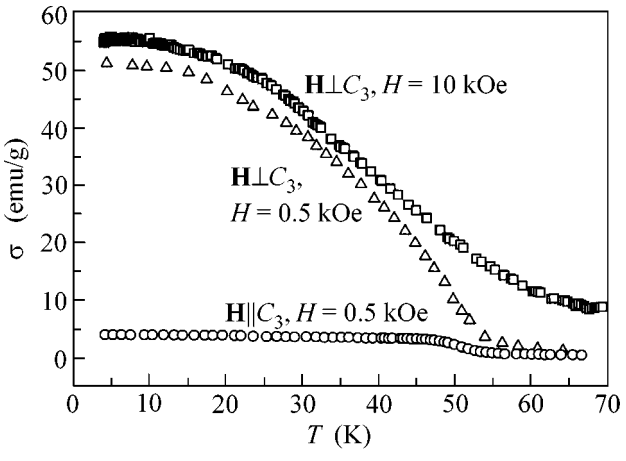

Fig. 2. Temperature dependences of the magnetization of $CoBO_3$ crystals.

0021-3640/01/7402-0082$21.00 © 2001 MAIK "Nauka/Interperiodica"

thus infer that the sample under study had a $CoBO_3$ composition and crystallized in the calcite structure with lattice parameters $a_H = 4.631 \pm 0.005$ and $c_H = 14.51 \pm 0.01$ Å (space group D_{3d}^6).

The magnetic measurements were performed on SQUID and vibrating-coil magnetometers over the temperature range 4.2–77 K in fields up to 60 kOe for crystals with a diameter ranging from 0.2 to 0.5 mm. The field dependences of the magnetization of the $CoBO_3$ samples at a temperature of 4.2 K are shown in Fig. 1. The temperature dependence of the magnetization is presented in Fig. 2. The squares correspond to $H = 10$ kOe, and the triangles are for $H = 500$ Oe. The circles are the data for $H = 500$ Oe.

These data suggest that $CoBO_3$ is an antiferromagnet with weak ferromagnetism and the magnetic moment lying in the basal plane. The extrapolation of magnetization gives $T_N = 53$ K.

For comparison, we present the data on σ for other weakly ferromagnetic crystals at $T = 0$ K: 4 emu/g in $FeBO_3$ [4] and 12 emu/g in $CoCO_3$ [5]. These data give evidence for the presence of strong anisotropic interactions in cobalt borate.

We are grateful to A.I. Pankrats for discussion of the results. This work was supported by the Russian Foundation for Basic Research, project no. 99-02-17405.

REFERENCES

1. H. Schmid, Acta Crystallogr. **17**, 1080 (1964).
2. M. L. Afanas'ev, S. G. Ovchinnikov, N. V. Kazak, and E. P. Popel, in *Proceedings of the XVII International School-Workshop "New Magnetic Materials of Microelectronics," Moscow, 2000*, p. 690.
3. T. A. Bither and H. S. Yung, J. Solid State Chem. **6**, 502 (1973).
4. M. P. Petrov, G. A. Smolenskiĭ, A. P. Paugurt, *et al.*, Fiz. Tverd. Tela (Leningrad) **14**, 109 (1972) [Sov. Phys. Solid State **14**, 87 (1972)].
5. A. S. Borovik-Romanov and V. I. Ozhogin, Zh. Éksp. Teor. Fiz. **39**, 27 (1960) [Sov. Phys. JETP **12**, 18 (1960)].

Translated by V. Sakun

JETP Letters, Vol. 74, No. 2, 2001, pp. 84–86. Translated from Pis'ma v Zhurnal Éksperimental'noĭ i Teoreticheskoĭ Fiziki, Vol. 74, No. 2, 2001, pp. 88–91.

Excitation of 2D Plasmons in a Cs/W(110) System

G. V. Benemanskaya*, K. E. Rovinskiĭ*, and G. É. Frank-Kamenetskaya**

** Ioffe Physicotechnical Institute, Russian Academy of Sciences, Politekhnicheskaya ul. 26, St. Petersburg, 194021 Russia*

*** St. Petersburg Institute of Technology, Zagorodnyĭ pr. 49, St. Petersburg, 198013 Russia*

Received June 13, 2001

The evolution of surface photoemission spectra was investigated for a Cs/W(110) system with metastable Cs coatings larger than a monolayer. It is demonstrated that 2D plasmons can be detected by threshold photoemission spectroscopy. Three photoemission peaks were observed, whose dependence on the Cs adsorption dose showed a complicated behavior. The peaks may be due to the photoinduced excitation of a plasmon in quasi-2D Cs clusters, a surface Cs plasmon, or an interface Cs–W plasmon. © *2001 MAIK "Nauka/Interperiodica".*

PACS numbers: 73.20.Mf; 79.60.Dp

Interest in studying collective electron oscillations in thin layers of alkali metals is caused by the fact that these objects serve as an ideal model for the theoretical description of many-body effects in the solid state. Nevertheless, the problem of experimental search for and identification of various quasi-two-dimensional (2D) collective modes is still far from being solved [1–6]. Moreover, the studies of metal nanoclusters have become particularly topical in recent years in connection with the design of nanostructures and quantum dots on the superconductor surfaces. That is why the elucidation of the nature of plasma modes and of the dependence of their frequencies on the coating thickness and substrate material seems to be important for the understanding of the processes of formation of ultrathin metal coatings.

The plasma 2D oscillations in the systems with cesium coatings were observed only for the Ag [1], Al [3], GaAs [7, 8], and Si [9] substrates. In [1, 3], three spectral features (2.0, 2.4, and 2.9 eV) were observed for the Cs coatings consisting of ~10 monolayers. These features were assigned to the surface multipolar, surface Cs, and bulk Cs plasmons, respectively. The plasmon modes of different frequencies were observed for the cesium coatings on semiconductor surfaces. For instance, the features observed upon the deposition of two Cs monolayers on the Si(100)2x1 surface were assigned in [9] to an interface Cs–Si plasmon (~1.0 eV), a surface Cs plasmon (~2.2 eV), and a bulk Cs plasmon (~3.2 eV). In [7, 8], the peaks observed in the electron energy loss spectra of a Cs/GaAs system were assigned to the plasma oscillations in Cs clusters. Nevertheless, the available experimental data fall short of being sufficient to elucidate the nature of plasma oscillations and to determine the role of the substrate and the regularities in the formation of the 2D plasmon spectra. Besides, 2D plasmons in the cesium coatings on the W surface have not been studied so far.

The electron energy loss method is most popular in studying the collective electronic excitations in metals [2, 3, 7, 8]. However, the experimental results obtained by this method are hard to interpret [4]. In two recent studies [4, 5], ultraviolet photoemission spectroscopy was used instead. It was demonstrated that this method offers considerable advantages in the interpretation of the experimental results and allows the surface plasma modes to be excited by a *p*-polarized radiation.

We have suggested a new method for studying 2D plasmons in thin metal coatings with the use of a *p*-polarized excitation in the threshold photoemission region. This method is an elaboration of threshold photoemission spectroscopy, which possesses higher surface sensitivity and energy resolution (<0.02 eV) in studying surface states, as compared to traditional ultraviolet photoemission spectroscopy. Threshold photoemission spectroscopy was used to study the surface states induced by the local interaction of the Cs adatoms with metal [10, 11] and semiconductor [12, 13] surfaces.

In this work, the surface photoemission spectra were studied in detail for the Cs/W(110) system in different adsorption regimes. The so-called dynamic deposition regime was used in order to obtain metastable Cs coatings of more than one monolayer. With an increase in the dose of adsorbed Cs, a band corresponding to the local interaction of the Cs adatoms with the W(110) surface disappears from the spectra and three photoemission peaks successively appear at ~2.02, ~2.11, and ~2.40 eV. The spectrum modification indicates that these peaks are caused by the excitation of plasma oscillations in quasi-2D Cs clusters and excitation of the interface Cs–W and surface Cs plasmons.

The experiment was carried out *in situ* under high vacuum $P < 1 \times 10^{-10}$ torr at room temperature. Atomically pure cesium was deposited on the W(110) surface from the standard source. The Cs flow intensity was

determined by the method used in [12, 13]. This method allowed the estimation of the cesium dose D_{Cs} deposited on the sample in a given time. The electronic properties were studied by threshold photoemission spectroscopy [10–13]. The photoemission was excited by the *s*- and *p*-polarized light incident on the sample at an angle of 45°. The surface photoemission spectra were measured as a ratio $I_p(h\nu)/I_s(h\nu)$, where $I_p(h\nu)$ and $I_s(h\nu)$ are the photoemission current spectra excited by the *p*- and *s*-polarized light, respectively. The photoemission currents were measured in the range 10^{-8}–10^{-13} A. The error of measuring the I_p/I_s spectra did not exceed 10%.

Figure 1 shows the surface photoemission spectra recorded in the step-by-step regime for $\Theta = 0.5$ ML (ML = monolayer) and the dynamic regime for different Cs doses deposited on the W(110) surface. The coverage $\Theta = 5.5 \times 10^{14}$ atom/cm^2 is taken as a monolayer ($\Theta = 1$ ML) for the Cs coatings on metal surfaces [14]. In the commonly accepted step-by-step regime, the source is switched off after the deposition of a certain dose, whereupon the spectra are recorded. The Cs-coverage degree at the W surface can be determined only for $\Theta < 0.95$ ML (the cesium attachment coefficient is unity in this case). For coverages $\Theta > 0.95$ ML, the Cs attachment coefficient drops drastically (the corresponding value was not determined), for which reason the higher coverages necessitate the use of special adsorption regimes, e.g., low-temperature adsorption [14]. We have proposed to use a continuous, so-called dynamic, adsorption regime, for which the Cs vapor pressure prevents the Cs desorption from the surface in the course of deposition. In this regime, the spectra for doses $D_{Cs} > 5.5 \times 10^{14}$ atom/cm^2 are recorded directly during the cesium deposition. The recording time provides an error of ~10% in the dose determination.

In the spectra presented in Fig. 1, three photoemission maxima **A**, **B**, and $\mathbf{P}_1$ at energies, respectively, 1.78, 2.02, and 2.35 eV appear with increasing Cs dose. Peak **A** (Fig. 1a) is observed only in the step-by-step regime and corresponds to the photoemission from the surface Cs band, which was studied previously in [10]. This peak is due to the local interaction of the Cs adatoms with the tungsten surface. The peak intensity drops sharply with increasing dose, and it eventually disappears from the spectrum (Figs. 1b, 1c). Simultaneously with the modification of peak **A**, a new broad ($\Delta E \sim 0.3$ eV) peak **B** appears in the spectrum (Fig. 1b) and dominates up to $D_{Cs} \approx 6.5 \times 10^{14}$ atom/cm^2 (Fig. 1c). The peak energy does not change with dose. A further increase in the dose results in the disappearance of peak **B** (Fig. 2b). Such a behavior enables one to conclude that peak **B** is due to the excitation of plasma oscillations in two-dimensional cesium clusters. The fact that peak **B** appears in the spectrum at approximately the same coverages at which the intensity of peak **A** decreases sharply and then disappears counts in favor of this interpretation. Therefore, the

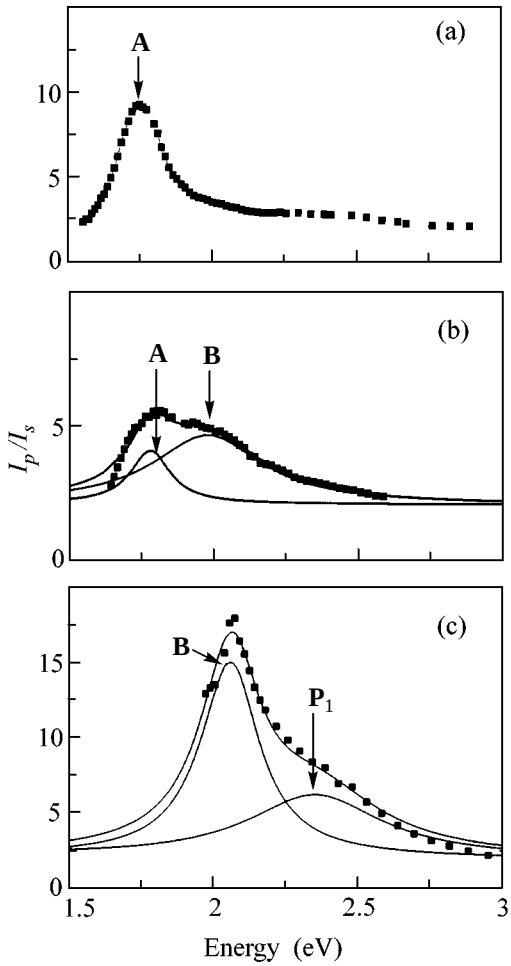

Fig. 1. Surface photoemission spectra I_p/I_s for different Cs doses. (a) Step-by-step adsorption regime: 4.2×10^{14} atom/cm^2 ($\Theta = 0.8$ ML); (b, c) Dynamic adsorption regime: (b) 5.8×10^{14} and (c) 6.5×10^{14} atom/cm^2.

appearance of peak **B** may be explained by the formation of close-packed 2D clusters from the individual Cs adatoms, which locally interacted with the W(110) surface at lower coverages. The clusters are formed because at a certain coverage degree the dipole–dipole repulsion between the polarized Cs adatoms changes to attraction as a result of the depolarization effects. The fact that the position of peak **B** does not change, while its intensity increases in a certain range of doses, indicates that the area occupied by the Cs clusters increases and that the density of Cs atoms in the clusters is virtually constant. For a coverage slightly higher than one monolayer, the interaction between the clusters becomes comparable with the interaction between adatoms in the cluster, resulting in the destruction of the Cs clusters and formation of a continuous coating.

To elucidate the origin of peak $\mathbf{P}_1$, one should trace the evolution of the spectra shown in Figs. 1 and 2. Peak $\mathbf{P}_1$ appears at $D_{Cs} = 6.5 \times 10^{14}$ atom/cm^2 and has a low intensity up to the critical dose $D_{Cs} = (9–10) \times$

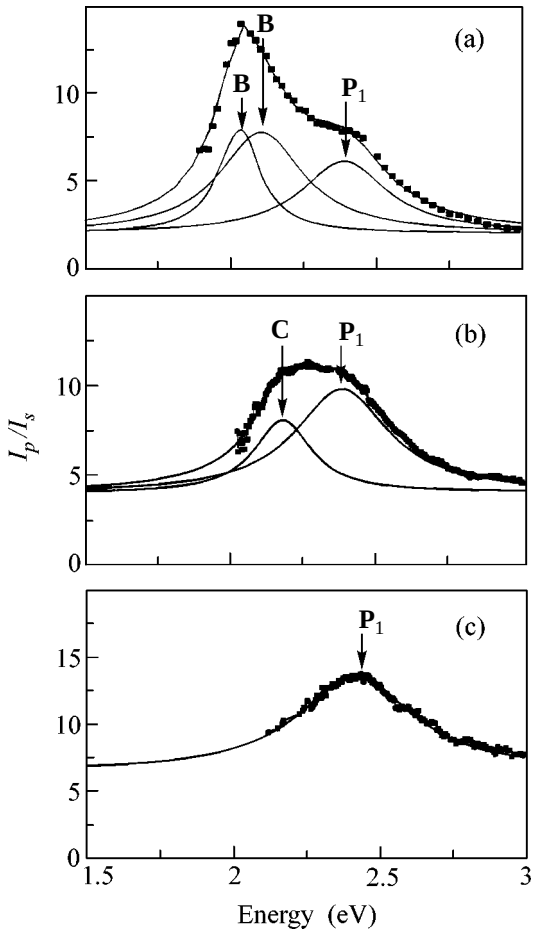

Fig. 2. Surface photoemission spectra I_p/I_s for different Cs doses. Dynamic adsorption regime: (a) 8.0×10^{14}, (b) 1.1×10^{15}, and (c) 1.3×10^{15} atom/cm^2.

10^{14} atom/cm^2, after which its intensity increases jumpwise (Fig. 2b) and then remains virtually unchanged (Figs. 2b, 2c). Note that, contrary to peak **B**, the position of peak $\mathbf{P}_1$ is not fixed. As the dose increases, it shifts to higher energies from 2.35 to 2.44 eV, apparently, because of the increase in electron density in the Cs coating. The observed values are close to the energies obtained previously for a surface Cs plasmon on the Si and Al substrates at Cs coverages higher than 2 ML [1, 3, 9]. Therefore, the energy of a surface Cs plasmon is influenced by both the nature of substrate and the adatom concentration. An important feature in the behavior of the Cs plasmon peak is that its intensity increases jumpwise at a dose corresponding to the disappearance of the Cs clusters. It is conceivable that this phenomenon is due to the formation of a continuous cesium coating. The presence of a surface Cs plasmon at smaller doses, at which the Cs clusters are as yet not observed, may be due to the percolation effect.

Peak **C** is observed in a rather narrow range of doses $D_{Cs} = (8–13) \times 10^{14}$ atom/cm^2 (Figs. 2a, 2b). It is seen that this peak undergoes an energy shift analogous to that of the Cs plasmon peak, indicating that the electron density increases. One can see a certain correlation between the parameters and behavior of peak **C** and peak $\mathbf{P}_1$ of the surface Cs plasmon. We assume that peak **C** is due to the electron density node at the interface between the substrate and Cs coating, i.e., to the interface Cs–W plasmons. Peak **C** disappears at large adsorption doses, likely, because the metastable Cs coating of 2–3 ML screens the plasmon excitation at the Cs–W interface.

Thus, it has been found that, before the formation of a continuous Cs coating, the Cs adsorption proceeds through the step of formation of the Cs clusters of a certain size. It is established that the electron density profile in the Cs/W system has at least two nodes with large amplitude that is sufficient for the excitation of a surface Cs plasmon and an interface Cs–W plasmon. One can conclude on the basis of the data obtained that threshold photoemission spectroscopy is an effective tool for studying the 2D plasma modes.

This work was supported by the Russian Foundation for Basic Research (project no. 01-02-16802) and the program of the Ministry of Industry, Science, and Technologies of the Russian Federation (project no. 1-107).

REFERENCES

1. A. Liebsch, G. Hincelin, and T. Lopez-Rios, Phys. Rev. B **41**, 10463 (1990).
2. K.-D. Tsuei, E. W. Plummer, A. Liebsch, *et al.*, Phys. Rev. Lett. **64**, 44 (1990).
3. K.-D. Tsuei, E. W. Plummer, *et al.*, Surf. Sci. **247**, 302 (1991).
4. S. R. Barman, K. Horn, P. Haberle, *et al.*, Phys. Rev. B **57**, 6662 (1998).
5. D. Claesson, S.-A. Lindgren, L. Wallden, *et al.*, Phys. Rev. B **82**, 1740 (1999).
6. A. Liebsch, *Electronic Excitations at Metal Surfaces* (Plenum, New York, 1997).
7. U. del Pennino, R. Compano, B. Salvarani, *et al.*, Surf. Sci. **409**, 258 (1998).
8. O. E. Tereshchenko, V. L. Al'perovich, A. S. Terekhov, A. N. Litvinov, *et al.*, Pis'ma Zh. Éksp. Teor. Fiz. **70**, 537 (1999) [JETP Lett. **70**, 550 (1999)].
9. Y.-C. Chao, L. S. O. Iohasson, and R. I. G. Uhrberg, Phys. Rev. B **56**, 15446 (1997).
10. G. V. Benemanskaya and M. N. Lapushkin, Pis'ma Zh. Éksp. Teor. Fiz. **45**, 423 (1987) [JETP Lett. **45**, 540 (1987)].
11. A. Liebsh, G. V. Benemanskaya, and M. N. Lapushkin, Surf. Sci. **302**, 303 (1994).
12. G. V. Benemanskaya, D. V. Dianeka, and G. E. Frank-Kamenetskaya, Surf. Rev. Lett. **5**, 91 (1998).
13. G. V. Benemanskaya, V. P. Evtikhiev, and G. É. Frank-Kamenetskaya, Fiz. Tverd. Tela (St. Petersburg) **42**, 356 (2000) [Phys. Solid State **42**, 366 (2000)].
14. A. G. Fedorus and A. G. Naumovets, Surf. Sci. **21**, 426 (1970).

Translated by V. Sakun

JETP Letters, Vol. 74, No. 2, 2001, pp. 87–90. From Pis'ma v Zhurnal Éksperimental'noĭ i Teoreticheskoĭ Fiziki, Vol. 74, No. 2, 2001, pp. 92–95.

Two-Terminal Conductance of a Fractional Quantum Hall Edge[1]

V. V. Ponomarenko* and D. V. Averin

Department of Physics and Astronomy, SUNY, Stony Brook, NY 11794 USA

** On leave of absence from the Ioffe Physical Technical Institute, St. Petersburg, 194021 Russia*

Received June 13, 2001

We have found a solution to a model of tunneling between a multichannel Fermi liquid reservoir and an edge of the principal fractional quantum Hall liquid (FQHL) in the strong-coupling limit. The solution explains how the chiral edge propagation makes the universal two-terminal conductance of the FQHL fractionally quantized and different from that of a 1D Tomonaga–Luttinger liquid wire, where a similar model, but preserving the time reversal symmetry, predicts unsuppressed free-electron conductance. © *2001 MAIK "Nauka/Interperiodica"*.

PACS numbers: 71.10.Pm; 73.43.Jn

Low-energy transport through an incompressible quantum Hall liquid with gapped bulk excitations is carried by gapless edge modes [1, 2]. For principal fractional quantum Hall liquid (FQHL) of the filling factor $\nu = 1/\text{odd}$, these modes are described as a single branch of a chiral Luttinger liquid (χLL) [3]. In presence of the right and left chiral edges, the model of the FQHL transport [4] appears to be equivalent to that of a metallic phase of a 1D interacting electron gas [5] known as a Tomonaga–Luttinger liquid (TLL) [6, 7]. To describe the two-terminal transport experiments, the external reservoirs have to be added to the model [2, 8], so that the full transport process includes transformation of the reservoir electrons into the FQHL/TLL quasiparticles in the junctions. The transformation process makes the two-terminal conductance of both the TLL wire [9, 10] and the narrow FQHL junctions [11, 12] equal to the free-electron conductance σ_0. The standard experimental observation, however, is that the two-terminal FQHL conductance is equal to the Hall conductivity $\nu\sigma_0$ (see, e.g., [13]) but not σ_0, a fact that implies equilibration between the chemical potentials of the reservoirs and the outgoing edges [14]. This problem was recently studied [12, 15] for the junction modeled as a sequence of pointlike contacts between the edge and different channels of a multichannel Fermi liquid reservoir under an additional assumption [12, 15] of suppressed quantum interference between electron tunneling at different contacts. The purpose of this work is to construct a quantum solution of the model of tunneling between a multichannel Fermi liquid reservoir and the χLL edge. Our solution shows how both the standard fractional quantization of the FQHL conductance and the free-electron conductance can be obtained not from the additional assumption of decoherence but from the appropriate account of different patterns of quantum interference depending on the junction structure. The solution explains (in obvious agreement with experiment) the difference between the universal two-terminal conductance $\nu\sigma_0$ of the 1D FQHL edge and conductance σ_0 of the 1D TLL wire.

The model we consider represents n scattering channels of the spinless FL reservoir as free chiral fermions. Tunneling from the channels (labeled by $j = 1, \ldots, n$) into the edge (labeled by 0) is assumed to be localized on the scale of magnetic length at the points x_j along the edge, where $x_j < x_i$ for $1 \le i < j \le n$. It is described by a tunnel Lagrangian:

$$\mathcal{L}_{\text{tunn}} = \sum_{j=1}^{n} [U_j \psi_0^+(x_j, t)\psi_j(x_j, t) + \text{h.c.}], \qquad (1)$$

where U_j are chosen real and positive. Bosonization expresses the operators of free electrons $\psi_j(x, t) = (2\pi\alpha)^{-1/2}\xi_j e^{i\phi_j(x,t)}$ in the reservoir channels and the operator of electrons propagating along the edge $\psi_0 = (2\pi\alpha)^{-1/2}\xi_0 e^{i\phi_0(x,t)/\sqrt{\nu}}$ through their associate bosonic fields ϕ_l, the Majorana fermions ξ_l accounting for their mutual statistics, and a common factor $1/\alpha$ denoting momentum cutoff of the edge excitations. Since the spatial dynamics of the reservoir channels ($l > 0$) does not affect the tunneling currents, velocities of these channels are irrelevant, and we take them equal to the velocity v of the edge excitations. Free dynamics of the bosonic fields is governed then by the Lagrangian $\mathcal{L}_O = \sum_{l=0}^{n} (\phi_l \hat{K}^{-1} \phi_l)/2$, where the differential operator is

$$\hat{K}^{-1}\phi_l(x, t) = \frac{1}{2\pi}\partial_x(\partial_t + v\partial_x)\phi_l(x, t). \qquad (2)$$

The full Lagrangian $\mathcal{L} = \mathcal{L}_O + \mathcal{L}_\xi + \mathcal{L}_{\text{tunn}}$ also includes an additional kinematic part $\mathcal{L}_\xi = (1/4)\xi\partial_t\xi$ describing a pure statistical dynamics of the Majorana fermions

[1] This article was submitted by the authors in English.

(time-ordering). A finite voltage applied to the reservoir is accounted for by the opposite-sign shift μ of the electrochemical potential of the edge, which can be introduced by an additional nonequilibrium part of the Lagrangian $\mathcal{L}_V = \sqrt{\nu}/2\pi \int dx\, \phi_0(x, t)\partial_x V(x)$, where $V(x)$ depends on the modeled physics and in our case can be chosen as follows. In the absence of tunneling, when the evolution of the edge is governed by the retarded Green's function $K(x, t) = \pi\theta(t)\,\mathrm{sgn}(x - vt)$ of the operator $\hat{K}^{-1}$ in Eq. (2), the Lagrangian $\mathcal{L}_V$ shifts ϕ_0 and results in its nonzero average

$$\bar{\phi}_0(x, t) = -(\sqrt{\nu}/2\pi)\int dt' \int dy K(x - y, t - t')\partial_y V(y)$$

satisfying

$$-\partial_t \bar{\phi}_0 = v\partial_x \bar{\phi}_0 + \sqrt{\nu}\left[V(x) - \frac{1}{2}\sum_{\pm} V(\pm\infty)\right]. \qquad (3)$$

This equation shows that $\mathcal{L}_V$ describes two physical processes. The first is current injection into the edge due to $V(x)$: $\partial_t \rho_0 + \partial_x j_0 = -v\partial V(x)/2\pi$ (chiral anomaly), where the chiral edge density $\rho_0 = \sqrt{\nu}\,\partial_x \phi_0/2\pi$ is related to the current as $j_0 = v\rho_0$. The second is an additional shift of electrochemical potential of the edge equal to $[V(x) - \sum_{\pm} V(\pm\infty)/2]$. By choosing $V(x) = -\mu\,\mathrm{sgn}(x - y_X)$, with $y_X \longrightarrow \infty$, we reduce the whole effect to the shift of the edge potential relative to the reservoir by, in general, time-dependent potential $\mu(t)$ without producing any additional edge current at $x < y_X$. With this choice, in presence of tunneling, the edge current caused by $\mathcal{L}_V$ is just the opposite of the total tunneling current.

We start by considering the strong coupling limit of a one-point contact ($n = 1$). The tunneling Lagrangian reduces to

$$\mathcal{L}_{\mathrm{tunn}} = U_1/2\pi\alpha \cos(\phi_0(x_1, t)/\sqrt{\nu} - \phi_1),$$

and in the limit $U_1 \longrightarrow \infty$ fixes the argument of the cos-term at one of the cosine maxima, e.g., $\phi_0(x_1, t)/\sqrt{\nu} = \phi_1(x_1, t)$. Then, introducing the vector $\phi(x, t) = [\phi_0, \phi_1]^T$, one can find its two-component average $\bar{\phi}(x, t) \equiv \langle\phi(x, t)\rangle$ as

$$\bar{\phi}(x, t) = -i\frac{\sqrt{\nu}}{\pi}\int \frac{d\omega}{\omega} e^{-i\omega t} g(x, \omega)\mu(\omega), \qquad (4)$$

where $-2\pi i g/\omega$ is the first column of the (2×2) matrix Green's function. The two components $g_{0,1}(x)$ of the function g do not depend on $y_X \longrightarrow \infty$ for $x < y_X$, and satisfy the homogeneous differential equation (2) at $x \neq x_1$, and therefore can be written as $g_{0,1} = a_{0,1} + b_{0,1}\exp[-i\omega x/v]$. The coefficients a and b take different values $a_{0,1}^{\wp}$, $b_{0,1}^{\wp}$ for x smaller and larger than x_1 ($\wp$ denotes $<$ or $>$, respectively). They are related among themselves by four conditions: continuity of g_0 and g_1; continuity of the current flow $\sqrt{\nu}b_0^{<} + b_1^{<} = \sqrt{\nu}b_0^{>} + b_1^{>}$; and maximum of the tunneling term $g_0(x_1) - \sqrt{\nu}g_1(x_1) = 0$. The solution g is a linear combination of the four independent functions

$$f_c^{-} = [\sqrt{\nu}, 1]^T, \quad f_b^{-} = e^{i\omega x/v} f_c^{-},$$
$$f_1^{\langle,\rangle} = \theta(\mp(x - x_1))(e^{i\omega x/v} - 1)[1, -\sqrt{\nu}]^T,$$

which are constructed to satisfy these conditions. Since propagation of tunneling electrons are governed by the free matrix Green's function which is diagonal and equal to $K \times 1$, where

$$K(x - y, \omega) = -\frac{2\pi i}{\omega}\left[\frac{1}{2} + \theta(x - y)\left(e^{\frac{-i\omega(x-y)}{v}} - 1\right)\right], \qquad (5)$$

we can find more restrictions on the coefficients: $b_{0,1}^{<} = 0$, $a_1^{<} = -a_1^{>}$, $a_0^{\wp} = 1/2 - a_1^{\wp}/\sqrt{\nu}$. They uniquely specify $g(x, \omega) = [\sqrt{\nu} f_c^{-}/2 - f^{>}]/(1 + \nu)$.

The currents follow then from Eq. (4) as

$$j_1(x, t) = -j_0 = \frac{2\nu}{1 + \nu}\theta(x - x_1)\sigma_0 \mu(t - [x - x_1]/v).$$

The tunneling conductance is equal to $G_1 = 2\nu\sigma_0/(1 + \nu)$ in agreement with the result of application [12] of the chirally symmetric solution developed for a point scatterer in TLL [5].

To extend this approach to the multichannel contact, we notice that, although the statistical factors $\pm\xi_0\xi_j$ attributed to annihilation/creation of electrons in the jth channel can not be ignored for more than one j involved, they can be replaced [7] by the exponents $\exp\{\pm i\sqrt{\gamma}\eta_j\}$ of the zero-energy bosonic fields satisfying $[\eta_i, \eta_j] = i\pi\,\mathrm{sgn}(i - j)$ with an odd integer γ that specifies a phase branch of the fermionic statistics. These fields can be readily constructed from the standard creation and annihilation operators of $n - 1$ independent zero-energy bosonic modes. Since any nonvanishing term of the perturbative expansion in $\mathcal{L}_{\mathrm{tunn}}$ contains $\pm$ exponents in pairs, a proper interchange cancels all exponents and leaves only the statistical sign, the same one would get directly from the Majorana fermions. The substitution of the Majorana fermions by

bosonic modes transforms $\mathcal{L}_{\text{tunn}}$ into

$$\mathcal{L}_{\text{tunn}} \equiv \sum_{j=1}^{n} \mathcal{L}_j = \sum \frac{U_j}{2\pi\alpha} \cos\left\{ \frac{\phi_0(x_1, t)}{\sqrt{\nu}} - \phi_j - \sqrt{\gamma}\eta_j \right\}. \quad (6)$$

Equation (6) possesses the initial commutation symmetry between the different parts of the tunneling Lagrangian, since permutation of $\mathcal{L}_i$ and $\mathcal{L}_j$ results in the appearance of the phase factors $\exp\{\pm i\pi \operatorname{sgn}(i - j)(\gamma - 1/\nu)\}$ equal to 1 for any odd γ. As all U_j in Eq. (6) tend to ∞, all the cosine arguments are simultaneously fixed. One can notice, however, that this strong-coupling limit depends on the choice of γ. Indeed, in this limit, each $\mathcal{L}_j$ can be approximated as $-\bar{U}_j/(2\pi\alpha)(\phi_0(x_1, t)/\sqrt{\nu} - \phi_j - \sqrt{\gamma}\eta_j)^2$ with sufficiently large $\bar{U}_j$, the form that clearly puts γ (and not exponent of γ) in the commutator between $\mathcal{L}_i$ and $\mathcal{L}_j$. Moreover, if $|x_i - x_j| \gg \alpha$ for all i, j, there is only one choice of γ, $\gamma = 1/\nu$, which does not violate the commutativity of limiting forms of $\mathcal{L}_j$. Relevance of the different choices of γ in the strong-coupling limits can be understood from their effect on the energy of the system [16]. Here, however, we chose a more heuristic physical argument. We prove that only the symmetric strong-coupling limit can be relevant, since all other choices of γ lead to solutions which do not satisfy the condition of causality.

To show this, we calculate the current flow in the strong-coupling limit of Eq. (6) keeping γ as a free parameter. The calculation generalizes the one for the single-point contact. The average $\bar{\phi}(x, t)$ in Eq. (4) becomes the $(n + 1)$-component vector $\langle[\phi_0, \ldots, \phi_j + \sqrt{\gamma}\eta_j, \ldots]^T\rangle$, and $-2\pi i g/\omega$ is the first column of the corresponding $(n + 1) \times (n + 1)$ matrix Green's function. The coefficients a_j, b_j, $j = 1 - n$ take different values $a_j^{\wp}$, $b_j^{\wp}$ for x smaller and larger than x_j, where $\wp$ denotes $<$ and $>$ as before. The edge channel coefficients a_0, b_0 take $(n + 1)$ different values, changing at each tunneling contact $x = x_j$ in a way that relates them to a_j, b_j by the four matching conditions derived above for the single-contact case. We denote by $a_0^{\wp}$ and $b_0^{\wp}$ their values for x smaller than x_n ($\wp = <$) and larger than x_1 ($\wp = >$). A set of $2(n + 1)$ independent vector functions satisfying all these conditions may be chosen as

$$f_c^- = [\sqrt{\nu}, 1, 1, 1, \ldots]^T, \quad f_b^- = e^{i\omega x/v} f_c^-,$$

$$f_j = (e^{i\omega x/v} - e^{i\omega x_j/v}) e_j,$$

$$f_j^> = (e_0/\sqrt{\nu} - e_j)\theta(x - x_j)(e^{i\omega(x - x_j)/v} - 1) + \sum_{l=1}^{j-1} e_l (e^{i\omega(x_l - x_j)/v} - 1)/\nu,$$

where a vector e_l has the only nonzero lth component equal to 1. Since all coefficients $b_l^<$ of the function g are zero, it can be expanded in this basis as

$$g = s_c f_c^- + \sum_{j=1}^{n} s_j f_j^> \quad (7)$$

with $(n + 1)$ unknown coefficients s_l. The nonzero s_j lead to finite jumps in a_j and b_j at $x = x_j$ and, therefore, to the nonvanishing $b_j^> = -s_j e^{-i\omega x_j/v}$. Then, in accordance with Eq. (4), the reservoir channel currents arising at x_j can be found as $j_j(\omega, x) = 2\sqrt{\nu}\,\mu\sigma_0 b_j^> \theta(x - x_j) e^{i\omega x/v}$. Jumps in the coefficients a_j and b_j are caused by the charge tunneling at the contact points x_j, with further propagation of charge governed by the free retarded Green's function. This means that this function determines both the continuous parts of the a, b coefficients and the relations between their discontinuous parts and the coefficients s_j. The Green's function is a $(n + 1) \times (n + 1)$ matrix and can be written as $K \times \mathbf{1} - \gamma\pi i\mathbf{C}/\omega$, where $\mathbf{C}$ is an antisymmetric matrix with all elements above the diagonal, except the first row, equal to 1. From this form, one can find that $b_l^< = 0$ [a fact already used in Eq. (7)] and that the coefficients a_l are related to s_j. In particular, $a_0^< = 1/2 + \sum_{p=1}^{n} s_p/2\sqrt{\nu}$, $a_j^< = -s_j/2 + \gamma/2 \sum_{p \neq j} \operatorname{sgn}(j - p) s_p$. From comparison of these relations to those obtained by direct substitution of the $\mathbf{f}$ vectors into Eq. (7), we get n equations:

$$\frac{\sqrt{\nu}}{1 + \nu} + s_n = -\frac{1 - \gamma\nu}{1 + \nu} \sum_{1}^{n-1} s_i,$$

$$s_p = s_n + \sum_{j=p+1}^{n} \frac{2 s_j}{(1 + \gamma)} [(1 - e^{i\omega(x_p - x_j)/v})/\nu - \gamma], \quad (8)$$

where $p = 1 - (n - 1)$. Equations (8) allow us to determine all unknown coefficients s_j.

For the two-point contact, these equations reduce to

$$s_1 = \left(1 - \gamma + \frac{2}{\nu}[1 - e^{i\omega(x_1 - x_2)/v}]\right) \frac{s_2}{1 + \gamma},$$

$$s_2 = -\frac{\nu^{3/2}(1 + \gamma)}{2R}, \quad (9)$$

$$R \equiv 1 + \nu(1 - \gamma) + \frac{\nu^2}{2}(1 + \gamma^2) - (1 - \nu\gamma) e^{i\omega(x_1 - x_2)/v}.$$

The part of the denominator R proportional to $(1 - \nu\gamma)$ signals the appearance of an interference structure in the currents. Substituting $s_{1,2}$ from Eqs. (9) into $j_0(x, t) = -\int d\omega e^{-i\omega t}\sum_{1,2} j_j(\omega, x)$, one can see that, indeed, the time dependence of charge propagation along the edge exhibits multiple backscattering at x_2 and x_1. A charge wave started by the tunneling into the edge propagates from the point x_2 to x_1 with the velocity v and then instantly recoils back to x_2 from x_1 with a finite reflection coefficient proportional to $(1 - \nu\gamma)$. The formal possibility of the charge propagation with infinite velocity in the direction opposite to the edge chirality is a combined effect of x-independent solutions of the operator $\hat{K}^{-1}$ from Eq. (2) and the matching conditions at the tunneling points. However, the instant "counterpropagation" violates causality of the edge response to external perturbations and cannot appear in the final physical results. This makes $\gamma = 1/\nu$ the only relevant strong-coupling limit for $x_1 - x_2 \gg \alpha$ and clarifies the consequences of breaking the commutational symmetry of the initial tunneling Lagrangian for other choices of γ.

When the two tunneling points virtually coincide, $x_1 - x_2 \leq \alpha$, the Lagrangian symmetry is preserved for any γ. To make a physical choice of γ in this case, we look at the tunneling conductance $G = \sigma_0 \dfrac{4\nu}{2 + \nu[1 + \gamma^2]}$ that follows from Eq. (9) at zero frequency. If $\gamma = 1$ (corresponding to the minimal phase of the fermionic statistics), then $G = G_1$. In the tunneling model (1) with $n = 2$, this value of conductance represents the situation when the chiral dynamics of the edge does not play any role, and the two reservoir channels are reduced to one tunneling mode. The choice of γ can also be confirmed by consideration of the tunneling energy [16], which for $x_1 \simeq x_2$ is minimized by the smallest γ consistent with the statistics of the tunneling operators. In particular, $\gamma = 0$ gives the strong tunneling conductance in the model of an impurity scatterer in TLL of two spin-degenerate channels with the spin coupling constant $g_s = 2$ and the charge constant $g_c = 1/(1/\nu + 1/2)$.

For spatially separated tunneling points, the symmetry-preserving solution with $\gamma = 1/\nu$ reproduces equilibration between the reservoir and the edge. To see this, we substitute $\gamma = 1/\nu$ into the first of Eqs. (8) and find that $s_n = -\sqrt{\nu}/(1 + \nu)$ for any n. This shows that the tunneling into the nth channel is described by the one-point tunneling conductance G_1 for all frequencies ω, since it cannot be affected by other contacts down the edge. The zero-frequency solution of the second of Eqs. (8) is $s_{p-1} = qs_p$, $p = 2–n$, with $q = (1 - \gamma)/(1 + \gamma)$ equal to $1 - G_1/\sigma_0\nu$ for $\gamma = 1/\nu$. It means that in the strong-coupling limit the tunneling current Δj out of the edge results in the $\Delta j/\sigma_0\nu$ drop of the edge chemical potential. The zero-frequency n point tunneling conductance follows from $b_0^> = \sum s_j/\sqrt{\nu} = s_n(1 + \nu)(1 - q^n)/2\sqrt{\nu}$ as $\sigma_0\nu(1 - q^n)$ and saturates at $\nu\sigma_0$, when $n \longrightarrow \infty$ and the outgoing edge is equilibrated with the reservoir.

In conclusion, we have found the strong-coupling solution of the model of tunneling between the multimode Fermi liquid reservoir and an edge of the principal FQHL. The solution depends on the choice of the statistical phase branch of different reservoir modes with the physically relevant choice of the phase preserving the initial commutation symmetry of the tunneling Lagrangian. The statistical phase accounts for an even number of fluxes absorbed/emitted by tunneling electrons. The results explain the difference between transport through a 1D FQHL edge and a TLL wire: the two-terminal universal conductance of the edge is renormalized by the flux attachment, while direct electron–electron interaction in the wire does not change its universal free-electron conductance.

This work was supported by the NSA and ARDA under ARO contract.

REFERENCES

1. B. I. Halperin, Phys. Rev. B **25**, 2185 (1982); P. Streda, J. Kucera, and A. H. MacDonald, Phys. Rev. Lett. **59**, 1973 (1987).
2. M. Buttiker, Phys. Rev. B **38**, 9375 (1988).
3. X. G. Wen, Phys. Rev. Lett. **64**, 2206 (1990); J. Frölich and T. Kerler, Nucl. Phys. B [FS] **354**, 369 (1991); M. Stone and M. P. A. Fisher, Int. J. Mod. Phys. B **8**, 2539 (1994); N. Nagaosa and M. Kohmoto, Phys. Rev. Lett. **75**, 4294 (1995).
4. X. G. Wen, Phys. Rev. B **44**, 5708 (1991); K. Moon, H. Yi, C. L. Kane, *et al.*, Phys. Rev. Lett. **71**, 4381 (1993).
5. C. L. Kane and M. P. A. Fisher, Phys. Rev. B **46**, 15233 (1992).
6. S. Tomonaga, Prog. Theor. Phys. **5**, 544 (1954).
7. F. D. M. Haldane, J. Phys. C **14**, 2585 (1981).
8. R. Landauer, Philos. Mag. **21**, 863 (1970).
9. S. Tarucha, T. Honda, and T. Saku, Solid State Commun. **94**, 413 (1995); R. de Picciotto, H. L. Stormer, A. Yacoby, *et al.*, Phys. Rev. Lett. **85**, 1730 (2000); A. Yacoby, H. L. Stormer, Ned S. Wingreen, *et al.*, Phys. Rev. Lett. **77**, 4612 (1996).
10. V. V. Ponomarenko, Phys. Rev. B **52**, R8666 (1995); **54**, 10328 (1996); D. L. Maslov and M. Stone, Phys. Rev. B **52**, R5539 (1995); I. Safi and H. J. Schulz, Phys. Rev. B **52**, R17040 (1995).
11. D. B. Chklovskiĭ and B. I. Halperin, Phys. Rev. B **57**, 3781 (1998).
12. C. Chamon and E. Fradkin, Phys. Rev. B **56**, 2012 (1997).
13. A. M. Chang, L. N. Pfeiffer, and K. W. West, Phys. Rev. Lett. **77**, 2538 (1996); A. M. Chang and J. E. Cunningham, Surf. Sci. **229**, 216 (1990).
14. X. G. Wen, Int. J. Mod. Phys. B **6**, 1711 (1992); A. Yu. Alekseev, V. V. Cheianov, and J. Fröhlich, Phys. Rev. B **54**, R17320 (1996).
15. C. L. Kane and M. P. A. Fisher, Phys. Rev. B **52**, 17393 (1995).
16. V. V. Ponomarenko and D. V. Averin, in preparation.

JETP Letters, Vol. 74, No. 2, 2001, pp. 91–95. Translated from Pis'ma v Zhurnal Éksperimental'noĭ i Teoreticheskoĭ Fiziki, Vol. 74, No. 2, 2001, pp. 96–100.

Ordered Orthorhombic Phases of Titanium Monoxide

A. I. Gusev

Institute of Solid-State Chemistry, Ural Division, Russian Academy of Sciences, ul. Pervomaĭskaya 91, Yekaterinburg, 620219 Russia

e-mail: gusev@ihim.uran.ru

Received June 14, 2001

Symmetry analysis is carried out for the ordered phases of cubic monoxide TiO_y with relative oxygen contents $y < 1$ and $y > 1$. It is established that a partially ordered orthorhombic phase (space group *Immm*)—a derivative of the orthorhombic $M_3X_2\square$ superstructure (at $y < 1.0$) or the inverse superstructure $M_2\blacksquare X_3$ (at $y > 1$)—may arise in TiO_y. The distribution of Ti and O atoms, oxygen vacancies □, and titanium vacancies ■ in unit cells of the orthorhombic ordered phases is determined. The phases are formed through the order–disorder transition channel along two rays of a non-Lifshitz star $\{\mathbf{k}_4\}$, and the ordering proceeds as a first-order phase transition. The distribution functions of Ti atoms over the sites of metallic and O atoms over the sites of nonmetallic sublattices are calculated for the orthorhombic superstructures of cubic titanium monoxide TiO_y. © *2001 MAIK "Nauka/Interperiodica".*

PACS numbers: 61.50.Ks; 64.70.Kb; 61.66.Fn

The phase diagram of the Ti–O system was found to contain from 19 to 27 different phases and compounds [1–3], the real existence of some of them not being established reliably. Titanium monoxide TiO_y with the basal cubic (type B_1) structure is the most interesting compound in the Ti–O system. TiO_y belongs to the group of strongly nonstoichiometric compounds [4]; it has a broad homogeneity interval from $TiO_{0.70}$ to $TiO_{1.26–1.28}$ and contains 10–15 at. % structural vacancies simultaneously in each of the titanium and oxygen sublattices [5–8]. The formulation of titanium monoxide as TiO_y does not carry information on the concentration of structural vacancies in the metallic and nonmetallic sublattices. For this reason, it would be more correct to represent the monoxide composition as $Ti_xO_z \equiv Ti_x\blacksquare_{1-x}O_z\square_{1-z} \equiv TiO_y$ ($y = z/x$; ■ and □ are the structural vacancies in the titanium and oxygen sublattice, respectively). Although the existence of TiO_y is beyond question, the data about the structure of its ordered phases are limited and contradictory in many cases.

The monoclinic [space group $C2/m$ ($A12m/1$)] superstructure $Ti_5\blacksquare O_5\square$ [8–11] is the only one whose existence was firmly established and repeatedly confirmed experimentally. A comprehensive description of its structure is given in [7]. The structure of the ordered tetragonal phase corresponding to the monoxide with nominal composition $TiO_{1.25}$ is also satisfactorily described [10]. As for the other ordered phases (orthorhombic $TiO_{0.7–0.9}$, $TiO_{1.19}$, and $Ti_{2.5}O_3$ and cubic $Ti_{22.5}O_{22.5}$), the relevant information amounts to deriving their symmetry from electron microscopy and diffraction data and to the speculations about their possible belonging to one of the three or four space groups [10, 12]. The authors of [10, 12] consider these phases as transient from the disordered cubic phase of TiO_y to the ordered monoclinic phase Ti_5O_5.

This study is devoted to the structural analysis of the orthorhombic ordered phases of titanium monoxide. According to [12], the orthorhombic phase of nominal composition $TiO_{1.20}$ is formed on the basis of a disordered cubic phase of TiO_y with structure $B1$ in the region $TiO_{1.00}$–$TiO_{1.50}$ and belongs to the space group *Immm*, *Imm*2, or *I*222. The true composition of the monoxide is unknown, because the data on the concentration of structural vacancies in the titanium and oxygen sublattices are not reported in [12]. Moreover, $TiO_{1.28}$, and not $TiO_{1.50}$, is at the upper boundary of homogeneity interval of cubic monoxide TiO_y. It is assumed in [12] that, apart from one vacancy, a unit cell contains six titanium atoms and five oxygen atoms. However, there is no way to orderly arrange an odd number of atoms over the sites of the orthorhombic unit cell, because there are no positions with multiplicity 1 (the lowest site multiplicity is 2). In [8, 10], the orthorhombic superstructure with space group *Immm* or *I*222 appeared in the region $TiO_{0.7}$–$TiO_{0.9}$ (the real composition of the monoxides was unknown). It was assumed in [10] that the authors of [8, 10, 12] dealt with the same orthorhombic phase, in which (depending on the oxygen content in TiO_y) the structural vacancies in the titanium sublattice or the structural vacancies in the oxygen sublattice were randomly distributed over the lattice sites, while the structural vacancies of the other sublattice were partially ordered.

0021-3640/01/7402-0091$21.00 © 2001 MAIK "Nauka/Interperiodica"

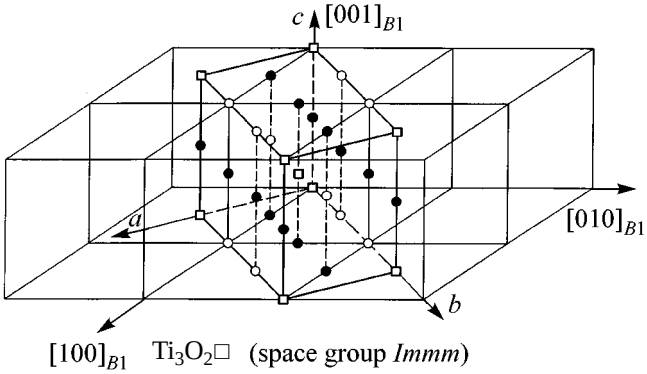

Fig. 1. Unit cell of the orthorhombic (space group *Immm*) $Ti_3O_2\square$ superstructure in the basal lattice of titanium monoxide Ti_xO_z ($y \equiv z/x < 1$) with structure *B*1: ● are the titanium sites randomly (with probability *x*) occupied by the Ti atoms; ○ are the oxygen 4(*g*) positions fully occupied by the O atoms; □ are the oxygen 2(*a*) positions vacant with probability $1 - n_{1(\bigcirc)}$ or (what is the same) occupied by the oxygen atoms with probability $n_{1(\bigcirc)} = z - 2\eta_4^{(\bigcirc)}/3 < 1$. The long-range order parameter can vary within $3(1 - z) \geq \eta_4^{(\bigcirc)} \geq 0$. The oxygen vacancies are located in every third $(110)_{B1}$ plane of the basal cubic lattice; the sites of these planes are randomly occupied by the oxygen vacancies.

Symmetry analysis carried out earlier in [4, 13] has shown that all the known superstructures of strongly nonstoichiometric compounds MX_y having structure *B*1 can be formulated as $M_{2t}X_{2t-1}\square$ (t = 1, 1.5, 2, 3, and 4). According to [14–16], only the $M_{2t}X_{2t-1}\square$ superstructures with t = 1, 1.5, and 3, i.e., $M_2X\square$ (space groups $R\bar{3}m$, $Fd\bar{3}m$, and $I4_1/amd$), $M_3X_2\square$ (space groups *Immm*, *P*2, and $C222_1$), and $M_6X_5\square$ (space groups *C*2, *C*2/*m*, and $P3_1$), are thermodynamically stable in the nonstoichiometric MX_y compounds containing vacancies in the nonmetallic sublattice. All the above-mentioned superstructures; their inverse superstructures $M\blacksquare X_2$, $M_2\blacksquare X_3$, and $M_5\blacksquare X_6$ with the ordered metallic vacancies; and the superstructures $M_5\blacksquare X_5\square$ and $M_2\blacksquare X_2\square$ with simultaneous vacancy ordering in both sublattices can, in principle, arise in the strongly nonstoichiometric compounds containing vacancies in both sublattices. The type of superstructure in a particular nonstoichiometric compound depends primarily on the width of the homogeneity interval of this compound. For example, superstructures of the $M_2X\square$ and $M\blacksquare X_2$ types cannot form in TiO_y, because they lie far beyond the homogeneity region of the TiO_y monoxide. Superstructures of the $M_6X_5\square$ and $M_5\blacksquare X_6$ types also cannot arise because, for the atom-to-vacancy ratio of 5/1 in the ordering sublattice, the concentration of vacancies of another sort in TiO_y approaches 10 at. %, i.e., is large to an extent that the ordering must occur in both sublattices. The $M_2\blacksquare X_2\square$ superstructure contains 33 at. % of vacancies in each sublattice, so that it also cannot form in TiO_y, because the concentration of structural vacancies in each sublattice of the equiatomic TiO monoxide does not exceed 17 at. % [5–7].

The stoichiometric composition of the M_3X_2 superstructure ($M_3X_2\square$) is closest to the lower boundary of the homogeneity interval of titanium monoxide $TiO_{0.70} \equiv Ti_{0.97}O_{0.68}$. The orthorhombic structure of this composition belongs to the space group *Immm*. It is formed through the order–disorder phase-transition channel along two rays $\mathbf{k}_4^{(1)} = (\mathbf{b}_1 + \mathbf{b}_2 + 2\mathbf{b}_3)/3$ and $\mathbf{k}_4^{(1)} = -\mathbf{k}_4^{(1)}$ of a non-Lifshitz star $\{\mathbf{k}_4\}$ with running parameter $\mu_4 = 1/3$ (the wave-vector stars $\{\mathbf{k}_s\}$ in the first Brillouin zone of a fcc crystal and the rays $\mathbf{k}_s^{(j)}$ of these stars are numbered according to [4, 16]). In the coordinates of the basal cubic structure, the translation vectors of a unit cell of orthorhombic (space group *Immm*) superstructure are **a** = {1/2, –1/2, 0}, **b** = {3/2, 3/2, 0}, and **c** = {0, 0, 1}.

Knowing the transition channel, one can determine the distribution function over the sites of oxygen sublattice for the O atoms in the orthorhombic superstructure $Ti_3O_2\square$ (t = 1.5) of the Ti_xO_z monoxide. The calculated distribution function has the form

$$n_{\bigcirc}(x_I, y_I, z_I) = z - (2\eta_4^{(\bigcirc)}/3)\{\cos[4\pi(x_I + y_I)/3]\}, \quad (1)$$

where $\eta_4^{(\bigcirc)}$ is the long-range order parameter corresponding to the $\{\mathbf{k}_4\}$ star. The maximal value of this parameter depends on the composition of the Ti_xO_z monoxide. For the ordered oxygen sublattice, one has for $1 > y \equiv z/x > (2t - 1)/2t$

$$\eta_4^{(\bigcirc)\max}(z) = 2t(1 - z) \equiv 3(1 - z), \quad t = 1.5. \quad (2)$$

Therefore, even at the lower boundary of the homogeneity interval of TiO_y monoxide (y = 0.70 and z = 0.68), the maximal value of the long-range order parameter in the ordered phase cannot exceed 0.96, and it does not exceed 0.59 for the $TiO_{0.90} \equiv Ti_{0.895}O_{0.805}$ monoxide.

The unit cell of the ordered orthorhombic (space group *Immm*) phase of a TiO_y monoxide with $y < 1$ is shown in Fig. 1. At the sites of the oxygen sublattice, the distribution function in Eq. (1) takes either of two values: $n_{1(\bigcirc)} = z - 2\eta_4^{(\bigcirc)}/3$ at the 2(*a*) positions and $n_{2(\bigcirc)} = z + \eta_4^{(\bigcirc)}/3$ at the 4(*g*) positions. One can readily verify that, for $1 > z > (2t - 1)/2t$, the $n_{2(\bigcirc)}$ value is always equal to unity, while $z \geq n_{1(\bigcirc)} \geq 3z - 2$ and is always smaller than unity. This implies that the oxygen atoms in the ordered orthorhombic phase of the TiO_y ($y < 1$) monoxide occupy all 4(*g*) positions, whereas the 2(*a*) positions are vacant with probability $P = 1 - n_{1(\bigcirc)}$ [or, what is the same, randomly occupied by the O atoms with probability $n_{1(\bigcirc)}$]. In the orthorhombic superstructure $Ti_3O_2\square$ of the TiO_y ($y < 1$) monoxide, the oxygen vacancies are

located in every third $(110)_{B1}$ plane of the basal cubic structure and randomly distributed in these planes (Fig. 1).

One should distinguish between the ordered orthorhombic phase $Ti_3O_2\square$ and the hexagonal (space group $P6/mmm$) phase of $TiO_{0.5}$ (or Ti_3O_2) [17], because the latter is not an ordered phase of the cubic monoxide TiO_y. Note that the stoichiometric $Ti_3O_2\square$ composition of the ordered orthorhombic phase does not lie within the homogeneity interval of the cubic titanium monoxide and, therefore, does not exist. Only a partially ordered orthorhombic phase of the $Ti_3O_2\square$ type is formed. An interesting case of ordering in the orthorhombic phase is provided by the ordering of the $Ti_3O_2\square$ type in the $TiO_{0.95}$ ($Ti_{0.877}O_{0.833}$) monoxide. If the long-range order parameter in $Ti_{0.877}O_{0.833}$ equals 0.5, then the O atoms and the oxygen vacancies $\square$ occupy the 2(a) positions with the same probability 0.5, and the composition of the partially ordered monoxide can be written as $(Ti_{0.877}\blacksquare_{0.123})_6O_5\square$. Compositionally, this resembles a superstructure of the $M_6X_5\square$ type, although it is a particular case of the $Ti_3O_2\square$ superstructure. The X-ray diffraction patterns of the ordered monoxides confirm these conclusions.

Figure 2 shows the calculated X-ray patterns of the $Ti_{0.968}O_{0.678}$ ($TiO_{0.70}$) and $Ti_{0.877}O_{0.833}$ ($TiO_{0.95}$) monoxides with the orthorhombic (space group *Immm*) ordering of the $Ti_3O_2\square$ type; the long-range order parameter is 0.966 and 0.50, respectively. In the X-ray pattern of the ordered $Ti_{0.877}O_{0.833}$ monoxide, whose composition can be written as $(Ti_{0.877}\blacksquare_{0.123})_6O_5\square$, the superstructure reflections are observed only for the rhombic phase; the reflections with $2\theta = 18.4°$, 20.9°, and other angles corresponding to the monoclinic or trigonal superstructures of the $M_6X_5\square$ type are absent.

Let us now consider the orthorhombic superstructure $M_2\blacksquare X_3$ with ordered metallic vacancies and randomly distributed nonmetallic vacancies. In TiO_y, such a structure can arise if $y > 1$. The ordered orthorhombic phase $Ti_2\blacksquare O_3$ of stoichiometric composition lies beyond the homogeneity region of the cubic TiO_y monoxide, but it is closest to the upper boundary of the homogeneity interval. The ordered phase $Ti_2\blacksquare O_3$ should be distinguished from the trigonal phase Ti_2O_3, because the latter is not an ordered phase of the TiO_y monoxide. The structural order–disorder phase-transition channel TiO_y ($y > 1$) $\rightleftharpoons$ $Ti_2\blacksquare O_3$ is the same as in the case of the TiO_y ($y < 1$) $\rightleftharpoons$ $Ti_3O_2\square$ transition.

The distribution function of Ti atoms over the sites of the titanium sublattice in the orthorhombic $Ti_2\blacksquare O_3$ superstructure ($Ti_{2t-1}\blacksquare O_{2t}$ with $t = 1.5$) of the Ti_xO_z monoxide has the form

$$n_{\mathrm{Ti}}(x_\mathrm{I}, y_\mathrm{I}, z_\mathrm{I}) = x - (2\eta_4^{(\mathrm{Ti})}/3)\{\cos[4\pi(x_\mathrm{I} + y_\mathrm{I})/3]\}. \quad (3)$$

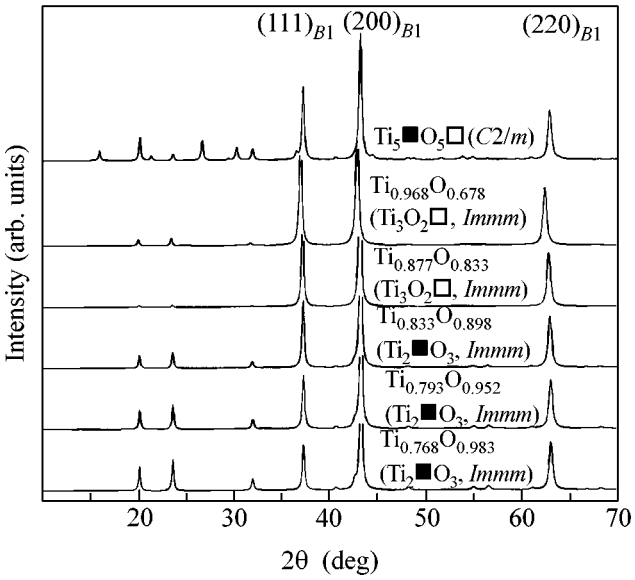

Fig. 2. X-ray diffraction patterns of the $Ti_{0.968}O_{0.678}$ ($TiO_{0.700}$) and $Ti_{0.877}O_{0.833}$ ($TiO_{0.950}$) monoxides with the orthorhombic (space group *Immm*) ordering of the $Ti_3O_2\square$ type, and X-ray patterns of the $Ti_{0.833}O_{0.898}$ ($TiO_{1.077}$), $Ti_{0.793}O_{0.952}$ ($TiO_{1.200}$), and $Ti_{0.768}O_{0.983}$ ($TiO_{1.280}$) monoxides with the orthorhombic (space group *Immm*) ordering of the $Ti_2\blacksquare O_3$ type. For the $Ti_{0.968}O_{0.678}$ and $Ti_{0.877}O_{0.833}$ monoxides, the long-range order parameter $\eta_4^{(\bigcirc)}$ is equal, respectively, to 0.966 and 0.50, and the period a_{B1} of the disordered basal cubic lattice is, respectively, 0.4207 and 0.4184 nm. The long-range order parameter $\eta_4^{(\mathrm{Ti})}$ for the $Ti_{0.833}O_{0.898}$, $Ti_{0.793}O_{0.952}$, and $Ti_{0.768}O_{0.983}$ monoxides is equal, respectively, to 0.50, 0.62, and 0.696, and the period a_{B1} of the basal lattice is, respectively, 0.41755, 0.41698, and 0.41675 nm. The translation periods of the rhombic unit cell are $a = a_{B1}/\sqrt{2}$, $b = 3a_{B1}/\sqrt{2}$, and $c = a_{B1}$. X-ray pattern of an ideal ordered monoclinic (space group $C2/m$) $Ti_5\blacksquare O_5\square$ phase ($a_{B1} = 0.41804$ nm) is shown for comparison. Cu$K\alpha_{1,2}$ radiation, $u = v = 0.1$, $w = 0.02$, and $U_{iso} = 0.01$.

If the ordering occurs in the metallic sublattice of the Ti_xO_z monoxide with $1 > x > (2t-1)/2t$ and $y \equiv z/x > 1$, then the maximal value of long-range order parameter is

$$\eta_4^{(\mathrm{Ti})\max}(x) = 2t(1-x) \equiv 3(1-x), \quad t = 1.5. \quad (4)$$

At the upper boundary of the homogeneity region of TiO_y ($y \approx 1.28$ and $x \approx 0.77$), the maximal value of parameter $\eta_4^{(\mathrm{Ti})}$ in the ordered phase does not exceed 0.70. On changing composition from $TiO_{1.28}$ to that of the equiatomic monoxide TiO ($Ti_{0.833}O_{0.833}$), the maximal value of the long-range order parameter decreases to 0.50.

The unit cell of a partially ordered orthorhombic (space group *Immm*) phase $Ti_2\blacksquare O_3$ of TiO_y with $y > 1$ is

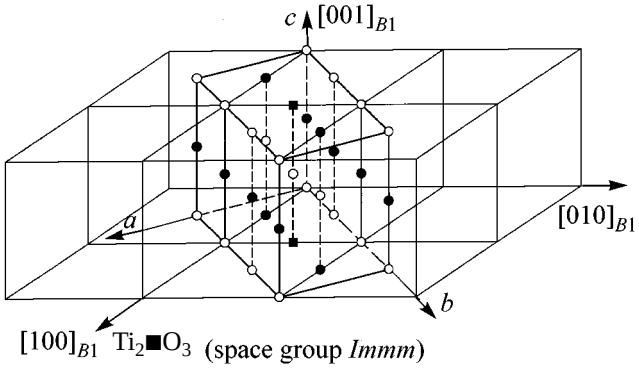

Fig. 3. Unit cell of the orthorhombic (space group *Immm*) $Ti_2{\blacksquare}O_3$ superstructure in the basal lattice of the $TiO_y \equiv Ti_xO_z$ ($y \equiv z/x > 1$) monoxide with structure *B*1: ○ are the oxygen sites randomly (with probability *z*) occupied by the O atoms; ● are the metallic 4(*h*) positions occupied by the Ti atoms; ■ are the metallic 2(*c*) positions vacant with probability $(1 - n_{1(Ti)})$. In the $Ti_2{\blacksquare}O_3$ superstructure of the TiO_y ($y > 1$) monoxide, the vacant sites of the metallic sublattice are located in every third $(110)_{B1}$ plane of the basal cubic lattice; the sites of these planes are randomly occupied by the vacancies.

depicted in Fig. 3. This cell is the inverse of the unit cell of rhombic superstructure $Ti_3O_2{\square}$ (Fig. 1) and can be obtained through replacing the sites of the metallic sublattice by the sites of the nonmetallic sublattice.

At all sites of the metallic sublattice, the distribution function in Eq. (3) takes either of two values: $n_{1(Ti)} = x - 2\eta_4^{(Ti)}/3$ at positions 2(*c*) and $n_{2(Ti)} = x + \eta_4^{(Ti)}/3$ at positions 4(*h*). One can readily verify that, for the maximal degree of long-range order and $1 > x > (2t - 1)/2t$, the $n_{2(Ti)}$ value is always equal to unity, while $x \geq n_{1(Ti)} \geq 3x - 2$ and is always smaller than unity. This implies that the Ti atoms in the ordered orthorhombic phase of the TiO_y ($y > 1$) monoxide occupy all 4(*h*) positions, whereas the 2(*c*) positions are vacant with probability $P = 1 - n_{1(Ti)}$ [or occupied by the titanium atoms with probability $n_{1(Ti)}$]. In the $Ti_2{\blacksquare}O_3$ superstructure under discussion ($y > 1$), the metallic vacancies are located in every third 110_{B1} plane of the basal cubic structure (Fig. 3) and randomly distributed over the sites of these planes.

Figure 2 shows the calculated X-ray patterns of the $Ti_{0.833}O_{0.898}$ ($TiO_{1.077}$), $Ti_{0.793}O_{0.952}$ ($TiO_{1.20}$), and $Ti_{0.768}O_{0.983}$ ($TiO_{1.28}$) monoxides with the orthorhombic (space group *Immm*) ordering of the $Ti_2{\blacksquare}O_3$ type; the long-range order parameter $\eta_4^{(Ti)}$ is 0.50, 0.62, and 0.696, respectively. The superstructural reflections in the X-ray pattern of the ordered $Ti_{0.833}O_{0.898}$ monoxide, whose composition can be written as $Ti_5{\blacksquare}(O_{0.898}{\square}_{0.102})_6$, are only those of the rhombic phase; the reflections corresponding to the monoclinic or trigonal superstructures of the $M_5{\blacksquare}X_6$ type are absent. With the indicated vacancy concentrations in the titanium and oxygen sublattices, the ordered $TiO_{1.20}$ monoxide cannot even formally be represented as Ti_5O_6 or, taking into account the presence of two formula units in the rhombic unit cell, as $Ti_{2.5}O_3$, as was suggested in [12].

The X-ray pattern of an ideal ordered monoclinic (space group $C2/m$)$Ti_5{\blacksquare}O_5{\square}$ compound is given in Fig. 2 for comparison. One can clearly see that all superstructure reflections of the orthorhombic $Ti_3O_2{\square}$and $Ti_2{\blacksquare}O_3$ phases coincide with a part of superstructure reflections of the monoclinic $Ti_5{\blacksquare}O_5{\square}$ phase (a small noncoincidence is caused by the fact that the base lattice periods a_{B1} are different for the compositionally different monoxides). The reason for the coincidence is quite clear. Apart from the rays of the $\{\mathbf{k}_{10}\}$ and $\{\mathbf{k}_1\}$ stars, the $TiO_y \rightleftharpoons Ti_5{\blacksquare}O_5{\square}$ transition channel involves the rays of the $\{\mathbf{k}_4\}$ star with parameter $\mu_4 = 1/3$. The rays of the $\{\mathbf{k}_4\}$ star, which form the TiO_y ($y < 1$) $\rightleftharpoons Ti_3O_2{\square}$ and TiO_y ($y > 1$) $\rightleftharpoons Ti_2{\blacksquare}O_3$ transition channels, have the same value of parameter $\mu_4 = 1/3$ and, hence, the same length. Because of this, the reflections corresponding to the wave vectors of the $\{\mathbf{k}_4\}$ star coincide in a diffraction experiment with a polycrystal. When studying the ordering in polycrystalline samples, these reflections can be distinguished only in the presence of displacement. In the diffraction experiment with a single crystal, the rhombic and monoclinic reflections caused by the $\{\mathbf{k}_4\}$ star must be observed at different positions. Indeed, in the electron diffraction experiment with titanium monoxide, the authors of [10] observed reflections corresponding to both monoclinic and orthorhombic phases simultaneously.

The formation of orthorhombic phases in titanium monoxide is caused by the symmetry distortions along the non-Lifshitz star $\{\mathbf{k}_4\}$, for which the vector $3\mathbf{k}_4^{(1)}$ coincides with the structural vector $(220)_{B1}$. Hence, it follows that the Landau criterion for the second-order phase transitions does not hold in our case, so that the order–disorder transformations TiO_y ($y < 1$) $\rightleftharpoons$ $Ti_3O_2{\square}$ and TiO_y ($y > 1$) $\rightleftharpoons$ $Ti_2{\blacksquare}O_3$ are first-order transitions.

REFERENCES

1. J. L. Murray and H. A. Wriedt, Bull. Alloy Phase Diagrams **8**, 148 (1987).
2. R. C. De Vries and R. Roy, Am. Ceram. Soc. Bull. **33**, 370 (1954).
3. P. G. Wahlbeck and P. W. Gilles, J. Am. Ceram. Soc. **49**, 180 (1966).
4. A. I. Gusev and A. A. Rempel', *Nonstoichiometry, Disorder and Order in Solid* (Ural. Otd. Ross. Akad. Nauk, Yekaterinburg, 2001).
5. S. Andersson, B. Collen, U. Kuylenstierna, and A. Magneli, Acta Chem. Scand. **11**, 1641 (1957).

6. M. D. Banus, T. B. Reed, and A. J. Strauss, Phys. Rev. B **5**, 2775 (1972).
7. A. A. Valeeva, A. A. Rempel', and A. I. Gusev, Neorg. Mater. **37**, 716 (2001).
8. D. Watanabe, J. R. Castles, A. Jostsons, and A. S. Malin, Nature **210**, 934 (1966); Acta Crystallogr. **23**, 307 (1967).
9. E. Hilti and F. Laves, Naturwissenschaften **55**, 131 (1968).
10. D. Watanabe, O. Terasaki, A. Jostsons, and J. R. Castles, in *The Chemistry of Extended Defects in Non-Metallic Solids*, Ed. by L. Eyring and M. O. Keeffe (North-Holland, Amsterdam, 1970), pp. 238–258.
11. A. A. Valeeva, A. A. Rempel', and A. I. Gusev, Pis'ma Zh. Éksp. Teor. Fiz. **71**, 675 (2000) [JETP Lett. **71**, 460 (2000)].
12. E. Hilti, Naturwissenschaften **55**, 130 (1968).
13. A. I. Gusev and A. A. Rempel, Phys. Status Solidi A **135**, 15 (1993).
14. A. I. Gusev, *Physical Chemistry of Nonstoichiometric Refractory Compounds* (Nauka, Moscow, 1991).
15. A. I. Gusev, Usp. Fiz. Nauk **170**, 3 (2000).
16. O. V. Kovalev, *Irreducible Representations of the Space Groups* (Naukova Dumka, Kiev, 1961; Gordon and Breach, New York, 1965).
17. S. Andersson, Acta Chem. Scand. **13**, 415 (1959).

Translated by V. Sakun

JETP Letters, Vol. 74, No. 2, 2001, pp. 96–99. From Pis'ma v Zhurnal Éksperimental'noĭ i Teoreticheskoĭ Fiziki, Vol. 74, No. 2, 2001, pp. 101–104.

Critical Temperature of Superconductor/Ferromagnet Bilayers[1]

Ya. V. Fominov[1,2]*, N. M. Chtchelkatchev[1], and A. A. Golubov[2]

[1] *Landau Institute for Theoretical Physics, Russian Academy of Sciences, Moscow, 117940 Russia*

** e-mail: fominov@landau.ac.ru*

[2] *Department of Applied Physics, University of Twente, P.O. Box 217, 7500 AE Enschede, The Netherlands*

Received June 14, 2001

Superconductor/ferromagnet bilayers are known to exhibit nontrivial dependence of the critical temperature T_c on the thickness d_f of the ferromagnetic layer. We develop a general method for investigation of T_c as a function of the bilayer parameters. It is shown that interference of quasiparticles makes $T_c(d_f)$ a nonmonotonic function. The results are in good agreement with experiment. Our method also applies to multilayered structures. © *2001 MAIK "Nauka/Interperiodica".*

PACS numbers: 74.50.+r; 74.80.Dm; 75.30.Et

Recently, much attention has been paid to properties of hybrid proximity systems containing superconductors (S) and ferromagnets (F); new physical phenomena were predicted and observed in these systems [1–4]. One of the most striking effects in SF layered structures is the highly nonmonotonic dependence of the critical temperature T_c of the system on the thickness d_f of the ferromagnetic layers. Experiments exploring this nonmonotonic behavior have been performed previously on SF multilayers such as Nb/Gd [5], Nb/Fe [6], V/V–Fe [7], and Pb/Fe [8], but the results (and, in particular, comparison between the experiments and theories) were not conclusive.

To perform reliable experimental measurements of $T_c(d_f)$, it is essential to have d_f large compared to the interatomic distance; this situation can be achieved only in the limit of weak ferromagnets. Active experimental investigations of SF bilayers and multilayers based on Cu–Ni dilute ferromagnetic alloys are being carried out by the group of Ryazanov[2] [9]. In SF bilayers, they observed a highly nonmonotonic dependence $T_c(d_f)$. While the reason for this effect in multilayers can be the 0–π transition [3], in a bilayer system with a single superconductor this mechanism is irrelevant and the cause of the effect is quasiparticle interference specific to SF structures.

In this paper motivated by the ROP experiment [9], we theoretically study the critical temperature of SF bilayers. Previous theoretical investigations of T_c in SF structures were concentrated on systems with thin or thick S(F) layers [compared to the coherence length of the superconductor (ferromagnet)], with SF boundaries having very low or very high transparency; besides, the exchange energy was often assumed to be much larger then the critical temperature [3, 7, 8, 10–13]. The parameters of the ROP experiment do not correspond to any of these limiting cases. In this paper, we develop an approach giving an opportunity to investigate not only the limiting cases of parameters, but also the intermediate region. Using our method, we find different types of nonmonotonic behavior of T_c as a function of d_f such as the minimum of T_c and even reentrant superconductivity [14]. Comparison of our theoretical predictions with the experimental data shows good agreement.

We assume that dirty-limit conditions are fulfilled and calculate the critical temperature of the bilayer within the framework of the linearized Usadel equations for the S and F layers (the domain $0 < x < d_s$ is occupied by the S metal; $-d_f < x < 0$, by the F metal—see Fig. 1). Near T_c, the normal Green's function is $G = \operatorname{sgn}\omega_n$, and the Usadel equations for the anomalous function F take the form

$$\xi_s^2 \pi T_{cs} \frac{d^2 F_s}{dx^2} - |\omega_n| F_s + \Delta = 0, \quad 0 < x < d_s; \tag{1}$$

$$\xi_f^2 \pi T_{cs} \frac{d^2 F_f}{dx^2} - (|\omega_n| + iE_{ex}\operatorname{sgn}\omega_n) F_f = 0, \quad -d_f < x < 0; \tag{2}$$

$$\Delta \ln\frac{T_{cs}}{T} = \pi T \sum_{\omega_n} \left(\frac{\Delta}{|\omega_n|} - F_s \right), \tag{3}$$

where $\xi_s = \sqrt{D_s/2\pi T_{cs}}$, $\xi_f = \sqrt{D_f/2\pi T_{cs}}$, $\omega_n = \pi T(2n+1)$ with $n = 0, \pm1, \pm2, \ldots$ are the Matsubara frequencies, E_{ex} is the exchange energy, and T_{cs} is the critical temperature of the S layer. $F_{s(f)}$ denotes the function F in the S(F) region.

[1] This article was submitted by the authors in English.

[2] Ryazanov, Oboznov, Prokof'ev, *et al.*—hereafter referenced as ROP.

Equations (1)–(3) must be supplemented with the boundary conditions at the outer surfaces of the bilayer,

$$\frac{dF_s(d_s)}{dx} = \frac{dF_f(-d_f)}{dx} = 0, \tag{4}$$

as well as at the SF boundary,

$$\xi_s \frac{dF_s(0)}{dx} = \gamma \xi_f \frac{dF_f(0)}{dx}, \quad \gamma = \frac{\rho_s \xi_s}{\rho_f \xi_f}, \tag{5}$$

$$\xi_f \gamma_b \frac{dF_f(0)}{dx} = F_s(0) - F_f(0), \quad \gamma_b = \frac{R_b \mathcal{A}}{\rho_f \xi_f}. \tag{6}$$

Here, $\rho_{s,f}$ are the normal-state resistivities of the S and F metals, R_b is the total resistance of the SF boundary, and $\mathcal{A}$ is its area. The Usadel equation in the F layer is readily solved:

$$F_f = C(\omega_n)\cosh(k_f(x + d_f)), \tag{7}$$

with

$$k_f = \frac{1}{\xi_f}\sqrt{\frac{|\omega_n| + iE_{ex}\operatorname{sgn}\omega_n}{\pi T_{cs}}}, \tag{8}$$

and the boundary condition at $x = 0$ can be written in closed form with respect to F_s:

$$\xi_s \frac{dF_s(0)}{dx} = \frac{\gamma}{\gamma_b + B_f(\omega_n)} F_s(0), \tag{9}$$

where $B_f(\omega_n) = [k_f \xi_f \tanh(k_f d_f)]^{-1}$.

This boundary condition is complex. In order to rewrite it in real form, we do the usual trick and go over to the functions $F^{\pm} = F(\omega_n) \pm F(-\omega_n)$. The symmetric properties of F^+ and F^- are trivial, so we will treat only positive ω_n. The self-consistency equation is expressed only via the symmetric function F_s^+,

$$\Delta \ln\frac{T_{cs}}{T} = \pi T \sum_{\omega_n > 0}\left(\frac{2\Delta}{\omega_n} - F_s^+\right), \tag{10}$$

and the problem of determining T_c can be formulated in closed form with respect to F_s^+. This is done as follows. The Usadel equation for F_s^- does not contain Δ; hence, it can be solved analytically. After that, we exclude F_s^- from boundary condition (9) and arrive at the effective boundary conditions for F_s^+:

$$\xi_s \frac{dF_s^+(0)}{dx} = W(\omega_n)F_s^+(0), \quad \frac{dF_s^+(d_s)}{dx} = 0, \tag{11}$$

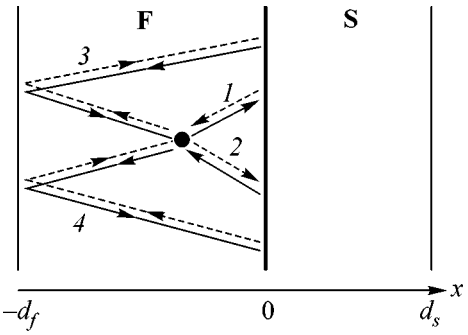

Fig. 1. The SF bilayer. The F and S layers occupy the regions $-d_f < x < 0$ and $0 < x < d_s$, respectively. The four types of trajectories contributing (in Feynman path integral sense) to the anomalous wave function of correlated quasiparticles are shown in the ferromagnetic region. The solid lines correspond to electrons, and the dashed lines to holes; the arrows indicate the direction of the velocity.

where

$$W = \gamma \frac{A_s(\gamma_b + \operatorname{Re}B_f) + \gamma}{A_s|\gamma_b + B_f|^2 + \gamma(\gamma_b + \operatorname{Re}B_f)}, \tag{12}$$
$$A_s = k_s\xi_s\tanh(k_s d_s), \quad k_s = 1/\xi_s(\sqrt{\omega_n/\pi T_{cs}}).$$

Self-consistency equation (10) and boundary conditions (11), (12) together with the Usadel equation for F_s^+,

$$\xi_s^2 \pi T_{cs}\frac{d^2F_s^+}{dx^2} - \omega_n F_s^+ + 2\Delta = 0, \tag{13}$$

will be used below to find the critical temperature of the bilayer.

The Green's function (in a mathematical sense) of problem (11)–(13) can be expressed via solutions v_1, v_2 of Eq. (13) without Δ, satisfying the boundary conditions at $x = 0$ and $x = d_s$, respectively:

$$G(x, y; \omega_n) = \frac{k_s\xi_s/\omega_n}{\sinh(k_s d_s) + a\cosh(k_s d_s)} \times \begin{cases} v_1(x)v_2(y), & x \le y \\ v_2(x)v_1(y), & y \le x, \end{cases} \tag{14}$$

where $a = W(\omega_n)/k_s\xi_s$ and

$$v_1(x) = \cosh(k_s x) + a\sinh(k_s x), \quad v_2(x) = \cosh(k_s(x - d_s)). \tag{15}$$

Having found $G(x, y; \omega_n)$, we can write the solution of Eqs. (11)–(13) as

$$F_s^+(x; \omega_n) = 2\int_0^{d_s} G(x, y; \omega_n)\Delta(y)dy. \tag{16}$$

Substituting this into self-consistency equation (10), we obtain

$$\Delta(x)\ln\frac{T_{cs}}{T_c} = 2\pi T_c \sum_{\omega_n>0}\left[\frac{\Delta(x)}{\omega_n} - \int_0^{d_s} G(x, y; \omega_n)\Delta(y)dy\right]. \quad (17)$$

This equation can be expressed in symbolic form: $\Delta\ln(T_{cs}/T_c) = \hat{L}\Delta$. Then, T_c is determined from the condition

$$\det\left(\hat{L} - \hat{1}\ln\frac{T_{cs}}{T_c}\right) = 0 \quad (18)$$

that Eq. (17) have a nontrivial solution with respect to Δ. Numerically, we put our problem (17), (18) on a spatial grid so that the linear operator $\hat{L}$ becomes a finite matrix.

Equations (14)–(18) are our central result; substituting the concrete parameters of the system, we can easily find the critical temperature numerically and in certain cases analytically. (The models considered previously [3, 7, 8, 10–13] correspond to the limiting cases of our theory.)

We apply our method to fit ROP experimental data [9]; the result is presented in Fig. 2. Estimating the parameters d_s = 11 nm, T_{cs} = 7 K, ρ_s = 7.5 μΩ cm, ξ_s = 8.9 nm, ρ_f = 60 μΩ cm, ξ_f = 7.6 nm, and γ = 0.15 from the experiment and fitting only E_{ex} and γ_b, we find good agreement between our theoretical predictions and the experimental data. The fitting procedure was the following: first, we determine $E_{ex} \approx 130$ K from the position of the minimum of $T_c(d_f)$; second, we find $\gamma_b \approx 0.3$ from fitting the vertical position of the curve. The deviation of our curve from the experimental points is small; it is most pronounced in the region of small d_f corresponding to the initial decrease of T_c. This is not unexpected because when d_f is of the order of a few nanometers, the thickness of the F film may vary significantly along the film (which is not taken into account in our theory) and the thinnest films can even be formed by an array of islands rather than by continuous material. At the same time, we note that the minimum of T_c occurs at $d_f \approx 5$ nm, when with good accuracy the F layer has uniform thickness.

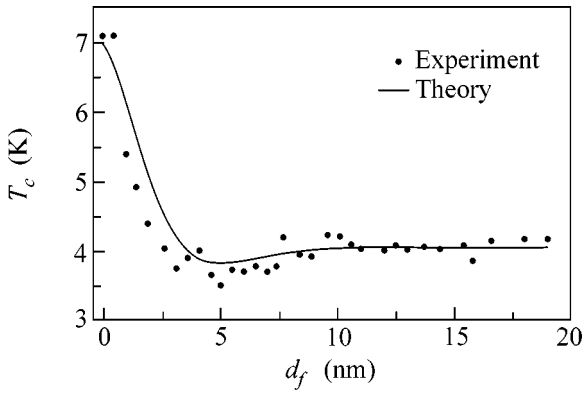

Fig. 2. Theoretical fit to ROP experimental data [9]. In the experiment, Nb was the superconductor (with d_s = 11 nm, T_{cs} = 7 K) and $Cu_{0.43}Ni_{0.57}$ was the weak ferromagnet. From our fit, we estimate $E_{ex} \approx 130$ K and $\gamma_b \approx 0.3$.

The position of the minimum of $T_c(d_f)$ can be estimated from qualitative arguments based on interference of quasiparticles in the ferromagnet. Let us consider a point x inside the F layer. According to Feynman's interpretation of quantum mechanics [15], the quasiparticle wave function [we are interested in an anomalous wave function of correlated quasiparticles, which characterizes the superconductivity; this function is equivalent to the anomalous Green's function $F(x)$] may be represented as a sum of the wave amplitudes over all classical trajectories; the wave amplitude for a given trajectory equals $\exp(iS)$, where S is the classical action along this trajectory. To obtain our anomalous wave function, we must sum over trajectories that (i) start and end at the point x and (ii) change the type of the quasiparticle (i.e., convert an electron into a hole or vice versa). There are four kinds of trajectories which should be taken into account (see Fig. 1). Two of them (denoted 1 and 2) start in the direction toward the SF interface (as an electron and as a hole), experience Andreev reflection, and return to the point x. The other two trajectories (denoted 3 and 4) start in the direction away from the interface, experience normal reflection at the outer surface of the F layer, move toward the SF interface, experience Andreev reflection there, and finally return to the point x. The main contribution is given by the trajectories normal to the interface. The corresponding actions are $S_1 = -S_2 = -Qx$ and $S_3 = -S_4 = -Q(2d_f + x)$ (note that $x < 0$), where Q is the difference between the wave numbers of the electron and the hole. To make our arguments clearer, we assume that the ferromagnet is strong and the SF interface is ideal, and consider the clean limit first: in this case $Q = k_e - k_h = \sqrt{2m(E + E_{ex} + \mu)} - \sqrt{2m(-E - E_{ex} + \mu)} \approx 2E_{ex}/v$, where E is the quasiparticle energy, μ is the Fermi energy, and v is the Fermi velocity. Thus, the anomalous wave function of the quasiparticles is $F(x) \propto \sum_{n=1}^{4}\exp(iS_n) \propto \cos(Qd_f)\cos(Q(d_f + x))$. The suppression of T_c by the ferromagnet is determined by the value of the wave function at the SF interface: $F(0) \propto \cos^2(Qd_f)$. The minimum of T_c corresponds to the minimal value of $F(0)$, which is achieved at $d_f = \pi/2Q$. In the

dirty limit the above expression for Q is replaced by $Q = \sqrt{E_{ex}/D_f}$; hence, the minimum of $T_c(d_f)$ occurs at

$$d_f^{(\min)} = \frac{\pi}{2}\sqrt{\frac{D_f}{E_{ex}}}. \quad (19)$$

In the case of ROP bilayer [9], we obtain $d_f^{(\min)} \approx 7$ nm, whereas the experimental value is 5 nm (Fig. 2); thus, our qualitative estimate appears to be reasonable.

The method developed in this paper applies directly to multilayered SF structures (in particular, to trilayers) in the 0-state, where an SF bilayer can be considered as an elementary cell of the system. A generalization can be made, which allows one to take into account possible superconductive and/or magnetic π-states.

In conclusion, we have developed a method for calculating the critical temperature of a SF bilayer as a function of parameters of the junction. The approach developed here gives an opportunity to evaluate T_c in a wide range of parameters. We demonstrate that there is good agreement between the experimental data and our theoretical predictions. Qualitative arguments are given that explain the nonmonotonic behavior of the function $T_c(d_f)$. Extensive details of our study will be published elsewhere [14].

We thank V.V. Ryazanov and M.V. Feigel'man for stimulating discussions and useful comments on the manuscript. We are especially indebted to V.V. Ryazanov for communicating the experimental result of his group to us prior to the detailed publication. Also, we are grateful to M.Yu. Kupriyanov and Yu. Oreg for enlightening comments. Ya.V.F. acknowledges financial support from the Russian Foundation for Basic Research (RFBR) (project no. 01-02-17759) and from Forschungszentrum Jülich (Landau Scholarship). The research of N.M.C. was supported by the RFBR (project no. 01-02-06230), by Forschungszentrum Jülich (Landau Scholarship), by the Netherlands Organization for Scientific Research (NWO), and by the Swiss National Foundation.

REFERENCES

1. V. V. Ryazanov, V. A. Oboznov, A. Yu. Rusanov, *et al.*, Phys. Rev. Lett. **86**, 2427 (2001); V. V. Ryazanov, V. A. Oboznov, A. V. Veretennikov, *et al.*, cond-mat/0103240.
2. T. Kontos, M. Aprili, J. Lesueur, *et al.*, Phys. Rev. Lett. **86**, 304 (2001).
3. Z. Radović, M. Ledvij, Lj. Dobrosavljević-Grujić, *et al.*, Phys. Rev. B **44**, 759 (1991).
4. L. R. Tagirov, Phys. Rev. Lett. **83**, 2058 (1999).
5. J. S. Jiang, D. Davidović, D. H. Reich, *et al.*, Phys. Rev. Lett. **74**, 314 (1995).
6. Th. Mühge, N. N. Garif'yanov, Yu. V. Goryunov, *et al.*, Phys. Rev. Lett. **77**, 1857 (1996).
7. J. Aarts, J. M. E. Geers, E. Brück, *et al.*, Phys. Rev. B **56**, 2779 (1997).
8. L. Lazar, K. Westerholt, H. Zabel, *et al.*, Phys. Rev. B **61**, 3711 (2000).
9. V. V. Ryazanov, V. A. Oboznov, A. S. Prokof'ev, *et al.*, to be published.
10. A. I. Buzdin, B. Bujičić, and M. Yu. Kupriyanov, Zh. Éksp. Teor. Fiz. **101**, 231 (1992) [Sov. Phys. JETP **74**, 124 (1992)].
11. E. A. Demler, G. B. Arnold, and M. R. Beasley, Phys. Rev. B **55**, 15174 (1997).
12. Yu. N. Proshin and M. G. Khusainov, Zh. Éksp. Teor. Fiz. **113**, 1708 (1998) [JETP **86**, 930 (1998)]; Zh. Éksp. Teor. Fiz. **116**, 1887 (1999) [JETP **89**, 1021 (1999)].
13. L. R. Tagirov, Physica C (Amsterdam) **307**, 145 (1998).
14. Ya. V. Fominov, N. M. Chtchelkatchev, and A. A. Golubov, in preparation.
15. R. P. Feynman and A. R. Hibbs, *Quantum Mechanics and Path Integrals* (McGraw-Hill, New York, 1965; Mir, Moscow, 1968).